

ADA955386



CHAPTER 2 - PART 2
PAGES 2-151 through
2-303

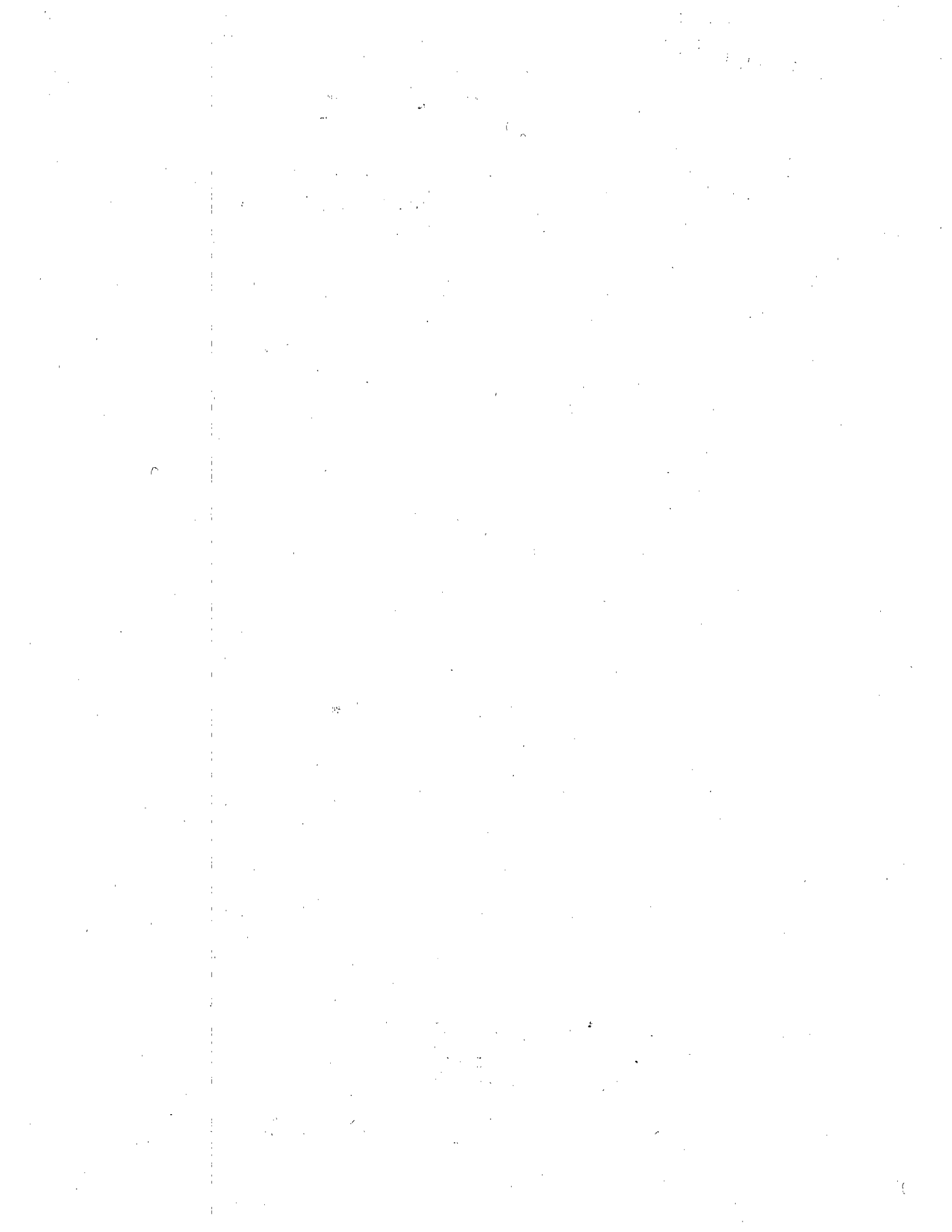
Chapter 2

BLAST AND SHOCK PHENOMENA

AD-A955 386

DTIC
ELECTE
S 2 MAR 1989 D
E

REPRODUCED BY
U.S. DEPARTMENT OF COMMERCE
NATIONAL TECHNICAL
INFORMATION SERVICE
SPRINGFIELD, VA 22161



[REDACTED]

On the other hand, the radiative coupling may be increased by as much as a factor of 5 compared to surface bursts if there is a slight penetration of the weapon into the surface of the ground (3 to 5 meters for a 1 Mt burst). This greater coupling is in addition to the well known increase in mechanical coupling, which is discussed in paragraph 2-47.

2-47 Mechanical Coupling

The preceding discussion outlined the flow of energy into the ground for cratering events that result from bursts at or above the surface. These processes take place during the first several milliseconds of actual crater formation. The hydrodynamic portion of crater formation may last for several seconds.

If the explosion occurs at a height-of-burst greater than 4 to 5 $m/kt^{1/3}$, the crater will be formed almost exclusively by compaction. Scouring, which results from airblast and airblast associated winds, contributes a small fraction of the crater volume. Since there is little fallback in such a crater, the true and apparent craters are essentially identical. As the height of burst is decreased, an increasing fraction of the crater is formed by excavation and ejection of ground material. In addition, compaction, plastic deformation and flow of the material in the rupture zone are principal mechanisms for crater formation of very near-surface bursts. These mechanisms produce a slight increase in material density as well as considerable brittle and plastic failure of the ground material. The mechanisms also cause a radial displacement with an overturning of crater material around the edge of the crater. The top of this mound is termed the crater lip. After detonation, the crater may be partially refilled by material falling back into the crater (fallback), by slumping, and by late-time rebound. The material thrown out beyond the crater lip (ejecta) forms a layer whose thickness diminishes with radial distance from the burst point.

The first diagram in Figure 2-70b illustrates the general crater shape that is expected from an above-surface burst. Despite many explosive cratering experiments with nuclear and high-explosive (HE) devices, the complex interrelationships that exist among the various mechanisms that could cause craters preclude the quantitative dynamics of crater formation by near-surface bursts from being well understood.

The size and shape of craters from subsurface detonations are affected significantly by the depth of burial. The dominant cratering mechanisms, which are discussed in succeeding paragraphs, will be related to the depths of burial shown in Figure 2-70b.

- *Crushing, Compaction, Plastic Deformation.* As the high pressure explosion gases expand against the surrounding medium, a spherical shock wave is generated. The initial shock pressures are as large as 10 to 100 million atmospheres. The medium surrounding a nuclear explosion is initially melted and vaporized as the shock passes through it. As the shock front moves outward in a spherically diverging shell, the medium behind the shock front is put into radial compression and tangential tension. The peak pressure in the shock front attenuates by spherical divergence and dissipative mechanisms in the medium. The material around the explosive charge (nuclear or HE) is crushed, heated, and physically displaced outward, forming a cavity. In regions outside this cavity, the shock wave will produce permanent deformation by plastic flow. This mechanism of crater formation is a significant contributor to crater size for bursts at or just below the ground surface (Figure 2-70b,(b)); and at depths of burial that result in subsidence craters (Figure 2-70b,(f)).

- [REDACTED]
- *Spalling.* When an upward moving shock (compressive) front encounters the air-ground interface, the large mismatch of material properties results in the generation of a negative stress (rarefaction) wave. The rarefaction wave propagates back into the medium in which the burst occurred, and puts the medium (originally under high compression) into tension (or less compression). This phenomenon causes the medium to break up and move upward with a velocity characteristic of the total momentum imparted to it. In a loose soil material, this spalling ejects individual particles of similar size into the air. In a rock medium, however, the thickness and size of the spalled material generally is determined by the presence of pre-existing fracture patterns and zones of weakness. The velocity of the spalled material decreases in proportion to the decrease in peak compressive stress. The spall mechanism produces an extended rupture and plastic zone near the ground surface and contributes significantly to the true lip height of the crater. This mechanism appears to be dominant in determining crater size at shallow depths of burial (Figure 2-70b,(c)).
 - *Gas Acceleration.* Gases are produced in the material surrounding the explosion by vaporization and chemical changes induced by heat and pressure. The near-adiabatic expansion of the gases imparts motion to the medium. At depths of burial at which crater dimensions are maximized (optimum DOB), the cavity gases produce appreciable acceleration in overlying material before they escape (vent) through cracks extending from the cavity to the surface. Gas acceleration is the dominant crater producing mechanism at optimum DOB (Figure 2-70b,(d)). At

shallow depths of burial the gases cannot exert significant pressure before venting occurs. In the case of very deep explosions, the weight of the overburden precludes any significant gas induced acceleration of the overlying material.

- *Overburden Collapse.* At depths of burial that are large (two or more times) compared to the optimum, the mechanism of overburden collapse (subsidence) becomes dominant. This effect is closely linked to the crushing, compaction and plastic deformation mechanism that produces an underground cavity. At these large depths of burial, spall and gas acceleration will not impart sufficient velocity to the overlying material to eject it physically from the crater. It would be expected that the crater volume would be determined largely by the underground cavity formed by the detonation. In a rock medium, however, material that is fractured and displaced from its original position tends to take up more space than it occupied in its natural state. This bulking action could result in no crater or, indeed, even a mound above the ground. A mound was produced after the SULKY detonation, as shown in Figure 2-72a.

In certain geologic materials yet another type of subsidence occurs. When the pressure in the cavity decreases below overburden pressure, the roof of the cavity begins to collapse. In most media, this collapse will continue upward and will form a "chimney" of collapsed material. In a soil medium, where the density of the material will not change significantly after it has fallen, the volume of the cavity will be transmitted to the surface, forming a "subsidence crater" on the surface (Figure 2-70b,(f)). This phenomenon is illustrated in Figure 2-72b.



Figure 2-72a. SULKY, Event; Mound Created by the Bulking of Rock Material in a Deeply Buried
0.087 kt Nuclear Detonation:
Mound Diameter = 48.8 m (160 ft.); Mound Height = 7.6 m (25 ft.); DOB = 27 m (90 ft.)

Reproduced from
best available copy.



Reproduced from
best available copy.



Figure 2-72b. PASSAIC Event; Subsidence Crater Produced by a Deeply Buried Nuclear Detonation in a Soil Medium

PREDICTION OF CRATER DIMENSIONS

The present prediction of crater dimensions for above-surface, surface, and shallow-buried bursts is based on the nuclear tests conducted in dry alluvial soil at the Nevada Test Site and the saturated coral at the Pacific Proving Ground. Extrapolation to other geologies is made on the basis of HE spherical-charge events. There have been no high-yield near-surface nuclear experiments in dry soil or rock. It is assumed that the influence of geology can be separated from that of the energy source. However, the nuclear tests conducted at the Pacific Proving Ground (saturated coral) and HE tests conducted at the Suffield Experiment Station (wet soil) suggest that the influence of geology is not *entirely* independent of the source. This fact is illustrated in Figure 2-73.

The dimensions of the crater vary in a complex manner as the HOB approaches the ground surface; but with lower HOBs the apparent depth of the crater generally increases and the ratio of the apparent radius to depth decreases. When crater dimensions for surface, above-surface, and shallow-buried bursts are scaled to yields much greater than 1 kt (for example, 1 Mt), the calculated change in the shape of the apparent crater as the yield increases is also an important consideration. This phenomenon, unfortunately, has not been observed in dry media.

2-48 Crater Dimension Scaling

The results of cratering explosions of various yields and burst geometries have been correlated by empirical scaling laws that express crater dimensions in terms of a standard yield of one kiloton. Crater dimensions for any other yield can be predicted by application of an empirical yield scaling exponent, as will be described in the succeeding paragraphs. The dimen-

sions for which curves and scaling procedures will be presented are the radius of the apparent crater, R_a , the depth of the apparent crater, D_a , and the apparent volume V_a . Other pertinent crater dimensions such as the radius to the crest of the apparent lip and the height of the apparent lip, may be related to the above dimensions by scaling laws that will be described.

Several burst geometries will be considered: above-surface (near and contact), surface, shallow-buried, and deep-buried bursts. The actual height of burst (HOB) or depth of burst (DOB) is measured from the original ground surface to the *center of energy* of the weapon. The scaled HOB or DOB is the actual dimension divided by the scaled yield (described below). Of the *above-surface* bursts ($HOB/W^{1/3} > 0$), the lower bursts are of most significance to cratering, i.e., $HOB/W^{1/3} \leq 3 \text{ m/kt}^{1/3}$. A *contact* burst is considered to be one wherein the weapon is in contact with the ground surface, and therefore has an actual HOB of approximately 0.5 m. A *surface* burst is one in which the HOB as defined above, is exactly zero. A *shallow-buried* burst has a $DOB/W^{1/3} \leq 5 \text{ m/kt}^{1/3}$ and the *deep-buried* burst has a $DOB/W^{1/3} > 5 \text{ m/kt}^{1/3}$.

No single yield scaling exponent has been found to be valid for scaling apparent crater dimensions over a wide range of yield, geology, and HOB or DOB. However, the following yield scaling exponents, a , (yield, W (kt), to the a power) have been found to be approximately correct for scaling the apparent crater dimensions for surface/above-surface bursts and for deep-buried bursts:

$$a = 1/3 \text{ for } 0 < \frac{HOB}{W^{1/3}} \leq 3 \text{ m/kt}^{1/3},$$

$$a = 1/3.4 \text{ for } \frac{DOB}{W^{1/3}} > 5 \text{ m/kt}^{1/3}.$$

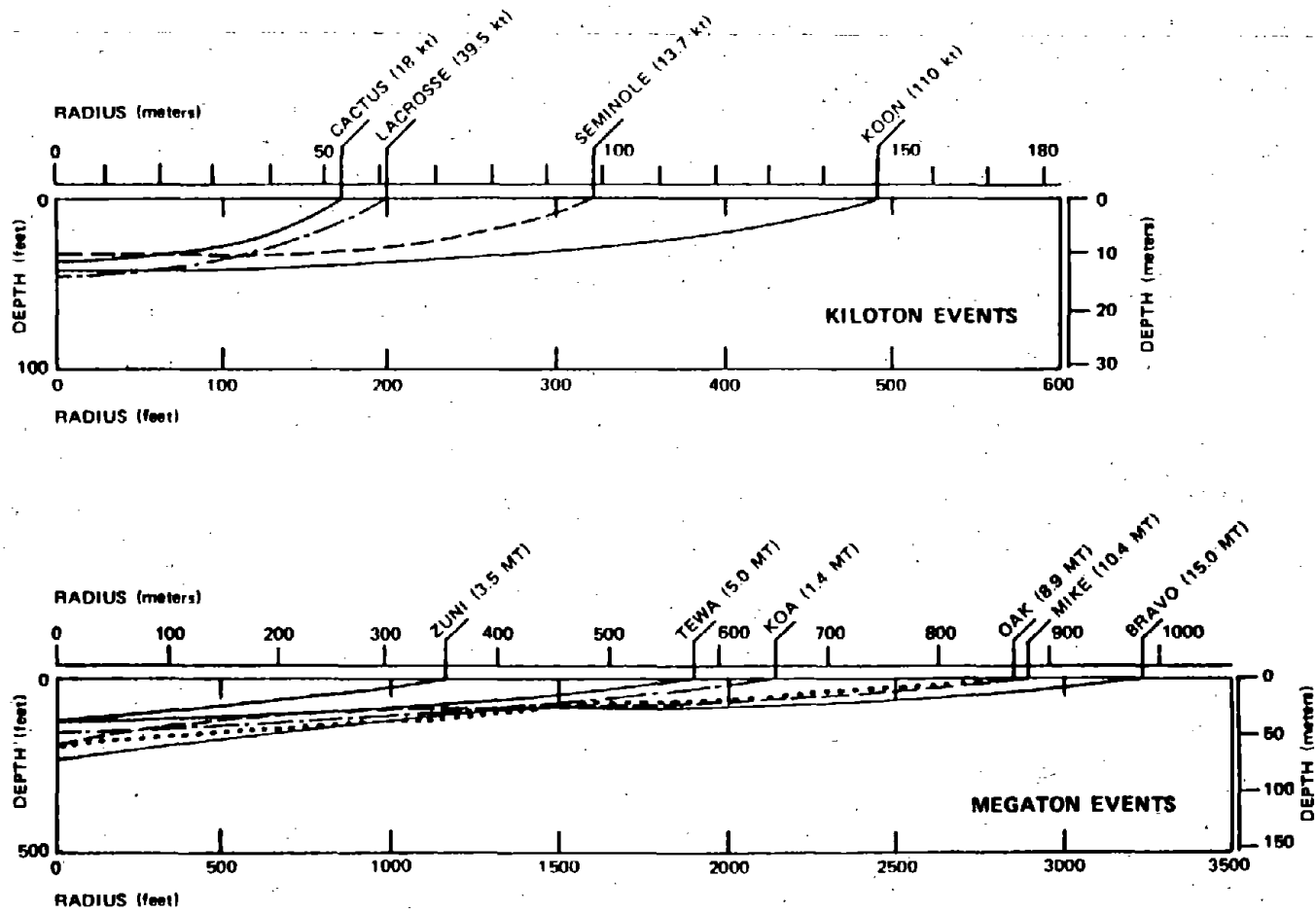


Figure 2-73. Typical Pacific Proving Ground Crater Profiles

In the shallow-buried region where the $DOB/W^{1/3}$ is less than $5 \text{ m/kt}^{1/3}$, the yield scaling exponent, α , is a function of depth of burial.* It is in this region that an interpolation procedure is required to determine α , as will be discussed in paragraph 2-49.

The near-surface region ($HOB/W^{1/3} \leq 3 \text{ m/kt}^{1/3}$ to $DOB/W^{1/3} \leq 5 \text{ m/kt}^{1/3}$) and the buried burst ($DOB/W^{1/3} > 5 \text{ m/kt}^{1/3}$) region will be examined separately in the succeeding paragraphs. Five generic geologies have been chosen to describe the effect of various homogeneous media on cratering efficiency.

2-49 Volume of Craters from Surface and Near-Surface Bursts
 $(HOB/W^{1/3} \leq 3 \text{ m/kt}^{1/3}$ to
 $DOB/W^{1/3} \leq 5 \text{ m/kt}^{1/3})$

Figures 2-74a through 2-75e show the apparent crater volume, as a function of height of burst,† for a near-surface 1 kt explosion in various homogeneous generic geologies. Figures 2-74a through 2-74e are valid for yields less than or equal to 1 kt and Figures 2-75a through 2-75e are valid for yields greater than 10 kt.

For yields between 1 and 10 kt, the crater volume may be estimated by using the best estimate curve of the appropriate geology for either 1 kt or 10 kt or a weighted average, depending upon the output characteristics of the warhead. The higher the radiative fraction, the

*Craters from detonations on the islands of the Pacific Proving Ground (Eniwetok and Bikini atolls) indicate that, for a saturated coral medium, the scaling exponent for the apparent crater radius may be greater than 1/3 and for the crater depth, smaller than 1/3. Until the reason that it is necessary to depart from cube-root scaling in saturated coral is understood, it will not be possible to determine similar departures in other media.

†In this group of figures, HOB is used to indicate both HOB and DOB, i.e., buried bursts are shown with a negative HOB.

closer the crater volume will be to the $W > 10 \text{ kt}$ curve. If, for example, it is known that a 3 kt weapon of interest has a high radiative output, the $W > 10 \text{ kt}$ curve should be used to determine the apparent crater volume. If, however, no information is available concerning the radiative output, the crater volume should be determined by interpolation, assigning a 60 percent weight to the $W \leq 1 \text{ kt}$ curve and 40 percent weight to the $W > 10 \text{ kt}$ curve, i.e., for a 3 kt weapon with no further information

$$V_a(3) = 0.6V_a(W \leq 1) + 0.4V_a(W > 10).$$

The yield scaling parameter, α , for near-surface bursts is determined as follows:

$$\frac{HOB}{W^{1/3}} \geq 0; \alpha = 0.333$$

$$-5 \leq \frac{HOB}{W^{1/3}} < 0 \text{ (m/kt}^{1/3}); \alpha = \text{(see Figure 2-76a).}$$

Once the value of α is known, the apparent scaled crater volume can be obtained from Figures 2-74a through 2-75e for a specified yield (W) and HOB/W^α in the appropriate geology. The value obtained by this procedure is the "best estimate" of the apparent crater volume for a 1 kt explosion (V_{a1}).

The crater volume for yields other than 1 kt may be obtained by the following scaling relation:

$$\frac{V_a}{V_{a1}} = W^{3\alpha},$$

where V_{a1} is the apparent crater volume for a 1 kt explosion, and V_a is the corresponding volume for a yield of W kt. The height of burst scaling relation is

$$\frac{HOB}{HOB_1} = W^\alpha,$$

where HOB_1 is the height of burst for a 1 kt explosion, and HOB is the corresponding height of burst for a yield of W kt.

The uncertainty in the crater volume for $W < 1$ kt is based on HE cratering results. It is assumed that the uncertainty is independent of geology and yield. The bounds shown in Figures 2-74a through 2-74e are not the results of a detailed statistical analysis. These bounds contain 95 percent of the experimental data, but statistical implications should not be drawn from this fact.

The best estimate for the $W > 10$ kt curve was determined by nuclear data from the Pacific Proving Ground. The lower bound was suggested by calculations, and was influenced by the fact that all the nuclear data were obtained from devices that were very dissimilar to modern weapons.

2-50 Crater Shapes and Dimensions for Surface and near-Surface Bursts

The shape of the crater from a near-surface burst must be known to determine the radius and depth from the crater volume and the explosive yield. The shape depends mainly on the yield, the scaled height of burst, and the geology. Table 2-8 shows the shape to be expected as a function of these three variables. The succeeding discussion provides the necessary scaling relationships to determine the dimensions for the various shapes. Separate procedures are provided for each of the yield/HOB combinations shown in Table 2-8.

Table 2-8. Classification of Crater Shapes from Near Surface Bursts as a Function of Yield, Height of Burst, and Geology

Yield	Scaled HOB (m/kt ^{1/3})	Geology	Crater Shape
$W < 1$ kt	All	All	Bowl
$W > 1$ kt	$HOB/W^{1/3} > 0$	All	Dish
$W > 1$ kt	$-5 < HOB/W^{1/3} < 0$	Unsaturated Saturated	Dish/Bowl Dish

a. $W < 1$ kt

The crater shape for near-surface bursts ($-5 \text{ m/kt}^{1/3} < HOB/W^{1/3} < 3 \text{ m/kt}^{1/3}$) in all geologies for $W < 1$ kt is best described as bowl-shaped. The dimensions of the apparent crater radius, R_a , and apparent crater depth (D_a) for these bursts are given by the following expressions:

$$1.1 V_a^{1/3} < R_a < 1.4 V_a^{1/3},$$

$$0.35 V_a^{1/3} < D_a < 0.7 V_a^{1/3}.$$

The best estimates for R_a and D_a are

$$R_a = 1.2 V_a^{1/3},$$

$$D_a = 0.5 V_a^{1/3},$$

where V_a = the best estimate apparent volume.

b. $W > 1$ kt

The crater shape for near-surface bursts in which $W > 1$ kt depends on the yield and HOB.

(1) $HOB/W^{1/3} \geq 0$.

For above-surface bursts ($HOB/W^{1/3} \geq 0$), in which $W > 1$ kt, the crater shape is best described as dish-shaped and the crater dimensions are determined by the expressions

$$1.1 W^{0.08} < \frac{R_a}{V_a^{1/3}} < 1.4 W^{0.08},$$

$$0.35 W^{-0.12} < \frac{D_a}{V_a^{1/3}} < 0.7 W^{-0.12}.$$

The best estimates for R_a and D_a are

$$\frac{R_a}{V_a^{1/3}} = 1.2 W^{0.08},$$

$$\frac{D_a}{V_a^{1/3}} = 0.5 W^{-0.12}.$$

where V_a = the best estimate apparent volume.

$$(2) HOB/W^{1/3} < 0$$

For near-surface buried events

$$\left(0 < \frac{DOB}{Wa} \leq 5 \text{ m/kt}^a\right),$$

in which $W' > kt$, the shape of the crater may be either "bowl" or "dish" in nature or some combination of the two extremes. Mechanisms such as compaction, rebound, bulking, slumping and layering effects play a significant role in the final crater shape. Cratering experience to date is not sufficient to make quantitative judgments regarding the impact of each mechanism.

The apparent crater dimensions for near-surface buried events are determined by the expressions

$$\frac{R_a}{V_a^{1/3}} = 1.2 W'^b \text{ meters,}$$

$$\frac{D_a}{V_a^{1/3}} = 0.5 W'^c \text{ meters.}$$

The values of the exponents (b, c), as a function of DOB, are found in Figures 2-76b and 2-76c. These exponents are necessary to ensure a smooth continuous curve for the radii of large yield (1 Mt) bursts as the depth of burial increases. Existing data indicate that above-surface bursts of high yield nuclear explosions produce dish-shaped craters and buried nuclear explosions produce bowl-shaped craters. However, since no data exist in the region

$$0 < \frac{DOB}{Wa} \leq 5 \text{ (m/kt}^a\text{)},$$

it is necessary to provide a transition region in which the crater produced is neither dish-shaped nor bowl-shaped, but some intermediate of the two extremes. The above equations produce this smooth transition region for the crater dimensions.

It has been noted, however, that in highly saturated media slope failure and/or liquefaction can produce a shallow crater for buried events. High explosive tests conducted at Fort

Polk, Louisiana are good examples of these phenomena.

Other pertinent crater dimensions may be related to the above dimensions as follows:

- The radius to the crater lip crest is

$$R_{LR} = 1.25R_a.$$

- The height of the apparent lip is

$$.25D_a < H_{LR} < .33D_a$$

(near-surface bursts).

A summary of the procedures for calculating craters from near-surface bursts is given on page 2-161, immediately preceding the applicable figures.

2-51 Dimensions of Craters from Deep-Buried Explosions

Cratering experiments with chemical explosives (HE) and nuclear explosions (NE) suggest that linear dimensions of craters from buried explosions scale according to a modified overburden rule. This scaling rule is somewhat cumbersome to use for the computation of crater dimensions, and the available data do not conclusively prove the validity of any single scaling rule. Therefore, a simplified yield scaling exponent, yield (kt) to the 1/3.4 power, has been chosen for scaling apparent crater dimensions for scaled DOBs greater than 5 m/kt^{1/3}. Figures 2-77 through 2-81 may be used to obtain apparent crater volumes for buried bursts in each of the soil types indicated. The curves in these figures are valid for *all* yields. The uncertainty in crater volume is independent of geology and yield, and is based on HE cratering results.

Crater radius and depth are given by the following expressions

$$1.1 V_a^{1/3} < R_a < 1.4 V_a^{1/3},$$

$$0.35 V_a^{1/3} < D_a < 0.7 V_a^{1/3}.$$

[REDACTED]

These expressions are valid for deep-buried bursts in *all* geologies for *all* yields. The best estimates for the crater dimensions are

$$R_a = 1.2 V_a^{1/3},$$

$$D_a = 0.5 V_a^{1/3},$$

where V_a is the best estimate of the apparent volume.

It is possible that slumping of the walls will produce a wide, shallow crater for some yield-DOB combinations in a saturated geology. The resulting crater shape is neither "bowl" nor "dish" in nature; it is some combination of the two. The only explosions to date that resulted in such occurrences in the craters have been in a very wet clay soil with the explosive charge at or near the optimum depth of burial.

The uncertainty in crater dimensions obtained from the expressions given above is, however, approximately correct for any specified crater volume. If the crater volume is chosen as the lower or upper uncertainty band from Figures 2-77 through 2-81, then the expressions for the radius and depth are still valid. A new range of crater dimensions is determined by using the equations and the chosen volume.

Figure 2-82 contains the best estimate prediction for high-explosive detonations in the five generic homogeneous geologies. These curves show the relative crater volumes for the geologies. The curves can be used as a guide as to the proper nuclear curve to use for a new or unknown geology. If some HE cratering data are available, the curves of Figure 2-82 can be used to determine which homogeneous geology is best for the problem. This figure should not be used to calculate crater volume for nuclear explosions.

Other pertinent crater dimensions may be related to the above dimensions as follows:

- The radius to the crater lip crest is

$$R_{ar} = 1.25R_a.$$

- The height of the apparent lip is

$$.20D_a < H_{ar} < .25D_a \\ \text{(deep-buried bursts).}$$

A summary of the procedures for calculating craters from deep-buried bursts is given on page 2-179, immediately preceding the applicable figures.

[REDACTED]

SUMMARY OF PROCEDURES FOR CALCULATING CRATERS FROM NEAR-SURFACE BURSTS ($-5 \text{ m/kt}^{1/3} < \text{HOB}/W^{1/3} < 3 \text{ m/kt}^{1/3}$)

Figures 2-74a through 2-75e and 2-76a, b and c, together with appropriate scaling laws, may be used to obtain crater volumes and dimensions from near-surface bursts in a variety of situations. The following summary provides a step-by-step procedure for obtaining such information. Example problems are provided on the pages immediately following the figures.

Required (either given or estimated)

Yield (W) in kt

Actual HOB or DOB (may be zero if required)

Soil type (one of the five generic types or a combination; see Figure 2-86b).

1. Determine yield scaling parameter, a , for burst position:

a. $\text{HOB}/W^{1/3} \geq 0 \rightarrow a = 1/3 \cong 0.333$,

b. $0 < \text{DOB}/W^{1/3} \leq 5 \text{ m/kt}^{1/3} \rightarrow a$ from Figure 2-76a.

2. Compute HOB_1 (HOB for 1 kt) = $\frac{\text{Actual HOB}}{W^a}$

or DOB_1 (DOB for 1 kt) = $\frac{\text{Actual DOB}}{W^a}$

3. Determine V_{a1} (apparent-crater volume for 1 kt):

a. If $W \leq 1$ kt, use curve for given soil type from Figures 2-74a through 2-74e.

b. If $W > 10$ kt, use curve for given soil type from Figures 2-75a through 2-75e.

c. If $1 \text{ kt} < W \leq 10 \text{ kt}$, with *low or unknown* radiative output, interpolate using $V_{a1} = 0.6 V_{a1}$ (from $W \leq 1$ kt curve) + $0.4 V_{a1}$ (from $W > 10$ kt curve).

d. If $1 \text{ kt} < W \leq 10 \text{ kt}$ with *known high* radiative output, use curve for given soil type from Figures 2-75a to 2-75e.

4. Compute V_a (actual crater volume for yield other than 1 kt):

$$V_a \text{ (actual volume)} = V_{a1} (W^{3a}).$$

These curves are provided for each soil type: best estimate, upper bound, and lower bound. Using the following guidelines, select the curve most appropriate to the problem.

a. Use *best estimate* V_{a1} if no specific geologic data are given. If actual HE tests are available for a specific site, compare them with the HE curves in Figure 2-82, and move toward the upper or lower bound NE curve to adjust for these data, depending on where the data are grouped.

b. Use *lower bound* V_{a1} (if desirable) for target-oriented calculations (offensive-conservative) to calculate R_a or D_a . Consider lower-bound V_{a1} for targeting when calculating crater volume-related phenomena, such as ejecta, transient velocity or displacement.*

c. Use *upper-bound* V_{a1} (if desirable) for design-oriented calculations (defense-conservative) to calculate R_a or D_a . Consider upper bound V_{a1} for design when calculating crater-related phenomena affected by volume.

d. For $W > 10$ kt, the discrepancy between the theoretical calculations and the empirical data in our understanding of the energy coupling produced by modern weapons detonated at low HOBs or in contact with the earth (HOB = 0.5 m)

*In all instances it is recommended that upper and lower bound values be calculated in order to gain an appreciation of the effects of uncertainties on the particular problem under consideration.

must be considered. (See paragraph 2-49.) Since this discrepancy only occurs in the lower-bound V_a values, it principally influences targeting, or offensive-conservative, problems.

It is recommended that the lower-bound V_a values be considered in calculating kill probabilities (P_k) due to the crater, but that high credence in cratering P_k not be used in assessing overall system P_k .

Note: This cratering discrepancy is a systematic uncertainty and should not be treated as a random uncertainty.

5. Calculate R_a and D_a using the expression from the following table that fits the yield and HOB and inserting the appropriate V_a :

Yield	Near-Surface Bursts	
	Above Surface ($\frac{HOB}{W^{1/3}} \geq 0$)	Below Surface ($\frac{DOB}{W^{1/3}} \leq 5 \text{ m/kt}^{1/3}$)
$W \leq kt$	$R_a = 1.2 V_a^{1/3}$ $D_a = 0.5 V_a^{1/3}$	same same
$W > 1 \text{ kt}^*$	$R_a = 1.2 W^{0.08} V_a^{1/3}$ $D_a = 0.5 W^{-0.12} V_a^{1/3}$	$R_a = 1.2 W^b V_a^{1/3}$ $D_a = 0.5 W^{-c} V_a^{1/3}$

*See Figures 2-76b and 2-76c for determining b and c.

The dimensions R_a , D_a , and V_a can be related to other pertinent crater dimensions as follows:

- The radius to the crest of the apparent-crater lip is

$$R_{al} = 1.25 R_a$$

- The height of the apparent lip is

$$0.25 D_a \leq H_{al} \leq 0.33 D_a$$

for near-surface bursts.†

Variations in the thickness of the ejecta as a function of range from the surface ground zero (SGZ) are discussed in paragraphs 2-52 and 2-53.

†An exception to this is a similar crater formed by an explosion at the Pacific Proving Ground. The crater had no lip and greatly reduced ejecta. It is thought that such a crater shape may have been the result of a late-time reconsolidation/liquefaction process, which caused the crater lip to be below the water surface.

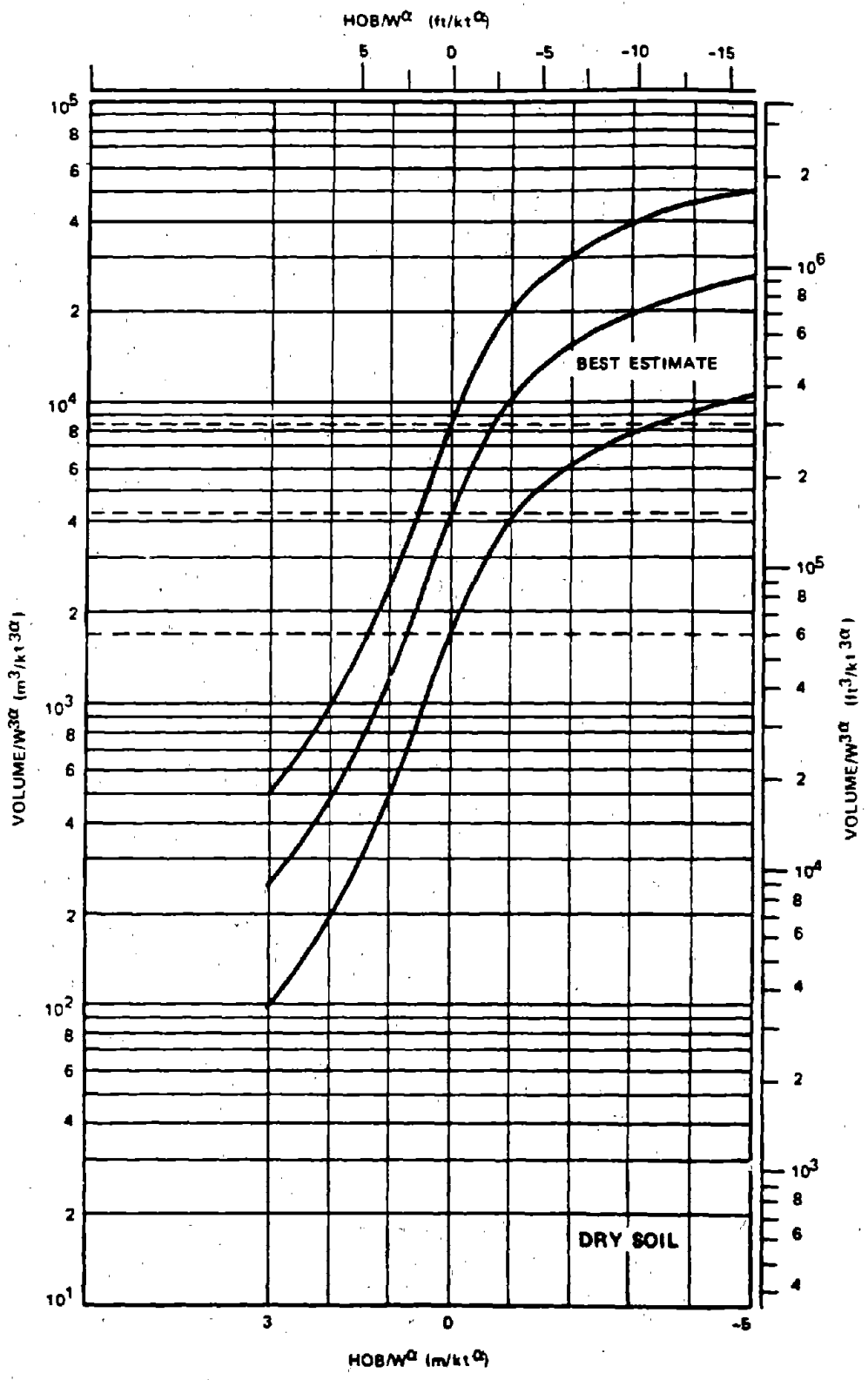
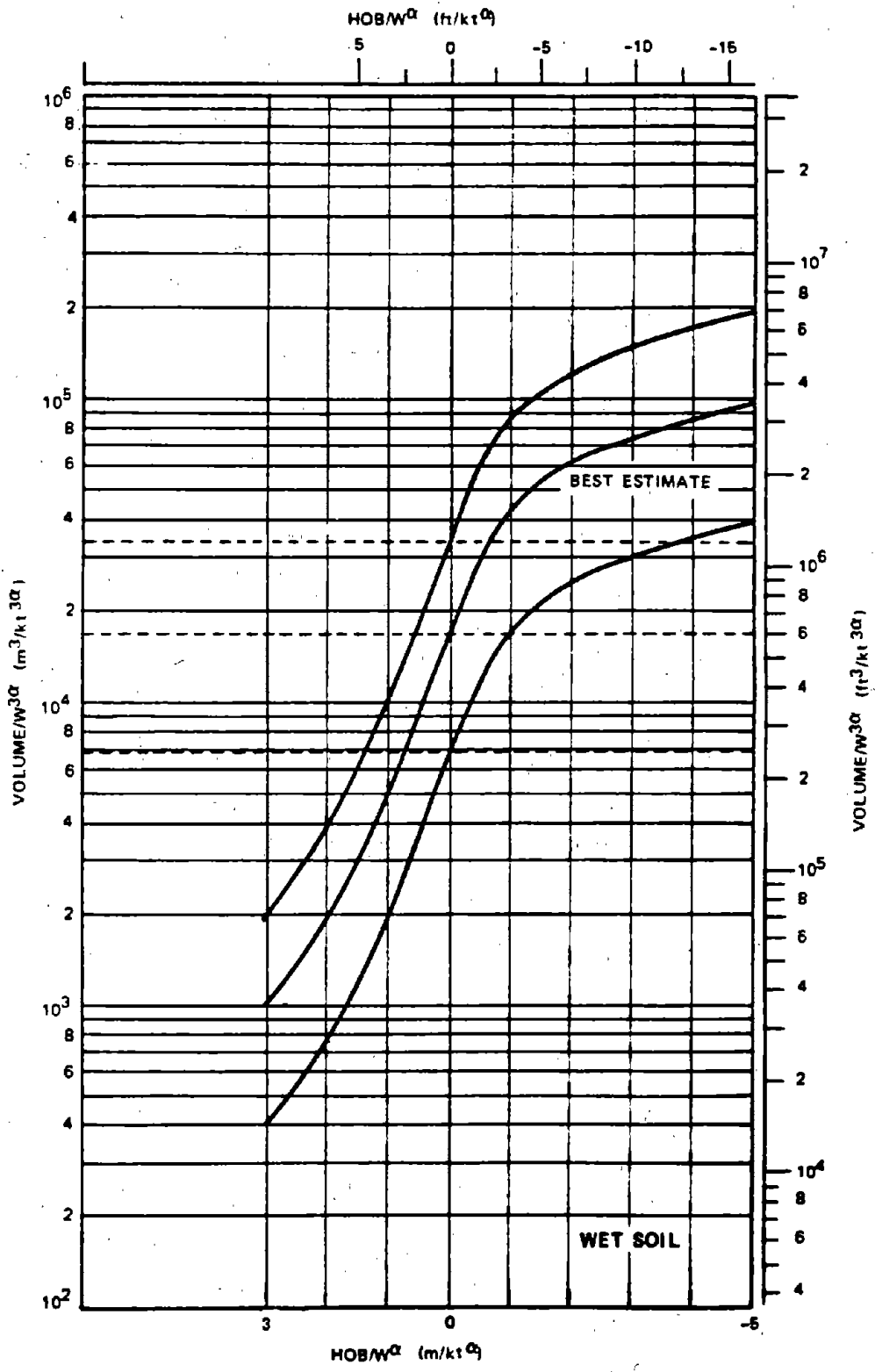


Figure 2-74a. Apparent Crater Volume for a 1-Kiloton Near-Surface Explosion in Dry Soil; Applicable for $W \leq 1$ kt



2-164

Figure 2-74b. Apparent Crater Volume for a 1-Kiloton Near-Surface Explosion in Wet Soil; Applicable for $W \leq 1$ kt

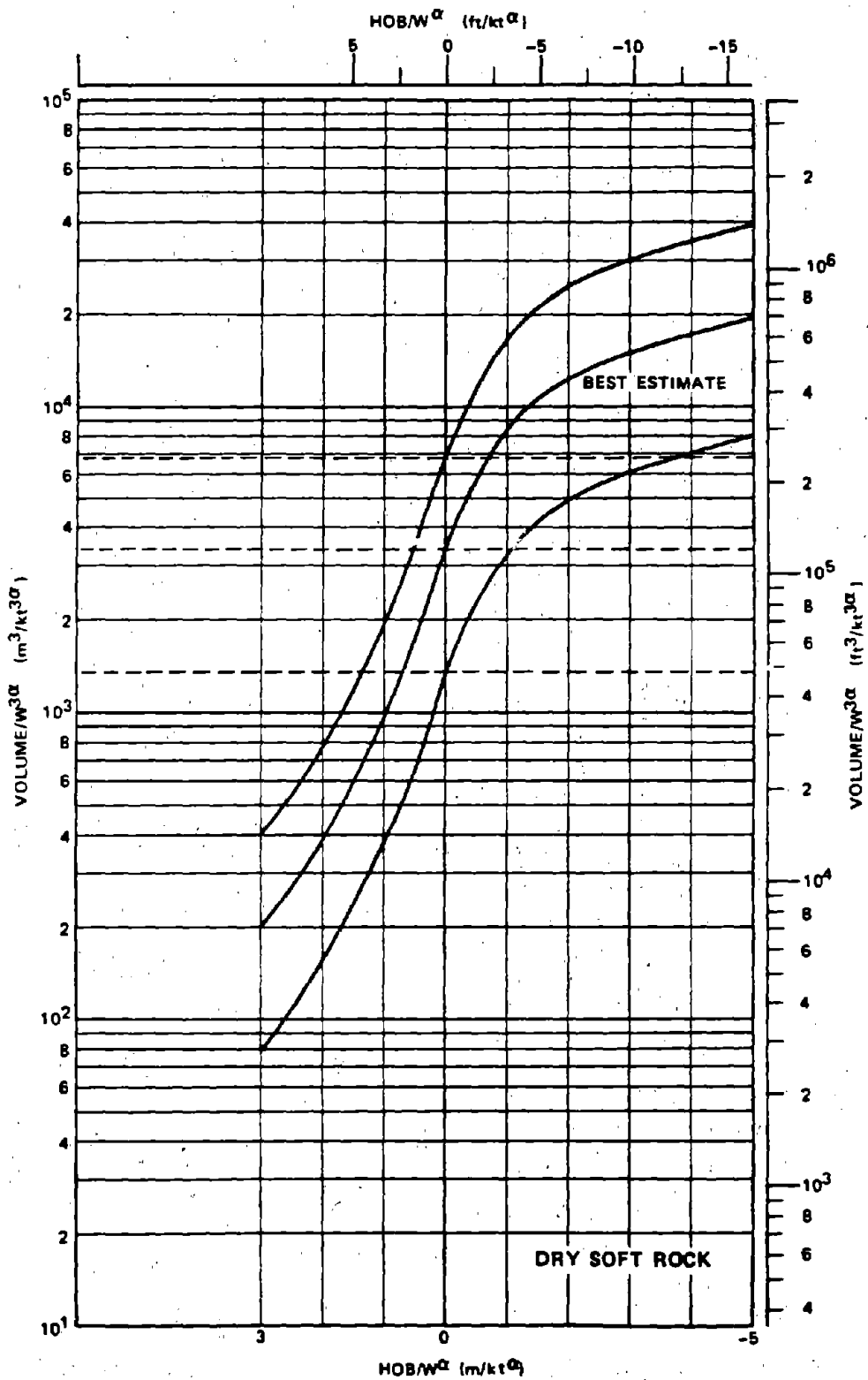
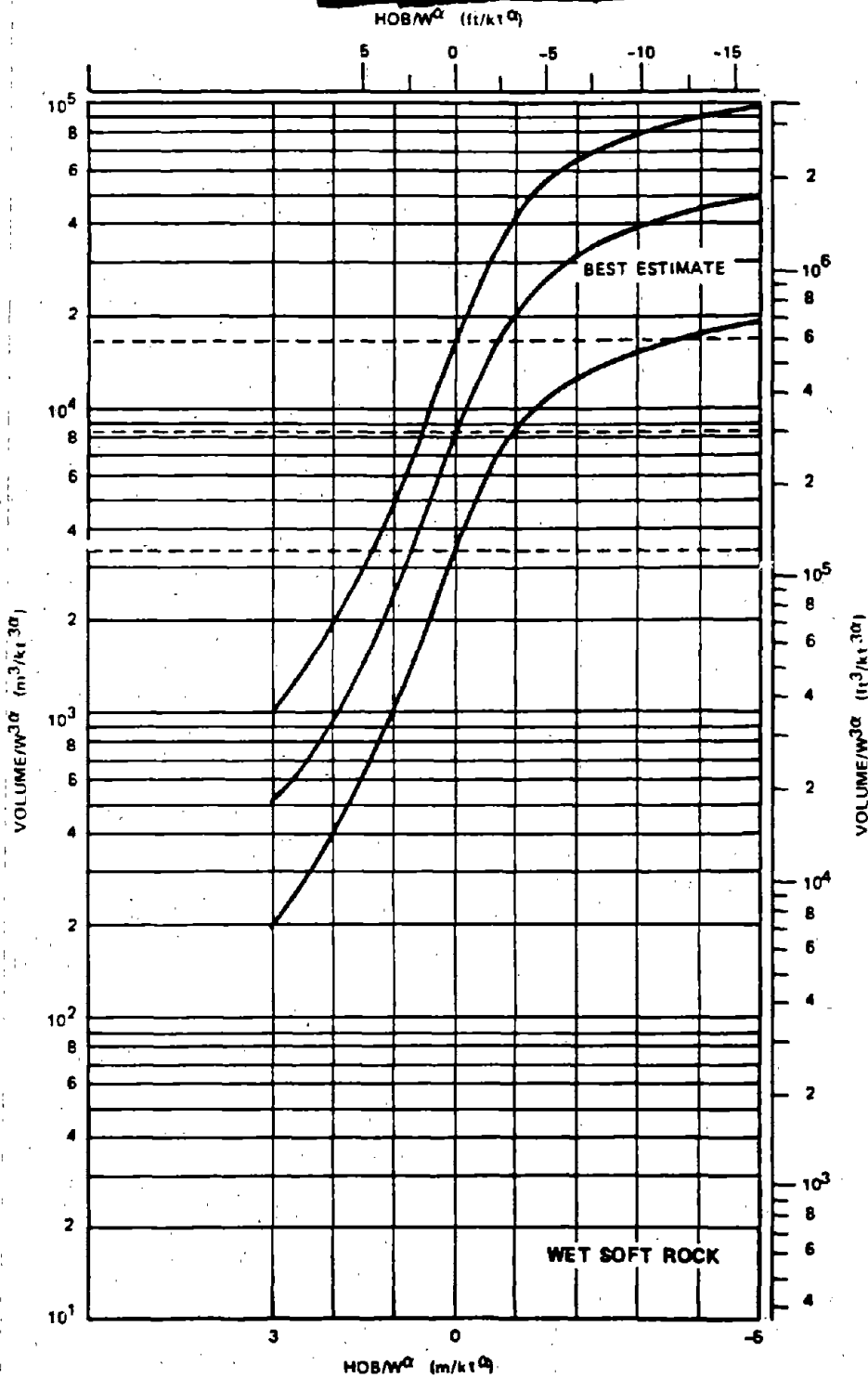


Figure 2-74c. Apparent Crater Volume for a 1 Kiloton Near-Surface Explosion in Dry Soft Rock; Applicable for $W \leq 1$ kt



2-166

Figure 2-74d. Apparent Crater Volume for a 1-Kiloton Near-Surface Explosion in Wet Soft Rock; Applicable for $W \leq 1$ kt

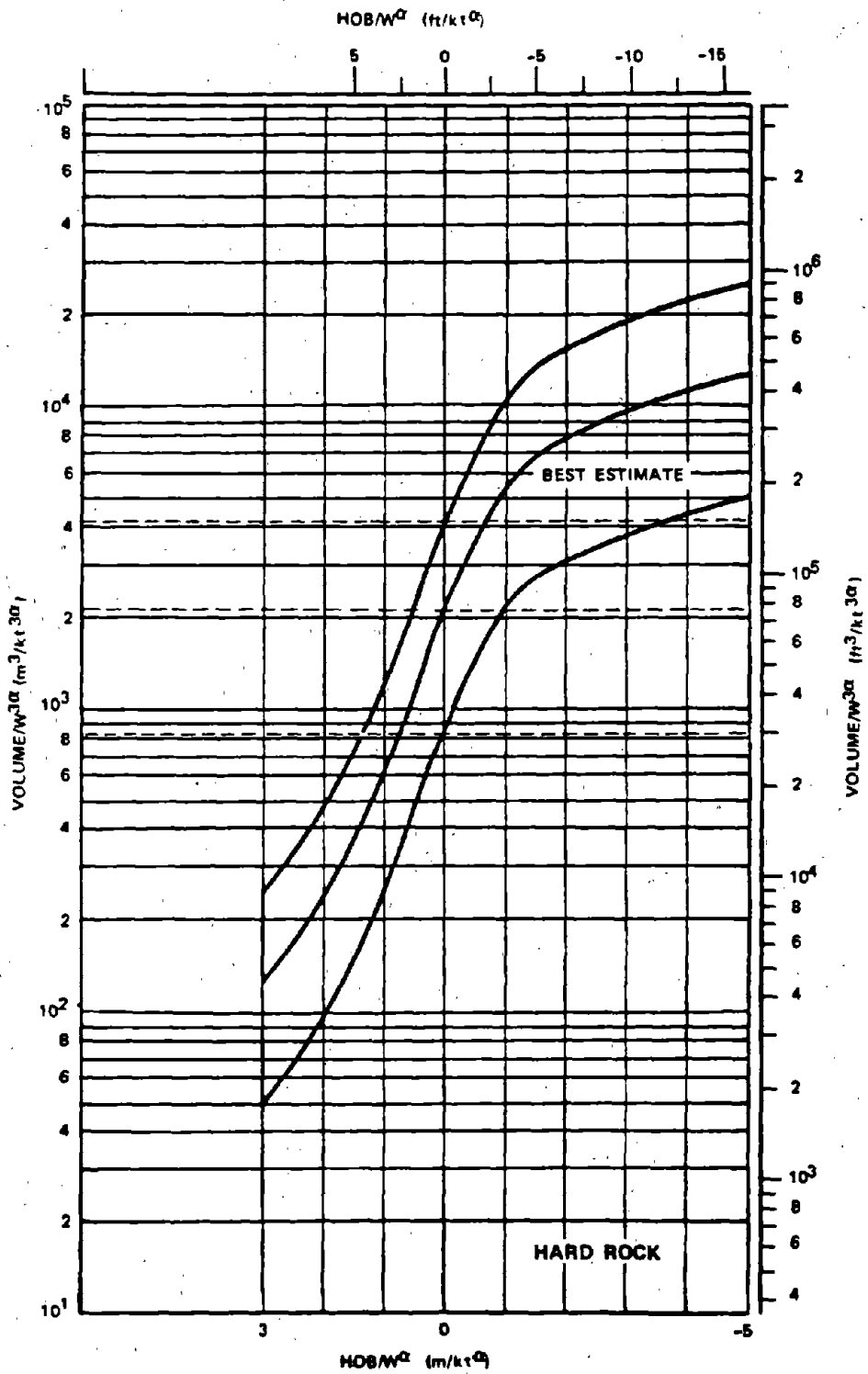
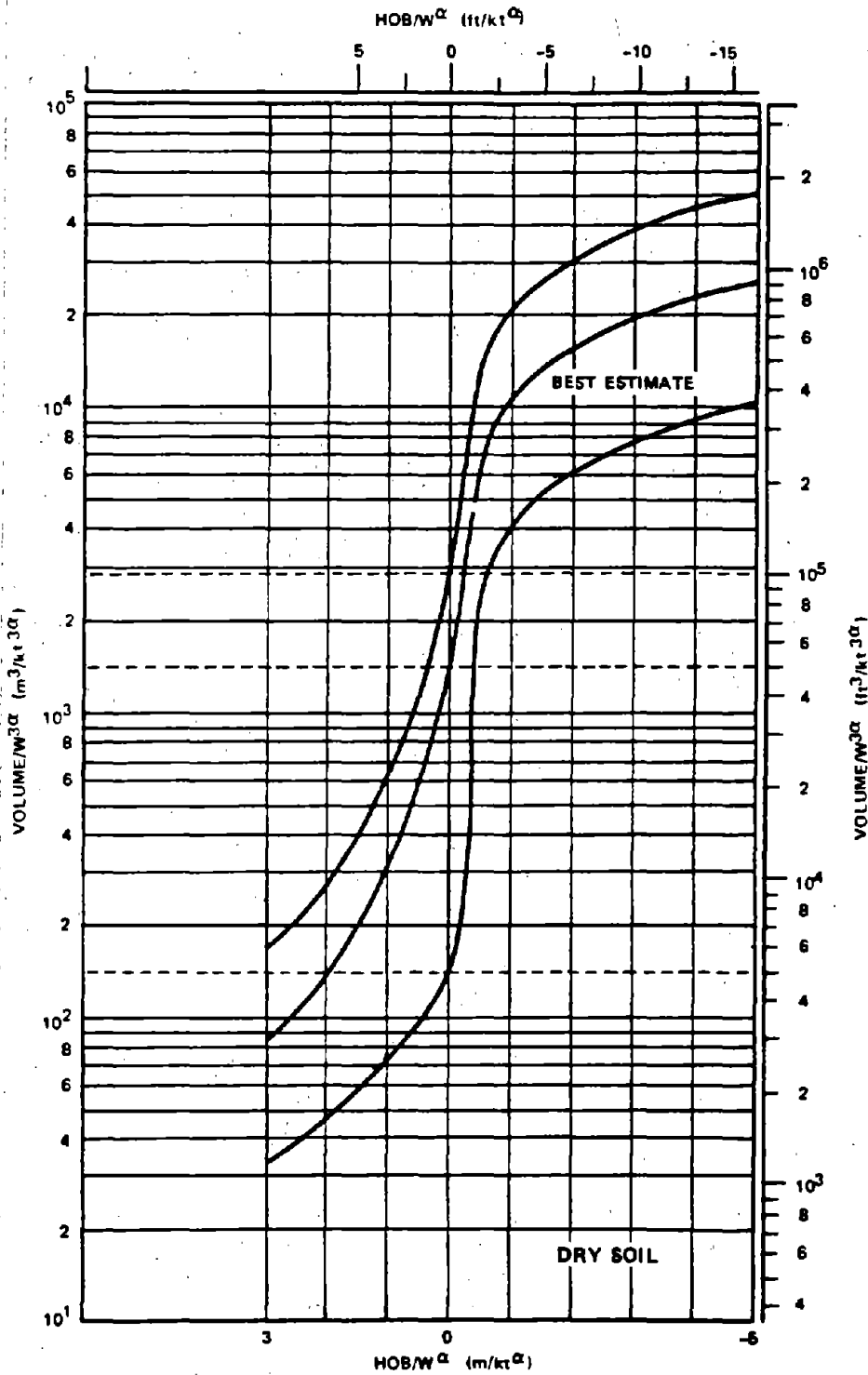


Figure 2-74e. Apparent Crater Volume for a 1 Kiloton Near-Surface Explosion in Hard Rock; Applicable for $W \leq 1$ kt



2-168

Figure 2-75a. Apparent Crater Volume for a 1 Kiloton Near-Surface Explosion in Dry Soil; Applicable for $W > 10$ kt

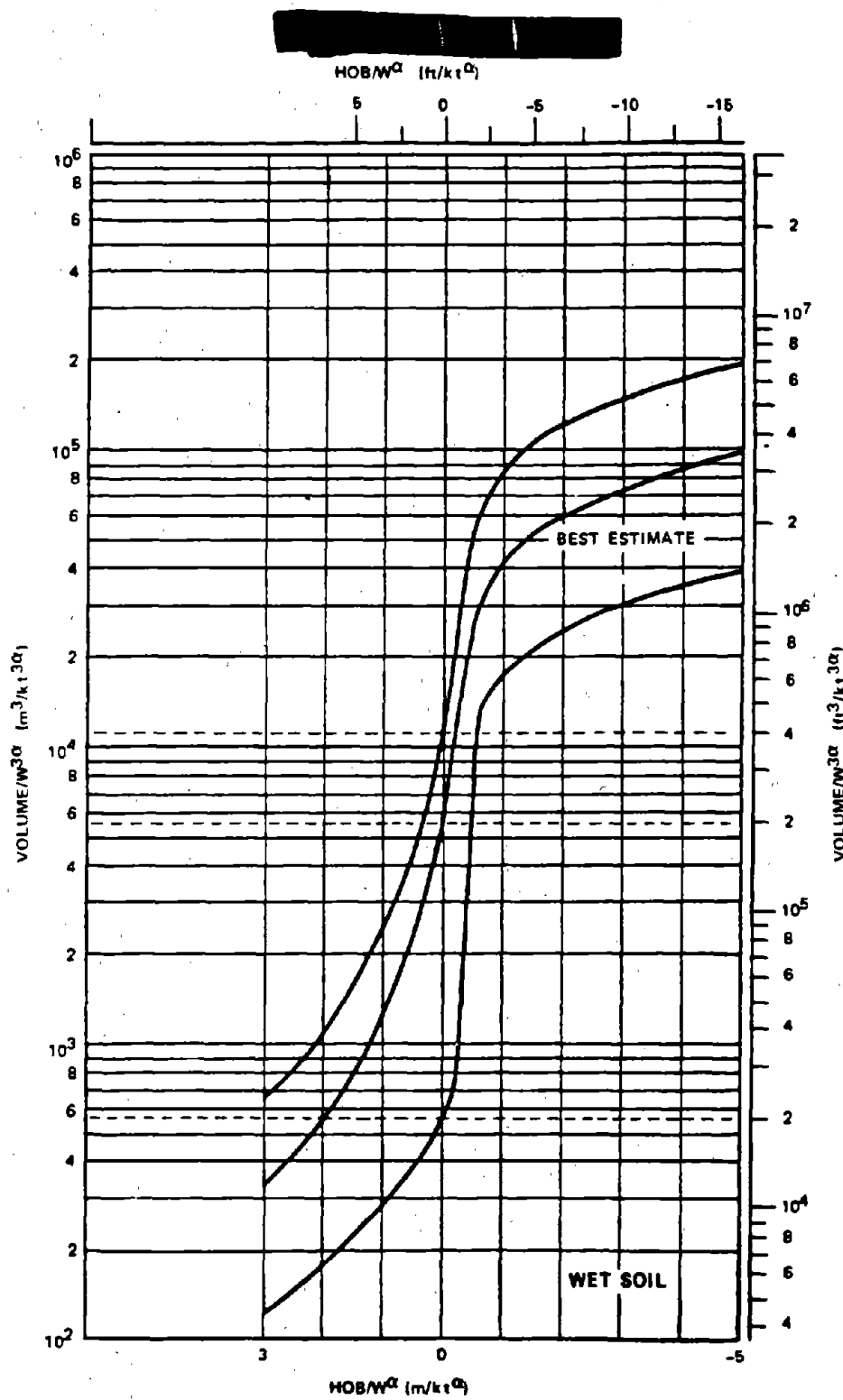
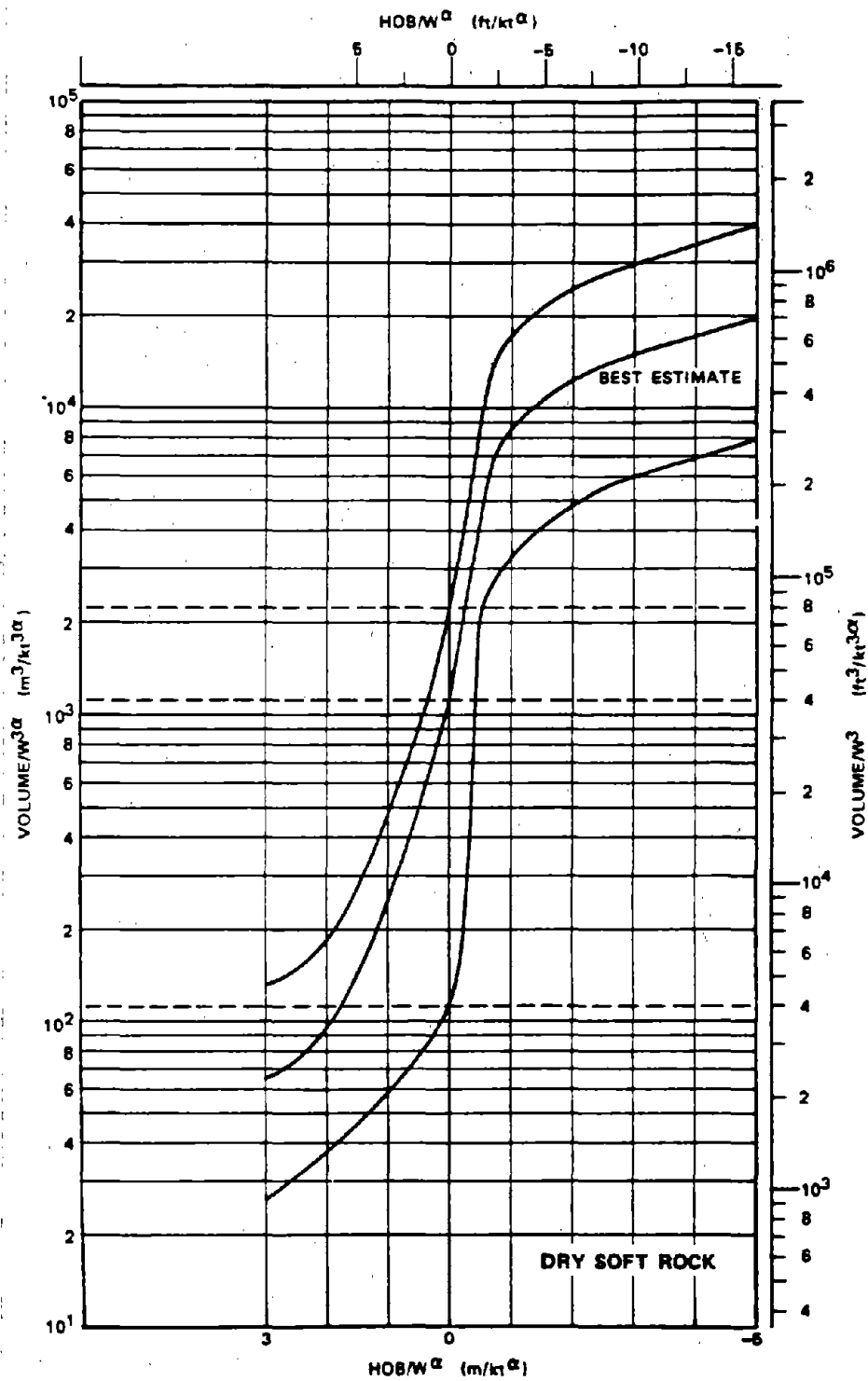


Figure 2-75b. Apparent Crater Volume for a 1 Kiloton Near-Surface Explosion in Wet Soil; Applicable for $W > 10$ kt



2-170

Figure 2-75c. Apparent Crater Volume for a 1 Kiloton Near-Surface Explosion in Dry Soft Rock; Applicable for W > 10 kt

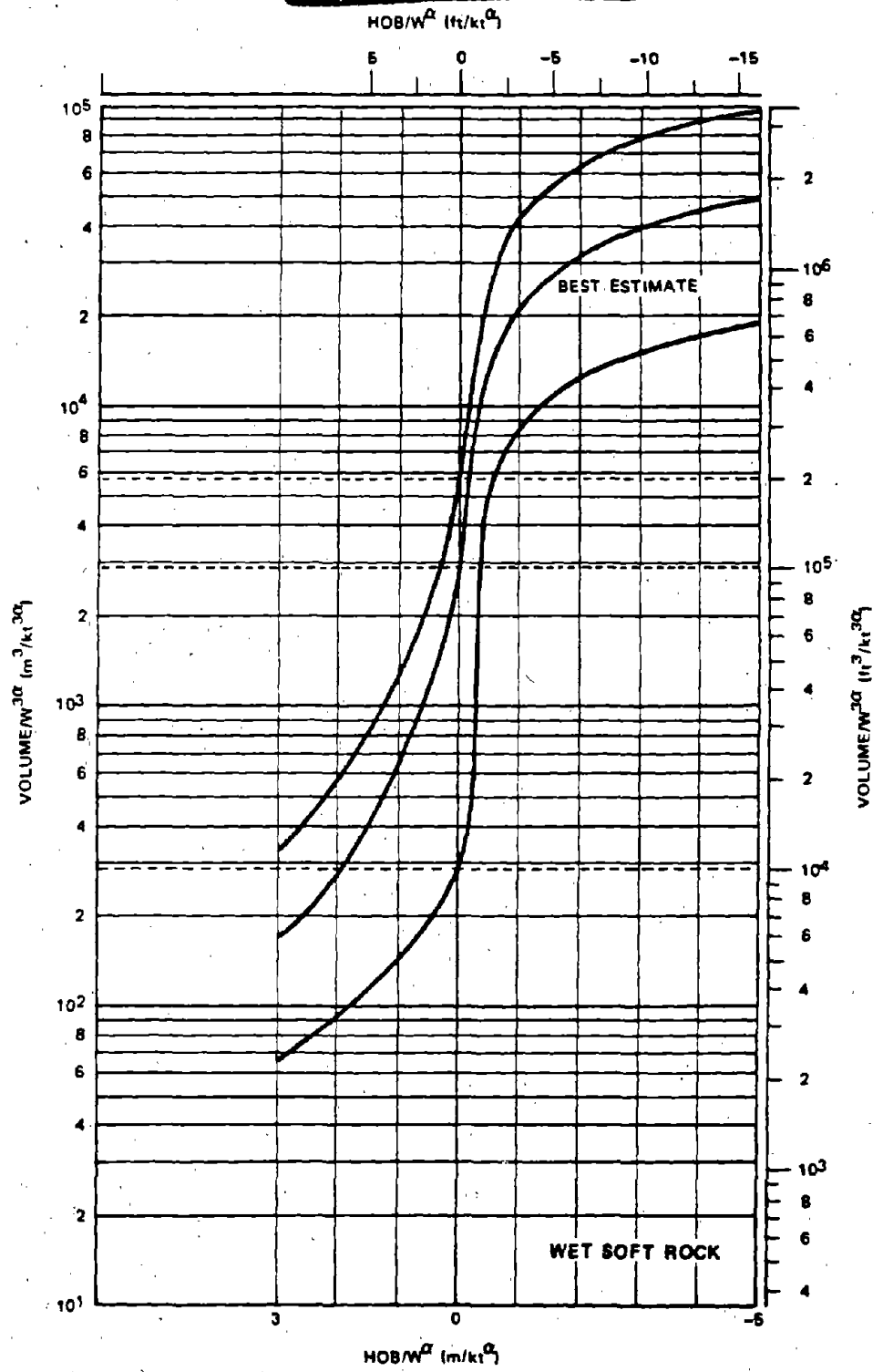
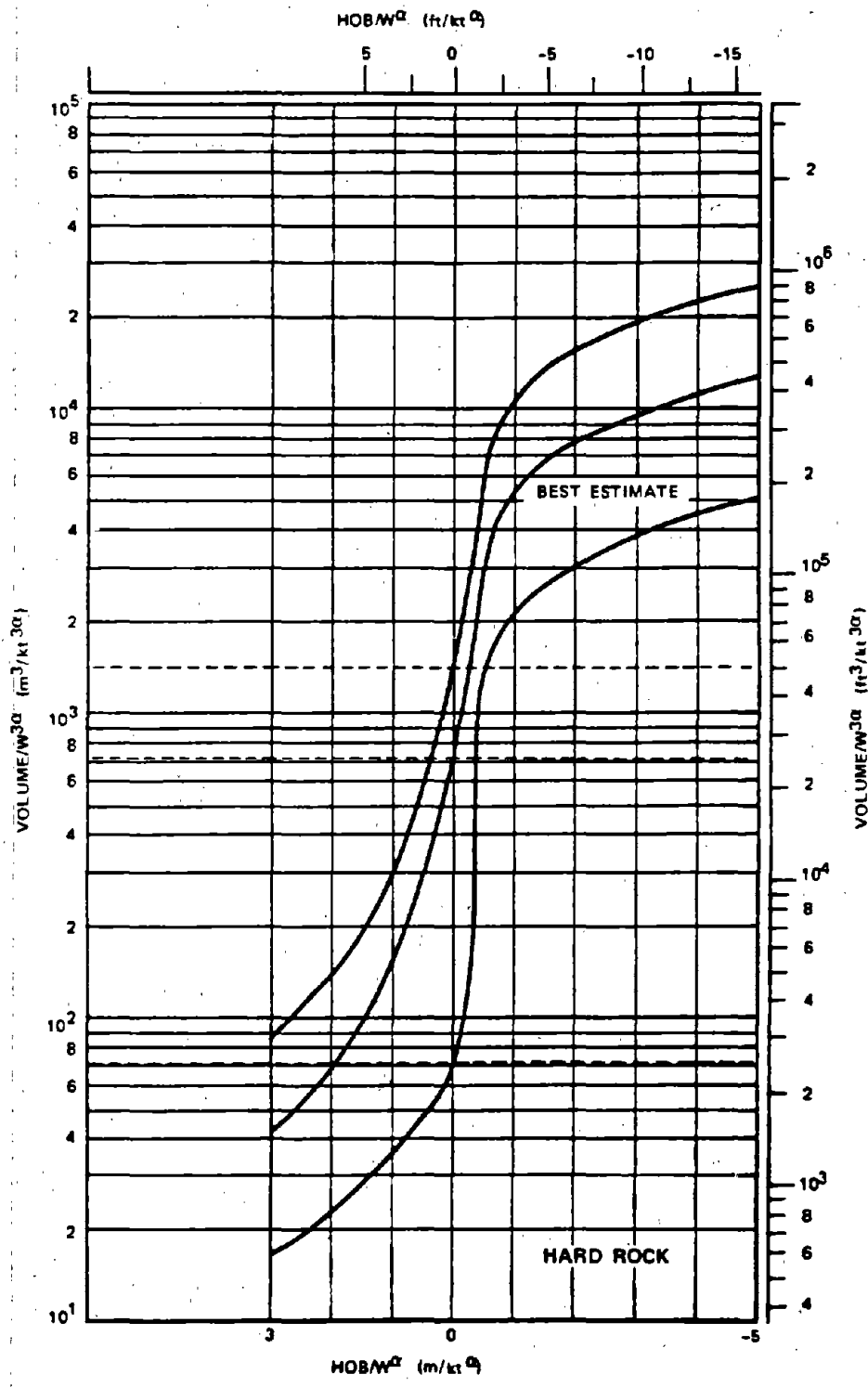


Figure 2-75d. Apparent Crater Volume for a 1-Kiloton Near-Surface Explosion in Wet Soft Rock; Applicable for $W > 10$ kt



2-172

Figure 2-75e. Apparent Crater Volume for a 1 Kiloton Near-Surface Explosion in Hard Rock; Applicable for W > 10 kt

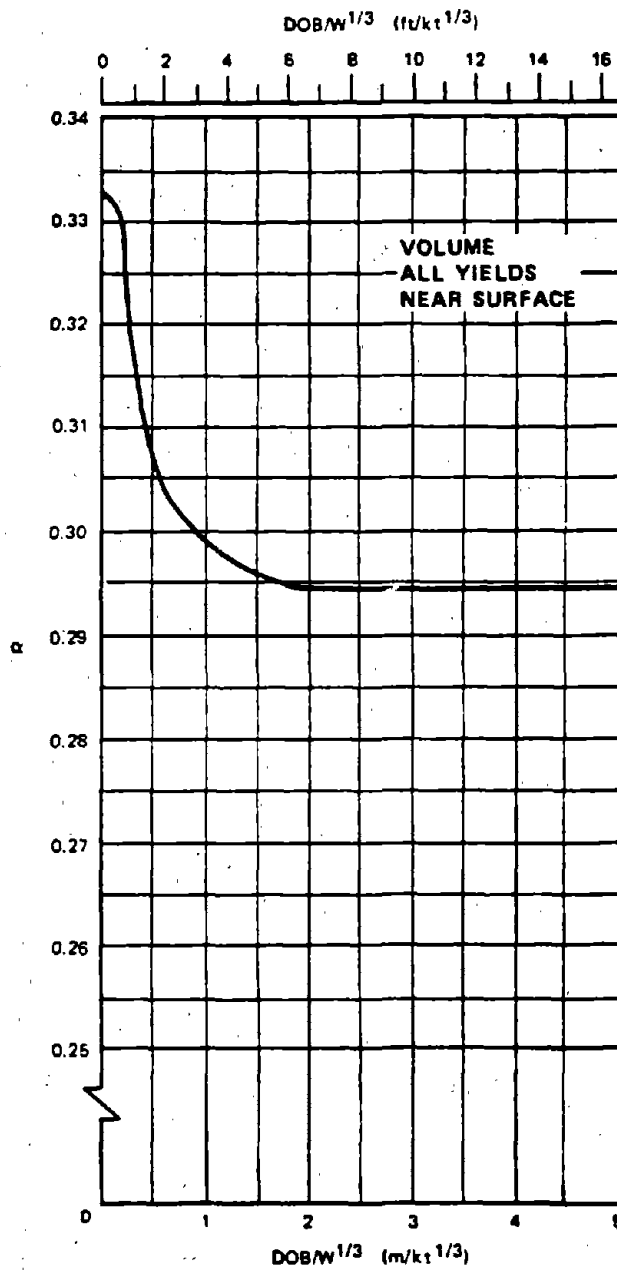
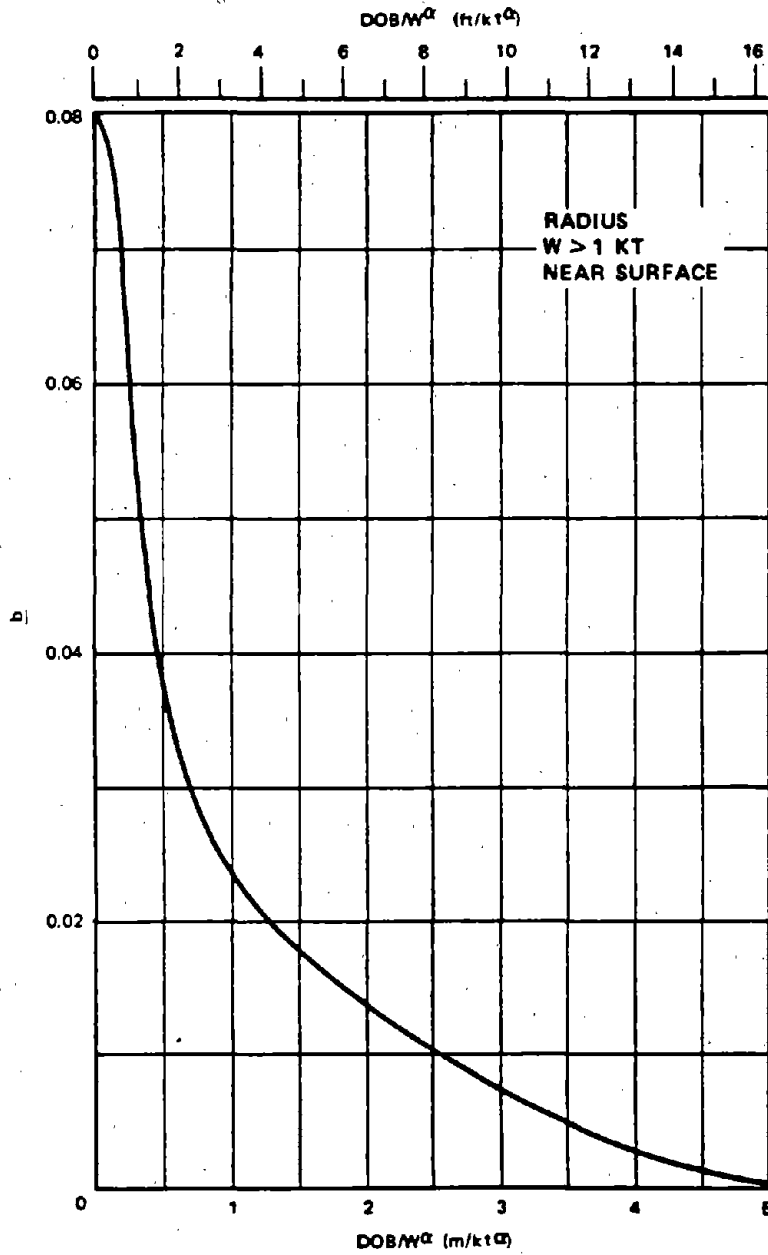


Figure 2-76a. Volume Scaling Exponent, α , as a Function of Scaled DOB for Near-Surface Explosions, All Yields



2-174

Figure 2-76b. Yield Transition Exponent, b, for Calculation of the Radius of Near-Surface, Buried Explosions W > 1 kt

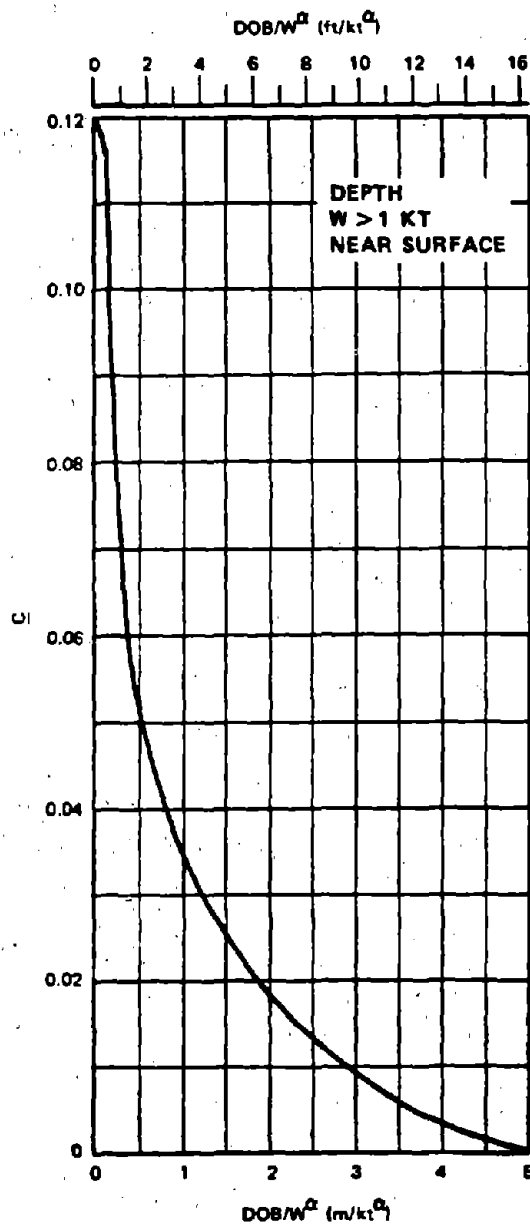


Figure 2-76c. Yield Transition Exponent, c , for Calculation of the Depth of Near-Surface, Buried Explosions, $W > 1$ kt

[REDACTED]

**Problem 2-22. Crater Dimensions for Above-Surface Bursts
(HOB > 0)**

Figures 2-74a through 2-75e include curves that indicate the apparent crater volume as a function of HOB for a 1 kt explosion in various homogeneous media.

Scaling: For yields other than 1 kt, the crater volume scales as follows:

$$V_{a1} = W^{3\alpha},$$

where V_{a1} is the apparent crater volume for a 1 kt explosion, and V_2 is the corresponding volume for a yield of W kt. The height of burst scales as

$$\frac{\text{HOB}}{\text{HOB}_1} = W^\alpha$$

Example:

Given: A hypothetical 300 kt contact burst on dry soil.

Find: The apparent crater radius and depth.

Solution: The HOB for a contact nuclear explosion is 0.5 meters. From paragraph 2-49,

$$\alpha = 0.3333$$

for $\text{HOB} \geq 0$. Therefore,

$$\text{HOB}_1 = \frac{\text{HOB}}{W^\alpha} = \frac{0.5}{(300)^{1/3}} = 0.075 \text{ m/kt}^{1/3}.$$

From Figure 2-75a, the apparent crater volume for a 1 kt explosion at a scaled HOB of 0.075 m/kt^{1/3} in dry soil is

$$V_{a1} = 1.25 \times 10^3 \text{ m}^3/\text{kt}^{3\alpha}$$

$$V_2 = V_{a1} (W)^{3\alpha} = 1.25 \times 10^3 (300)^{1.0} = 3.75 \times 10^5 \text{ m}^3.$$

Answer: The dimensions of the crater for a 300 kt contact burst are

$$\frac{R_2}{V_2^{1/3}} = 1.2 W^{0.08} = 1.2 (300)^{0.08} = 1.89,$$

$$R_2 = 1.89 (V_2)^{1/3} = 1.89 (3.75 \times 10^5)^{1/3} = 137 \text{ meters},$$

and

$$\frac{D_2}{V_2^{1/3}} = 0.5 W^{-0.12} = 0.5 (300)^{-0.12} = 0.252,$$

$$D_2 = 0.252 (V_2)^{1/3} = 0.252 (3.75 \times 10^5)^{1/3} = 18.2 \text{ meters}.$$

Uncertainty. The dimensions of the apparent crater obtained for the above problem have a range of uncertainties that are defined by the following:

$$1.1 W^{0.08} \leq \frac{R_2}{V_2^{1/3}} \leq 1.4 W^{0.08}$$

$$125 \leq R_2 \leq 159 \text{ meters},$$

and

$$0.35 W^{-0.12} \leq \frac{D_2}{V_2^{1/3}} \leq 0.7 W^{-0.12}$$

$$13 \leq \frac{D_2}{V_2^{1/3}} \leq 25 \text{ meters}.$$

The characteristics of the medium represent a major uncertainty in the crater data presented in Figure 2-74a through 2-75e. Details concerning material properties and geologic structure are not usually known about any particular site, but, in many cases small changes in these media characteristics can cause large changes in crater dimensions. The largest changes usually occur in the presence of an intersecting water table or a layered medium. Therefore, the range of uncertainty for a generic geology such as "wet soil" can be quite large, especially in the prediction of the apparent crater depth.

Related Material: See paragraphs 2-46 through 2-50; see also paragraphs 1-14 and 1-33.

[REDACTED]

Problem 2-23. Crater Dimensions for a Shallow Buried Burst

Figures 2-74a through 2-75e include curves that indicate the apparent crater volume as a function of HOB for 1 kt explosion in various homogeneous media.

Scaling: For yields other than 1 kt, the crater volume scales as follows:

$$\frac{V_a}{V_{a1}} = W^{3a}$$

where V_{a1} is the apparent crater volume for a 1 kt explosion, and V_a is the corresponding volume for a yield of W kt. The height of burst scales as

$$\frac{HOB}{HOB_1} = W^a$$

Example:

Given: A hypothetical 30 kt burst in wet soft rock at a depth of burial of 3 meters.

Find: The apparent crater radius and depth.

Solution: The value of a is obtained from Figure 2-76a, which must be entered with the scaled DOB.

The scaled DOB is

$$\frac{DOB}{W^{1/3}} = \frac{3}{(30)^{1/3}} = 0.965 \text{ m/kt}^{1/3}$$

From Figure 2-76a,

$$a = 0.299$$

The scaled HOB is

$$HOB_1 = \frac{HOB}{W^a} = \frac{-3}{(30)^{0.299}} = -1.09 \text{ m/kt}^a$$

From Figure 2-75d., the apparent crater volume for a 1 kt explosion, at $HOB = -1.09 \text{ m/kt}^a$ in wet soft rock, is,

$$V_{a1} = 2.20 \times 10^4 \text{ m}^3/\text{kt}^{3a}$$

and

$$\begin{aligned} V_a &= V_{a1} (W)^{3a} = 2.20 \times 10^4 (30)^{0.897} \\ &= 4.65 \times 10^5 \text{ m}^3 \end{aligned}$$

The dimensions for the 30 kt explosion are determined from the following expressions:

$$\frac{R_a}{V_a^{1/3}} = 1.2 W^b$$

$$\frac{D_a}{V_a^{1/3}} = 0.5 W^c$$

From Figures 2-76b and 2-76c the values of the yield transition exponents, b and c , at a scaled DOB of 1.09 m/kt^a ($HOB = -1.09 \text{ m/kt}^a$) are:

$$b = 0.023,$$

$$c = 0.033.$$

Answer: The dimensions of the crater for a 30 kt explosion at a DOB of 3 meters are:

$$\frac{R_a}{V_a^{1/3}} = 1.2 W^{0.023} = 1.2 (30)^{0.023} = 1.30,$$

$$R_a = 1.30 (4.65 \times 10^5)^{1/3} = 101 \text{ meters},$$

and

$$\frac{D_a}{V_a^{1/3}} = 0.5 W^{-0.033} = 0.5 (30)^{-0.033} = 0.447,$$

$$D_a = 0.447 (4.65 \times 10^5)^{1/3} = 34.6 \text{ meters}.$$

Uncertainty. The ranges of uncertainty for the radius and the depth are

$$1.1 W^{0.023} \leq \frac{R_a}{V_a^{1/3}} \leq 1.4 W^{0.023}$$

$$92 \leq R_a \leq 117 \text{ meters},$$

and

$$0.35 W^{-0.033} \leq \frac{D_a}{V_a^{1/3}} \leq 0.7 W^{-0.033}$$

$$24 \leq D_a \leq 49 \text{ meters}.$$

Related Material: See paragraphs 2-46 through 2-50; see also paragraphs 1-14 and 1-33.

*This could be written $DOB_1 = \frac{DOB}{W^a} = \frac{3}{(30)^{0.299}} = 1.09 \text{ m/kt}^a$, i.e., $HOB = -1.09$ is equivalent to $DOB = 1.09$.

[REDACTED]

Problem 2-24. Crater Dimensions for a Low Yield Near-Surface Explosion

Figures 2-74a through 2-75e include curves that indicate the apparent crater volume as a function of HOB for 1 kt explosion in various homogeneous media.

Scaling. For yields other than 1 kt, the crater volume scales as follows

$$\frac{V_a}{V_{a1}} = W^{3a},$$

where V_{a1} is the apparent crater volume for a 1 kt explosion, and V_a is the corresponding volume for a yield of W kt. The height of burst scales as

$$\frac{HOB}{HOB_1} = W^a.$$

Example:

Given: A hypothetical 3 kt burst over wet soil at a height of burst of 1 meter.

Find: The apparent crater radius and depth.

Solution: From paragraph 2-49,

$$HOB_1 = \frac{HOB}{W^a} = \frac{1.0}{(3)^{1/3}} = 0.693 \text{ m/kt}^{1/3}.$$

The apparent crater volume for a 3 kt burst will be determined by interpolating between the best estimate values from Figures 2-74b and 2-75b.

$$V_a(3) = 0.6 V_a(W \leq 1) + 0.4 V_a(W > 10).$$

From Figure 2-74b, the apparent crater volume for a 1-kt explosion (for $W \leq 1$), at a scaled HOB = 0.693 m/kt^{1/3}, in wet soil is

$$V_{a1} = 7.00 \times 10^3 \text{ m}^3/\text{kt}^{3a},$$

and

$$V_a(W \leq 1) = V_{a1}(W)^{3a} = 7.00 \times 10^3 (3)^{1.0} = 2.10 \times 10^4 \text{ m}^3.$$

From Figure 2-75b, the apparent crater volume for a 1 kt explosion ($W > 10$), at a scaled HOB = 0.693 m/kt^{1/3}, in wet soil is

$$V_{a1} = 1.80 \times 10^3 \text{ m}^3/\text{kt}^{3a},$$

and

$$V_a(W > 10) = V_{a1}(W)^{3a} = 1.80 \times 10^3 (3)^{1.0} = 5.40 \times 10^3 \text{ m}^3.$$

Therefore, for a 3 kt burst

$$V_a = 0.6 (2.10 \times 10^4) + 0.4 (5.40 \times 10^3) = 1.48 \times 10^4 \text{ m}^3.$$

Answer: The apparent crater dimensions for a 3 kt explosion with HOB of 1 meter are:

$$\frac{R_a}{V_a^{1/3}} = 1.2 W^{0.08} = 1.2 (3)^{0.08} = 1.31,$$

$$R_a = 1.31 (V_a)^{1/3} = 32.2 \text{ meters},$$

and

$$\frac{D_a}{V_a^{1/3}} = 0.5 W^{-0.12} = 0.5 (3)^{-0.12} = 0.438,$$

$$D_a = 0.438 (V_a)^{1/3} = 10.8 \text{ meters}.$$

Uncertainty. The dimensions of the apparent crater obtained for the above problem have a range of uncertainty that is defined by the following:

$$1.1 W^{0.08} < \frac{R_a}{V_a^{1/3}} < 1.4 W^{0.08}$$

$$29 < R_a < 38 \text{ meters}$$

and

$$0.35 W^{-0.12} < \frac{D_a}{V_a^{1/3}} < 0.7 W^{-0.12}$$

$$8 < D_a < 15 \text{ meters}.$$

If the 3 kt weapon in the preceding example were known to have a high radiative output, similar to weapons of larger yield (10 kt), then the best estimate for the apparent crater volume would be found using only Figure 2-75b. Therefore, V_a would be given by

$$V_a = 5.40 \times 10^3 \text{ m}^3,$$

and

$$R_a = 1.31 (V_a)^{1/3} = 23.0 \text{ meters},$$

$$D_a = 0.438 (V_a)^{1/3} = 7.7 \text{ meters}$$

Related Material: See paragraphs 2-46 through 2-50; see also paragraphs 1-14 and 1-33.

[REDACTED]

SUMMARY OF PROCEDURES FOR CALCULATING CRATERS FROM DEEP-BURIED BURSTS ($DOB/W^{1/3} > 5 \text{ m/kt}^{1/3}$)

Figures 2-77 through 2-81, together with appropriate scaling laws may be used to obtain crater volumes from deep-buried bursts in a variety of situations. The following summary provides a step-by-step procedure for obtaining such information. An example problem is provided immediately following the figures.

Required (either given or estimated):
 Yield (W) in kt
 Actual DOB
 Soil Type (one of the five generic types or a combination; (see Figures 2-82 and 2-86b).
 Yield-scaling parameters, α , for burst position:
 $DOB/W^{1/3} > 5 \text{ m/kt}^{1/3} \rightarrow \alpha = 1/3.4$

1. Compute DOB_1

$$(DOB \text{ for } 1 \text{ kt}) = \frac{\text{Actual DOB}}{W^\alpha}$$

2. Determine V_{a1} (apparent-crater volume for 1 kt), using curve for given soil type from Figures 2-77 to 2-81.

3. Compute V_a (actual crater volume for yield other than 1 kt):

$$V_a \text{ (actual volume)} = V_{a1} (W^{3\alpha}).$$

Three curves are provided for each soil type: best estimate, upper bound, and lower bound. Using the following guidelines, select the curve most appropriate to the problem.

- a. Use *best estimate* V_{a1} if no specific geologic data are given. If actual HE test are available for specific site, compare them with the HE curves in Figure 2-82, and move toward the upper or lower bound NE curve to adjust for these data, depending on where the data are grouped.

- b. Use *lower-bound* V_{a1} (if desirable) for target-oriented calculations (offensive-conservative) and to calculate R_a or D_a . Consider *lower-bound* V_{a1} for targeting when calculating crater-volume-related phenomena such as ejecta, transient velocity, or displacement.*

- c. Use *upper-bound* V_{a1} (if desirable) for design-oriented calculations (defense-conservative) and to calculate R_a or D_a . Consider *upper-bound* V_{a1} for design when calculating crater-related phenomena affected by volume.

4. Calculate R_a and D_a using the following expressions:

$$R_a = 1.2 V_a^{1/3}$$

$$D_a = 0.5 V_a^{1/3}$$

The dimensions R_a , D_a , and V_a can be related to other pertinent crater dimensions as follows:

- The radius to the crest of the apparent-crater lip is

$$R_{ac} = 1.25 R_a.$$

- The height of the apparent lip is

$$0.20 D_a \leq H_{ac} \leq 0.25 D_a$$

for deep-buried bursts.

Variations in the thickness of the ejecta as a function of range from the surface ground zero (SGZ) are discussed in paragraphs 2-52 and 2-53.

*In all instances it is recommended that upper and lower bound values be calculated in order to gain an appreciation of the effects of uncertainties on the particular problem under consideration.

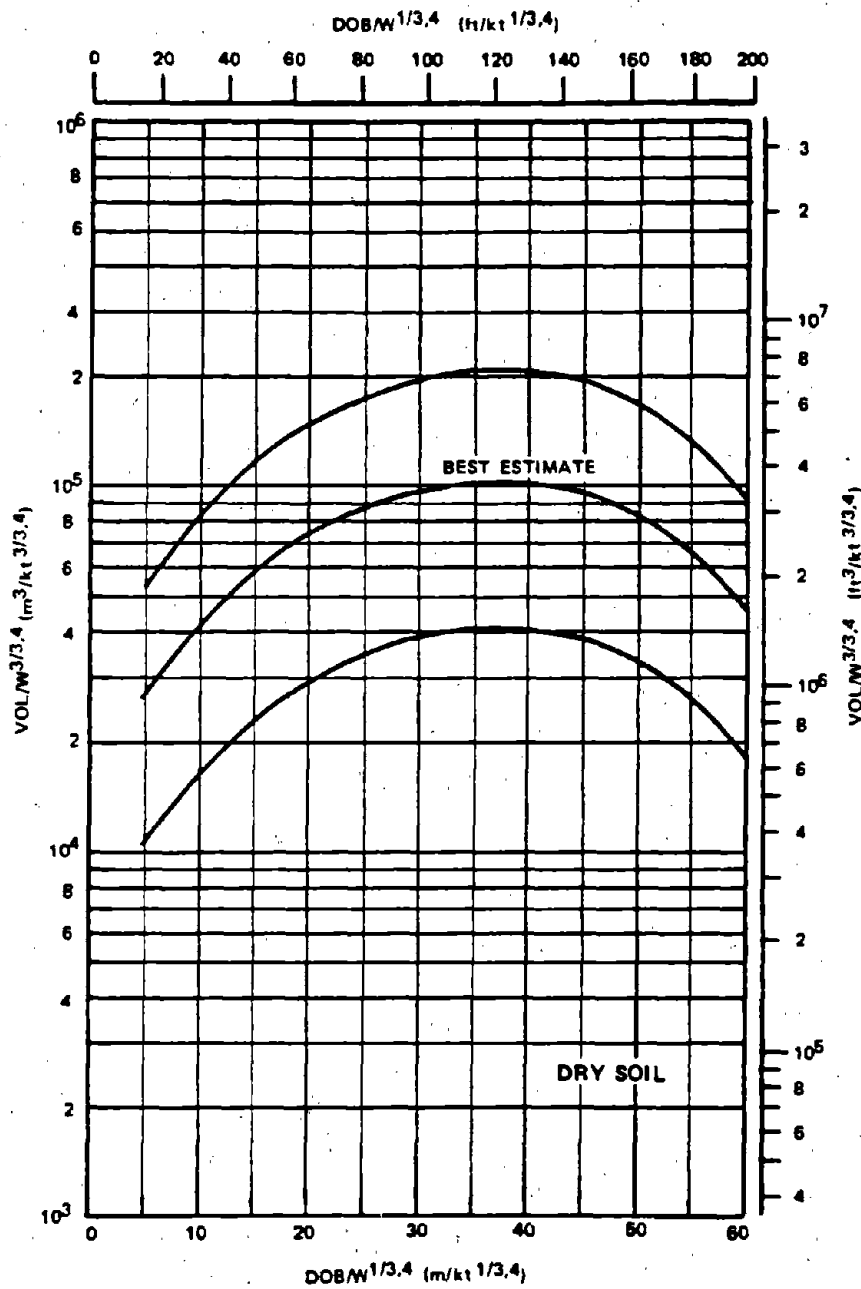


Figure 2-77. Crater Volume as a Function of Depth of Burial for a 1 Kiloton Explosion Buried in Dry Soil

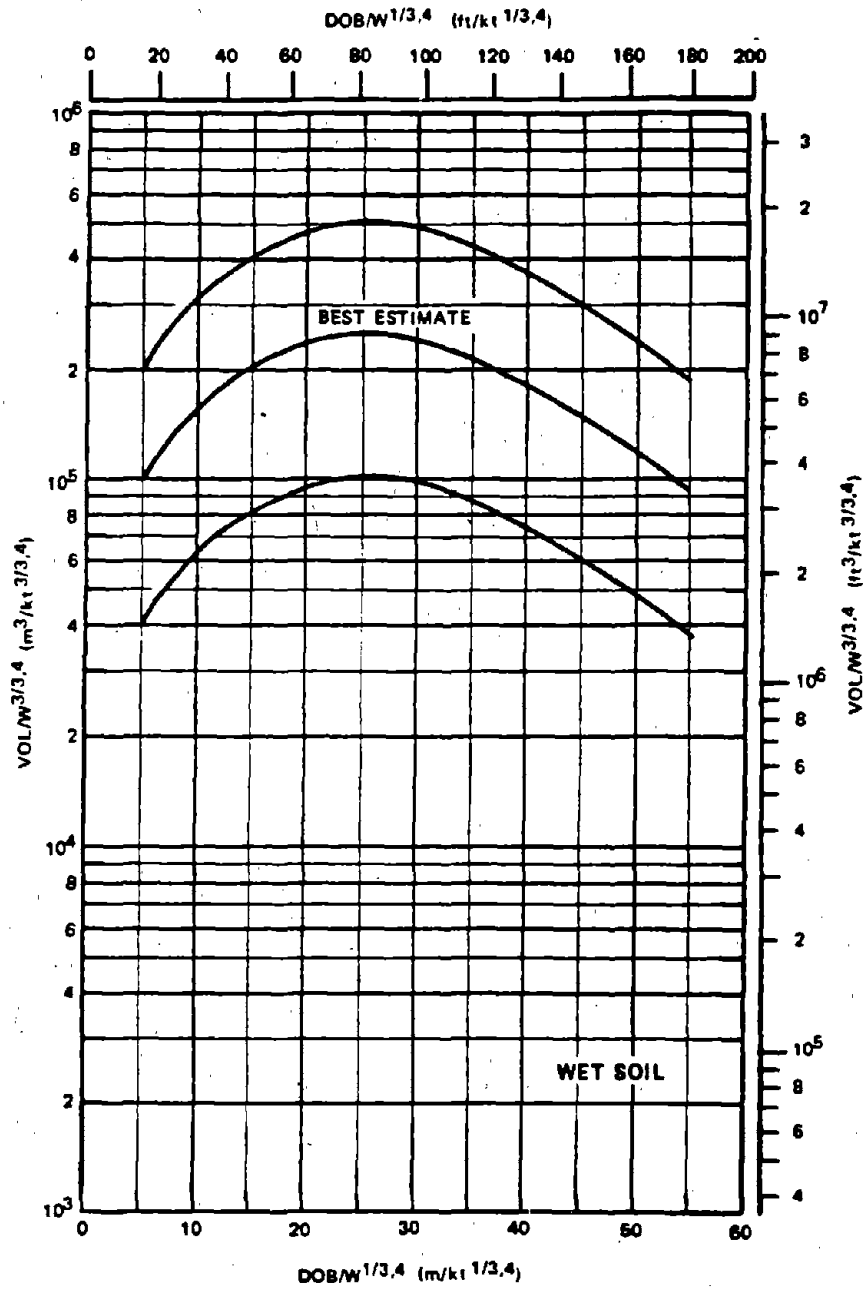


Figure 2-78. Crater Volume as a Function of Depth of Burial for a 1 Kiloton Explosion Buried in Wet Soil

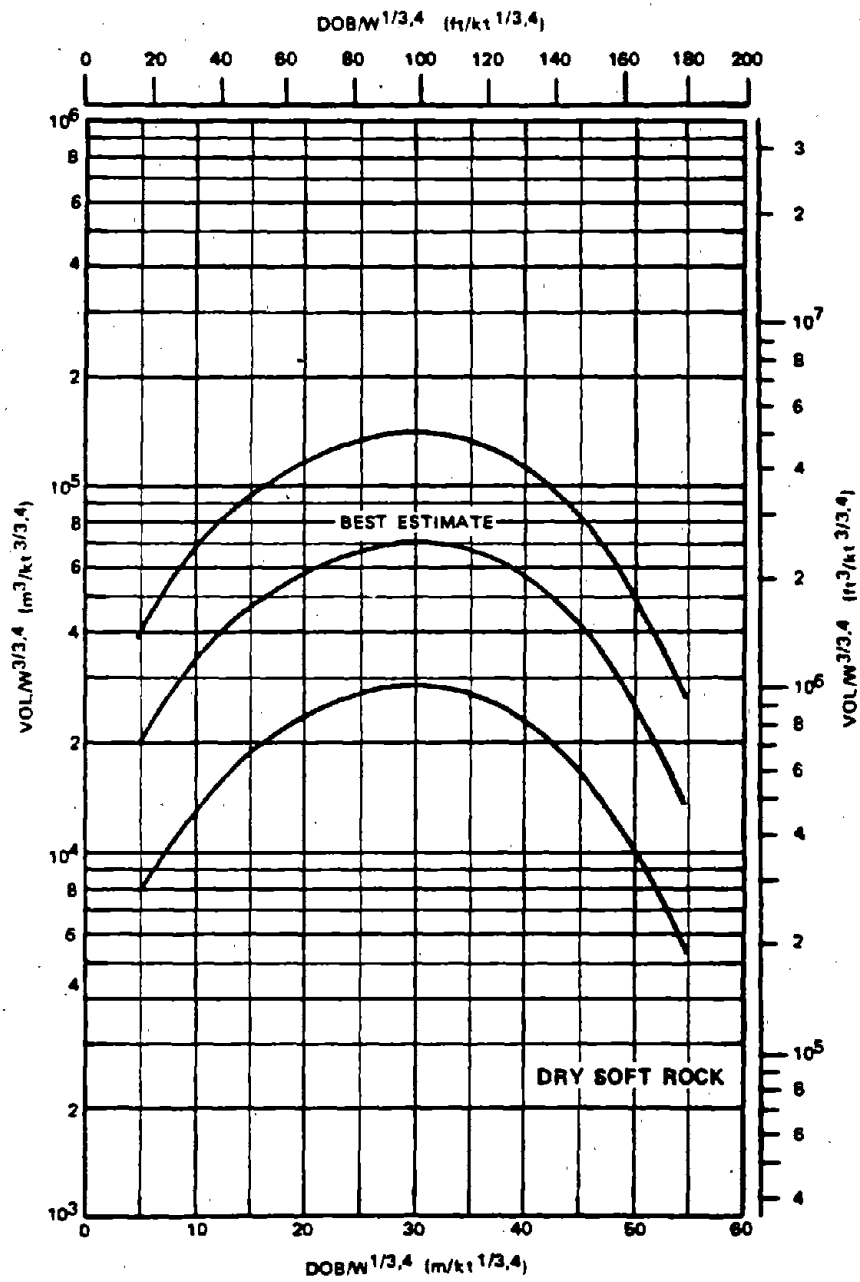


Figure 2-79. Crater Volume as a Function of Depth of Burial for a 1 Kiloton Explosion Buried in Dry Soft Rock

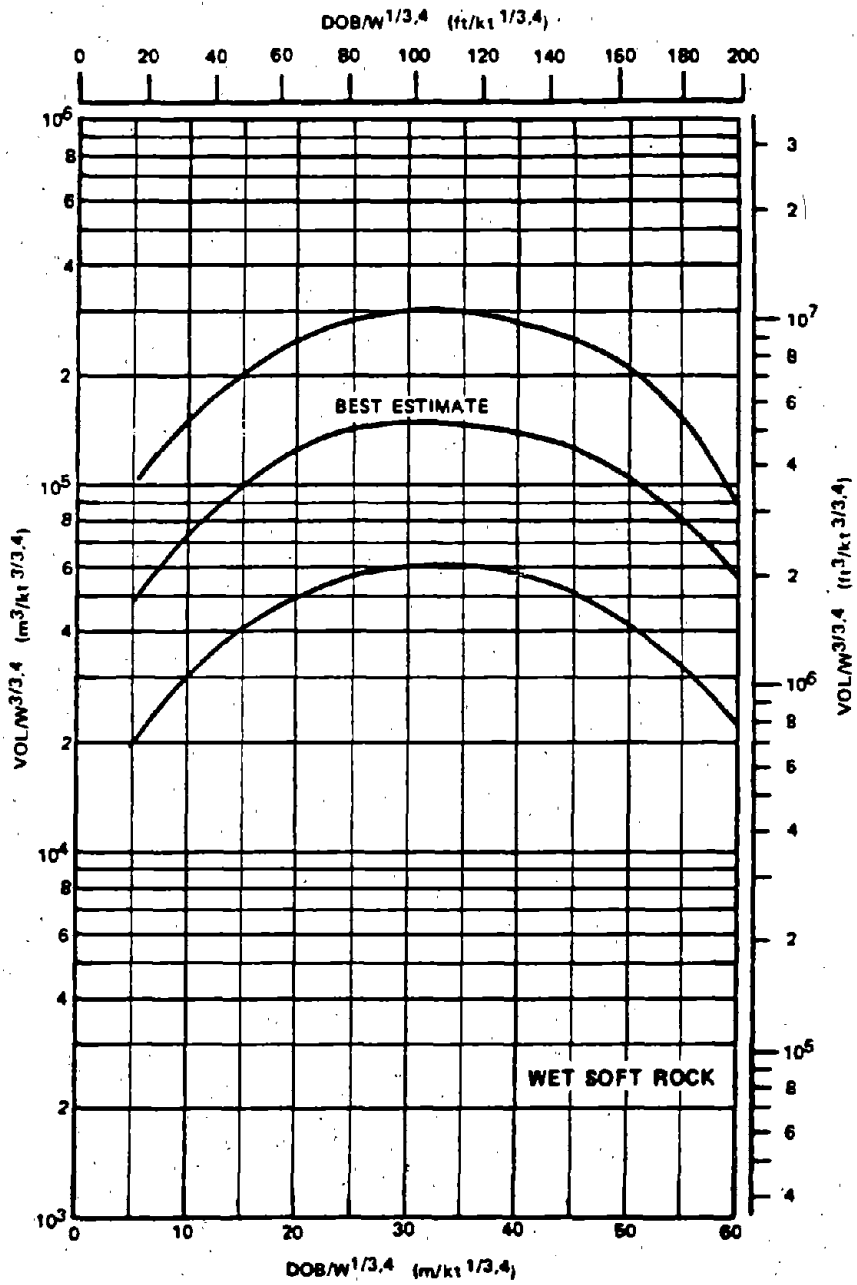


Figure 2-80. Crater Volume as a Function of Depth of Burial for a 1 Kiloton Explosion Buried in Wet Soft Rock

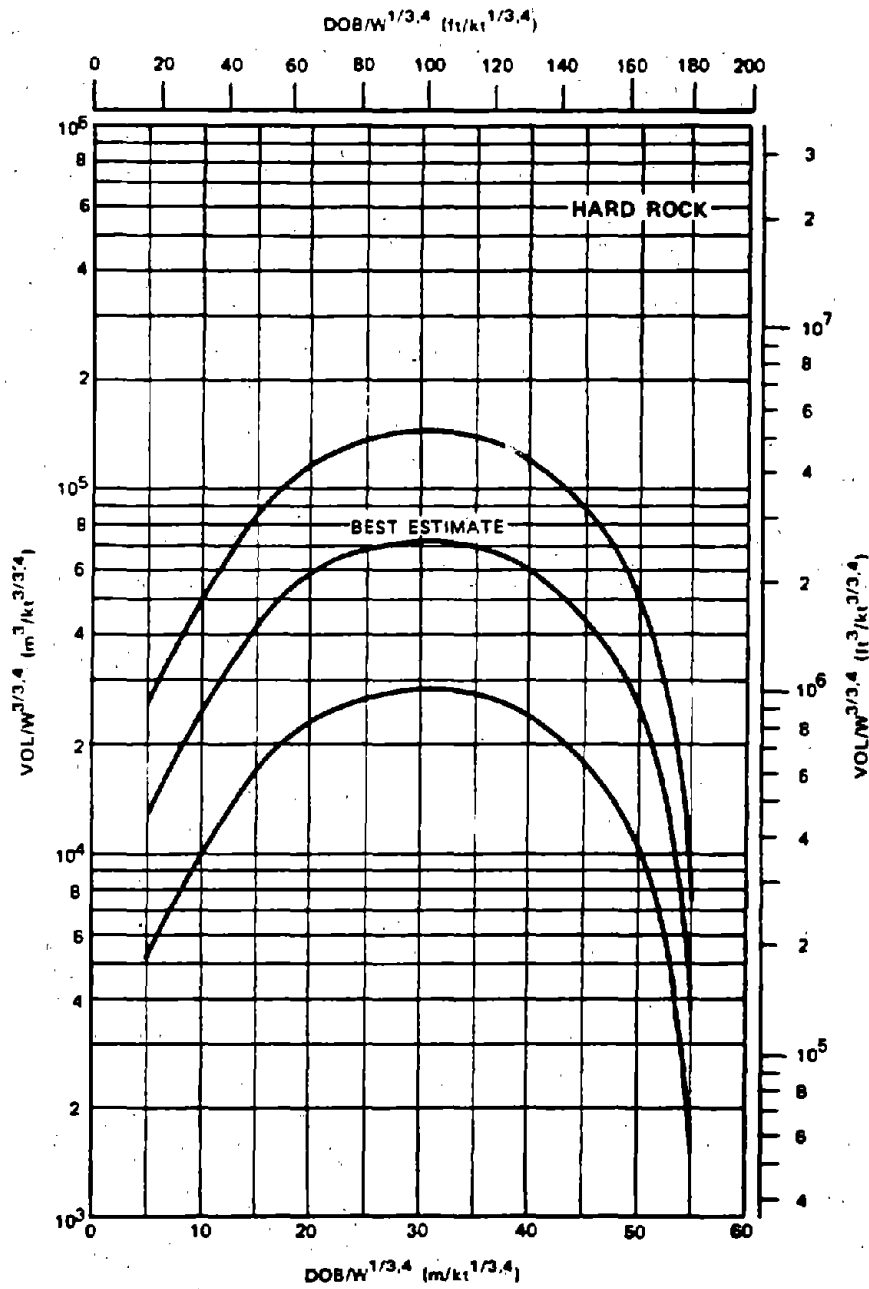


Figure 2-81. Crater Volume as a Function of Depth of Burial for a 1 Kiloton Explosion Buried in Hard Rock

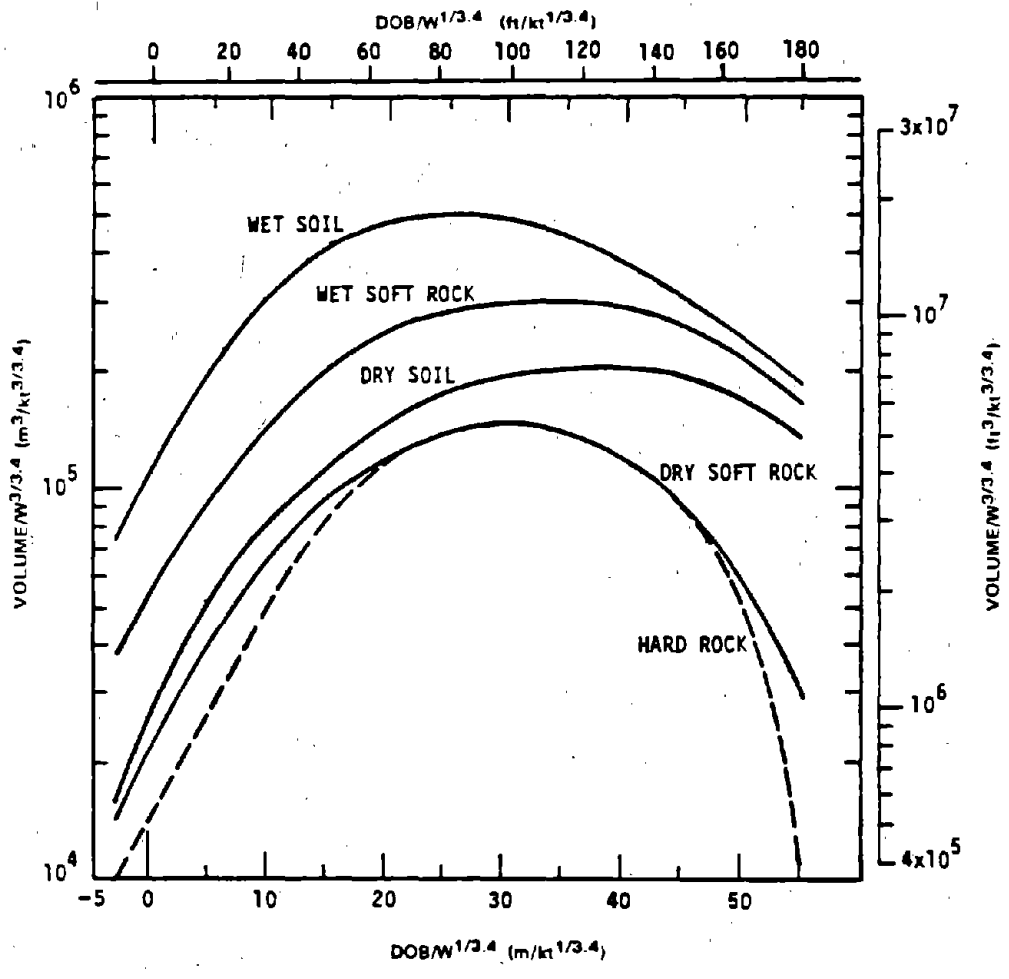


Figure 2-82. Crater Volume as a Function of Depth of Burst for HE Explosions in Five Homogenous Geologies



(This page is intentionally blank)



[REDACTED]

Problem 2-25. Calculation of Depth of Burial for Optimum Crater

Figures 2-77 through 2-81 show curves that indicate the apparent crater volume as a function of DOB for a 1 kt explosion in various media which are indicated in each figure.

Scaling. For yields other than 1 kt the crater volume and depth of burial scale as

$$\frac{DOB}{DOB_1} = W^{1/3.4},$$
$$\frac{V_a}{V_{a1}} = W^{3/3.4},$$

where DOB_1 and V_{a1} are the depth of burst and apparent crater volume for a 1 kt explosion, and DOB and V_a are the corresponding quantities for a yield of W kt.

Example:

Given: A hypothetical 3 kt explosion in hard rock.

Find: The depth of burst at which the maximum apparent crater will occur, and the dimensions of the apparent crater at this depth of burst.

Solution: From Figure 2-81, the maximum crater volume from a 1 kt explosion in hard rock occurs at a DOB_1 of 30.5 meters (note that the curve is flat in this region, and a variation of a few meters in DOB will have a small effect on V). The apparent volume of the crater from such a burst is

$$V_1 = 7.20 \times 10^4 \text{ m}^3.$$

Answer: The corresponding depth of burst and crater volume for a 3 kt explosion are

$$DOB = (DOB_1) (W)^{1/3.4} = 30.5 (3)^{1/3.4}$$
$$= 42.1 \text{ meters,}$$

$$V_a = (V_{a1}) (W)^{3/3.4} = 7.20 \times 10^4 (3)^{3/3.4}$$
$$= 1.90 \times 10^5 \text{ m}^3.$$

The apparent crater dimensions are defined by the expressions

$$R_a = 1.2 V_a^{1/3} = 1.2 (1.90 \times 10^5)^{1/3}$$
$$= 69.0 \text{ meters,}$$

$$D_a = 0.5 V_a^{1/3} = 0.5 (1.90 \times 10^5)^{1/3}$$
$$= 28.7 \text{ meters.}$$

Uncertainty: The dimensions of the apparent crater have a range of uncertainty that is defined by the expressions

$$1.1 V_a^{1/3} \leq R_a \leq 1.4 V_a^{1/3},$$

$$63 \leq R_a \leq 80 \text{ meters,}$$

$$0.35 V_a^{1/3} \leq D_a \leq 0.70 V_a^{1/3},$$

$$20 \leq D_a \leq 40 \text{ meters.}$$

In addition, the uncertainty in crater volume is given by

$$V_a (\text{min}) = V_{a1} (\text{min}) W^{3/3.4},$$

$$V_a (\text{min}) = 2.80 \times 10^4 (3)^{3/3.4},$$
$$= 7.38 \times 10^4 \text{ m}^3,$$

$$V_a (\text{max}) = V_{a1} (\text{max}) W^{3/3.4},$$

$$V_a (\text{max}) = 1.45 \times 10^5 (3)^{3/3.4},$$
$$= 3.82 \times 10^5 \text{ m}^3.$$

Related Material: See paragraph 2-51; see also paragraph 1-14 and 1-33.

EJECTA

Crater ejecta consists of soil or rock debris that is thrown beyond the boundaries of the apparent crater by an explosion. Together with the fallback, which lies between the true and apparent crater boundaries, ejecta comprises all material that is completely dissociated from the parent medium by the explosion. The ejecta field is divided into two zones:

- The crater lip, including the continuous ejecta surrounding the apparent crater.
- The discontinuous ejecta, comprised of the discrete natural missiles that fall beyond the limit of continuous ejecta.

The principal parameters used to describe the ejecta are:

- The average lip crest height.
- The radius to the crest of the crater lip from surface ground zero (SGZ).
- The depth of deposition.
- The ejecta mass density.
- The missile size distribution, which is a function of the azimuthal and radial distance from SGZ, the radius to the outer boundary of continuous ejecta, and the maximum missile range.

The principal variables that control the ejecta parameters are the yield and geometry, and the physical characteristics of the earth medium. Figure 2-83a shows the throwout of ejecta from the SEDAN Event, a 100 kt explosion at a depth of 635 feet.

2-52 Ejecta Thickness

The amount and linear extent of the continuously deposited ejecta in the crater lip are determined primarily by the yield. The radial limit of continuous ejecta, which is the outer edge of the lip, will usually vary between 2 and 3 times the apparent crater radius. The lip crest height above the original surface is estimated to be one-fourth

of the apparent crater depth ($H_{ar} = 0.25 D_a$, paragraphs 2-50 and 2-51). The depth of ejecta decreases rapidly in an exponential fashion as the distance from SGZ increases. About 80 to 90 percent of the entire ejecta volume generally is deposited within the area of continuous ejecta. Analysis of data for craters formed by near-surface bursts over soil indicates that ejecta mass represents approximately 55 percent of the apparent crater mass (the remainder being found in fallback, compaction, and the dust cloud, which is blown away). When the same yields explode at successively greater depths, ejecta mass increases significantly until the optimum DOB is reached. Ejecta thickness can be estimated for soil as follows (all dimensions are in feet):

$$t_e = 0.9V_a^{1.6} R^{-3.86}, \text{ for } R > 2.2V_a^{1/3}$$

where t_e is the ejecta thickness, V_a is the apparent crater volume, and R is the distance from SGZ to the point of interest. This formula for ejecta thickness assumes that the ejecta mass density will be approximately equal to the original in-situ density of the medium. The equation may be considered valid for a soil medium; however, the bulking, which is inherent in a disturbed rock medium would result in greater ejecta thicknesses than predicted by the formula. Therefore, in a rock medium, the ejecta thickness should be increased by 30 percent to account for the bulking, i.e., the formula for a rock medium is

$$t_e = 1.17V_a^{1.6} R^{-3.86}, \text{ for } R > 2.2V_a^{1/3}$$

2-53 Maximum Missile Range

Figure 2-83b shows the maximum missile range as a function of depth of burst for a 1 kt explosion in two soil types. These data are based on empirical results from several nuclear explosions.

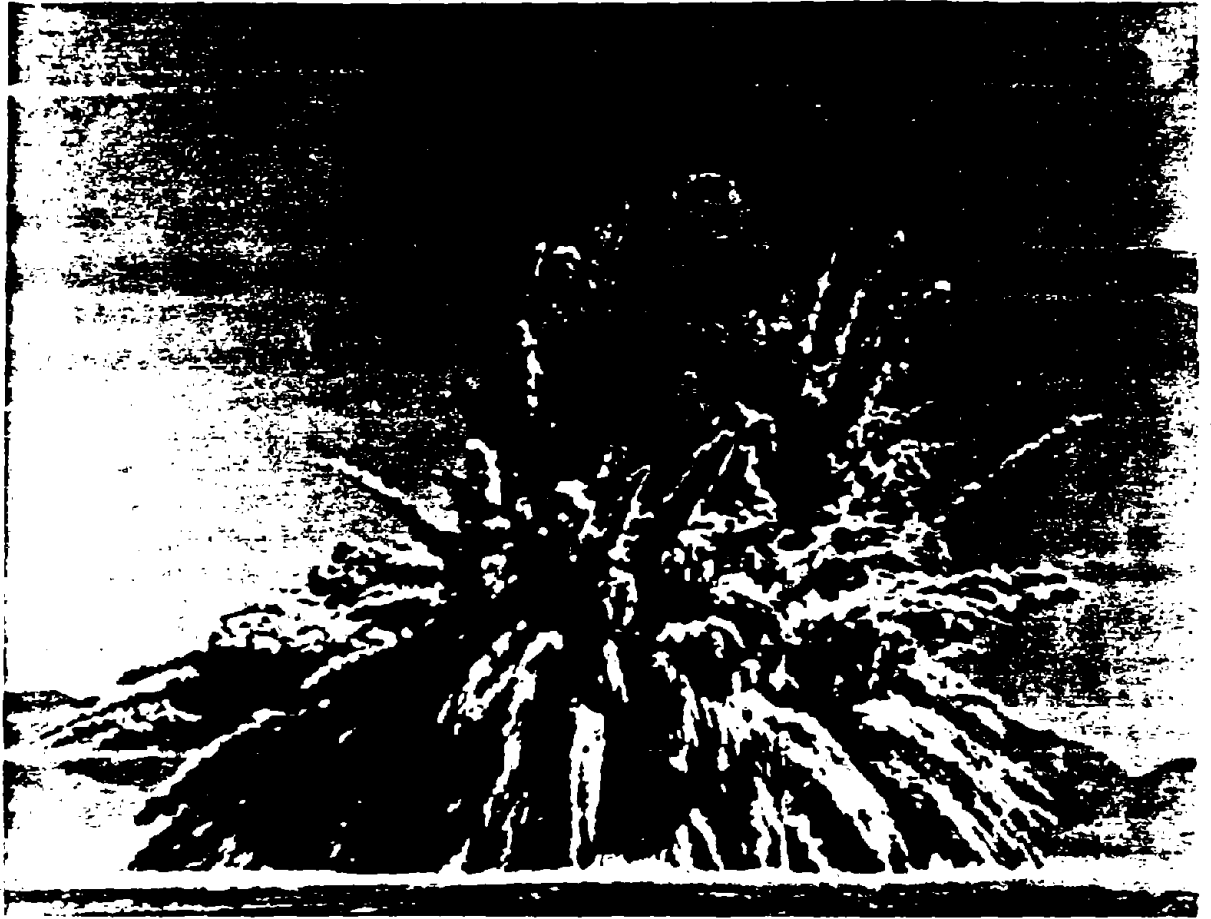


Figure 2-83a. Throwout of Ejecta from the 100-kt SEDAN Event



[REDACTED]

Problem 2-26a. Calculation of Ejecta Thickness

Paragraph 2-52 provides formulas for the prediction of ejecta thickness as a function of distance from surface ground zero and the apparent crater volume (V_a). V_a may be obtained from Figures 2-74a through 2-76c for near surface bursts and 2-77 through 2-81 for deep-buried bursts by the methods described in paragraphs 2-49 through 2-51.

Example:

Given: A hypothetical 300 kt contact surface burst (center of gravity of the weapon 0.5 meters above the surface) will produce a crater predicted to have an apparent radius of 137 meters, an apparent depth of 18.2 meters and an apparent volume of 3.75×10^5 cubic meters in dry soil. (See problem 2-22).

Find: The thickness of the ejecta at a distance of 300 meters from SGZ.

Solution:

$$R = 300 \text{ meters,}$$

$$2.2V_a^{1/3} = 2.2(3.75 \times 10^5)^{1/3} = 159 \text{ meters}$$

$$R > 2.2V_a^{1/3}$$

Therefore the equation for soil given in paragraph 2-52 applies.

Answer: The ejecta thickness is

$$r_e = 0.9V_a^{1.6} R^{-3.86}$$

$$r_e = 0.9 (3.75 \times 10^5)^{1.6} (300)^{-3.86} =$$

$$0.20 \text{ meters}$$

Reliability: Based on empirical formulas derived from high explosive and nuclear burst. Specific reliability has not been estimated.

Related Material: See paragraph 2-49 through 2-52. See also Problem 2-22.

[REDACTED]

Problem 2-26b. Calculation of Maximum Missile Range

Figure 2-83b shows the maximum range to which missiles might be expected from a 1 kt explosion as a function of depth of burial in two soil types.

Scaling. For yields other than 1 kt, the maximum missile range and depth of burst scale as follows:

$$\frac{R_m}{R_{m1}} = \frac{DOB}{DOB_1} = W^{0.3}$$

where R_{m1} is the maximum missile range for 1 kt, DOB_1 is the depth of burst for 1 kt, and R_m and DOB are the corresponding range and burial depth for W kt.

Example:

Given: A hypothetical 3 kt explosion at a depth of 85 meters in hard rock.

Find: The maximum missile range for the explosion.

Solution: The corresponding depth of burst for a 1 kt explosion is

$$DOB_1 = \frac{DOB}{W^{0.3}} = \frac{85}{(3)^{0.3}} = 61 \text{ meters.}$$

From Figure 2-83b, the maximum missile range for a 1 kt explosion at a depth of 61 meters in hard rock is 440 meters.

Answer: The corresponding maximum missile range for a 3 kt explosion at a depth of 85 meters in hard rock is

$$R_m = R_{m1} W^{0.3} = (440) (3)^{0.3} = 612 \text{ meters.}$$

Reliability: Based on empirical results from several nuclear explosions, but no specific reliability has been estimated.

Related Material: See paragraphs 2-46 through 2-52.

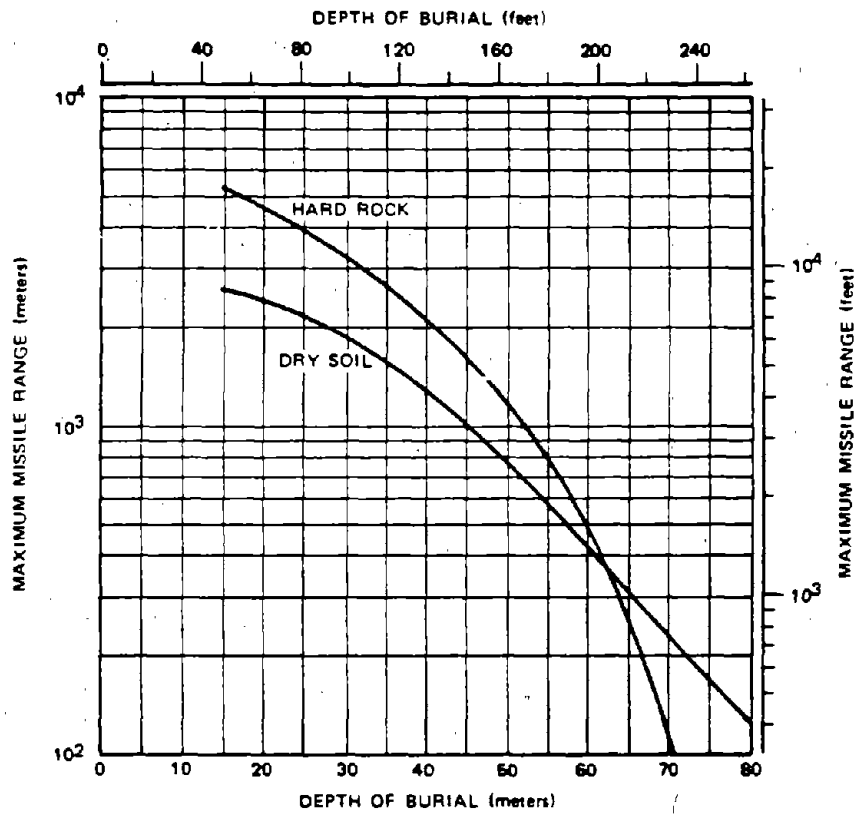


Figure 2-83b. Maximum Missile Range as a Function of Depth of Burial for a 1 kt Explosion



CHARGE STEMMING

The term charge stemming refers to the backfilling of material in the charge-emplacment hole. Ideally, charges should be completely stemmed and tamped to contain the explosive energy temporarily, which increases its coupling with the medium. Typical stemming materials are concrete, gravel, sand and water. The cratering curves shown in preceding paragraphs provide predictions for fully stemmed charges. There are, however, operational considerations that may require reduced stemming or the capability to emplace or remove the stemming material in a short period of time. Therefore, modified stemming geometries, including various degrees of stemming or no stemming at all, are important considerations in the evaluation of nuclear cratering phenomena.

The following changes in cratering phenomena generally may be expected when less than full stemming is used:

- Air blast and the fraction of radioactive materials that vents will be increased.
- Energy loss out of the emplacement hole will reduce the coupling effectiveness of the explosion. This will result in crater dimensions that are smaller than those from fully stemmed explosions.
- Energy deposited in the emplacement hole will cause a modification to the energy deposition pattern in the medium. The source will appear to be a distorted cylindrical source rather than a concentrated spherical source. Lip height, ejecta distribution, and maximum missile range will vary from those of a fully stemmed explosion.

2-54 Guidelines for Assessing the Effect of Stemming

The crater dimensions from a partially stemmed or an unstemmed emplacement hole

will be affected primarily by the amount of stemming, the diameter of the emplacement hole, and the depth of burial. The following are some general conclusions concerning stemming that are based largely on HE experiments.

- The crater radius, which is the dimension of greatest military importance, does not increase significantly with increased stemming.
- Stemming about one-half of the emplacement hole (50% stemming) provides most of the crater depth that would be expected from a fully stemmed charge.
- Water appears to be a very efficient stemming material.

Figures 2-84a, b, and c illustrate the HE experimental results concerning the effect of stemming on crater volume, diameter, and depth, respectively.

EFFECTS OF GEOLOGICAL FACTORS

In most situations a weapon will *not* be burst in a homogeneous medium such as dry soil or wet soft rock. Instead, typical geologies may contain a water table at a shallow depth, a layering of one type of media over another (e.g., soil over rock), parallel planes of distant jointing in rock, or a steeply sloping ground surface. All of these factors can influence the formation of a crater and, in some cases, can change the size or characteristics of the crater significantly. The following paragraphs describe the general effects of geologic variations on cratering phenomena.

2-55 Sloping Topography

Terrain slopes of about five degrees or more will affect the geometry of a crater formed by either a surface or buried explosion. The ejecta distribution will also be affected. If the slope is gentle, the crater volume will be comparable

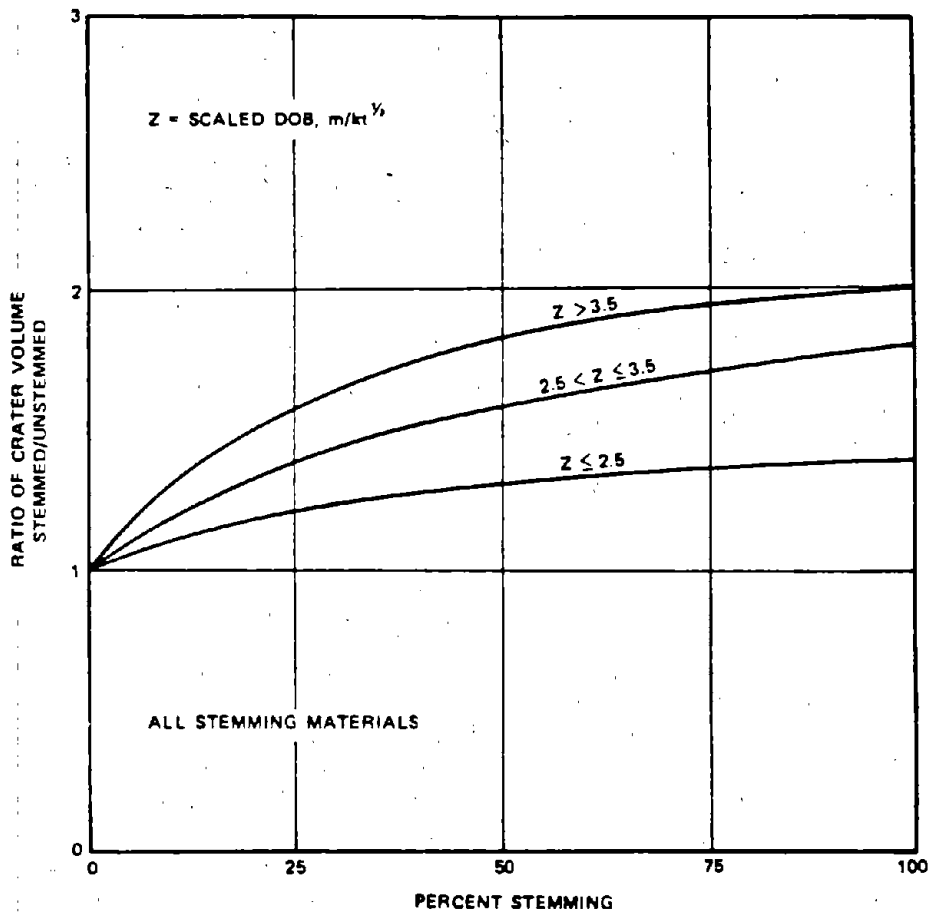


Figure 2-84a. Increase in HE Crater Volume as a Function of Stemming for Various DOBs

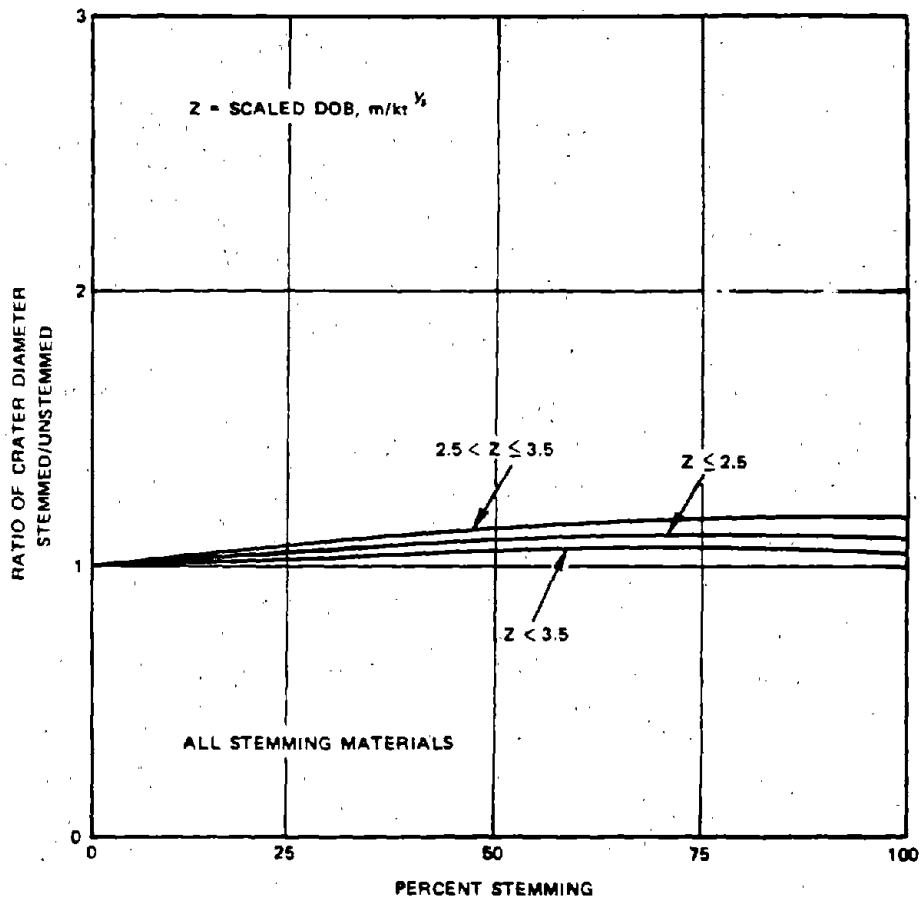


Figure 2-84b. Increase in HE Crater Diameter as a function of Stemming for Various DOBs

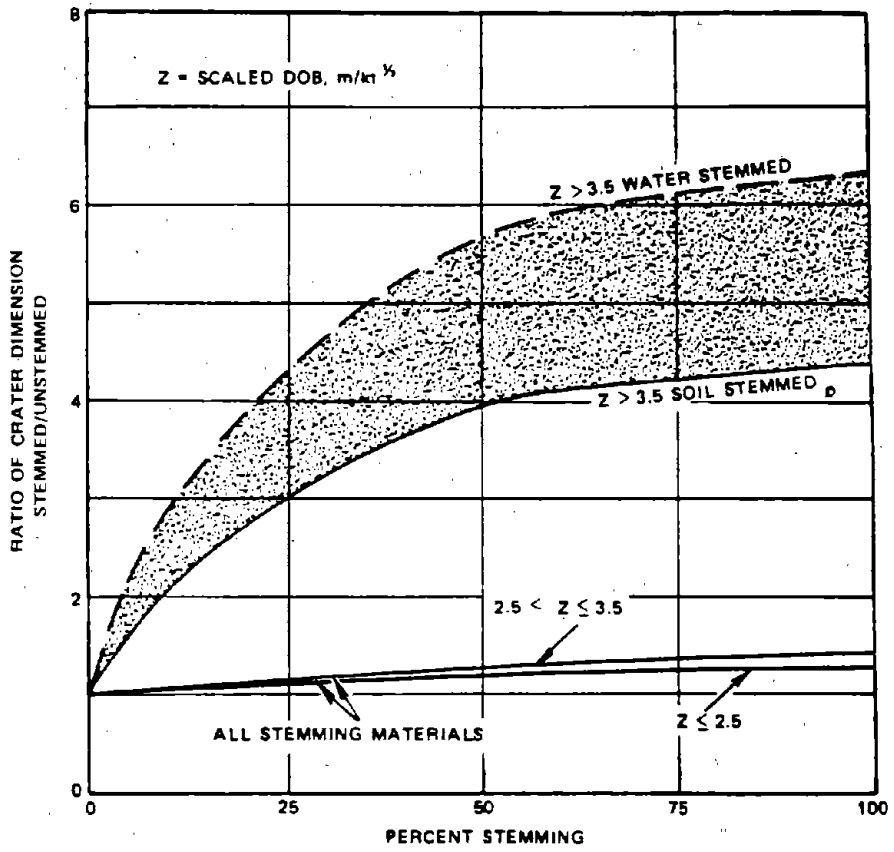


Figure 2-84c. Increase in HE Crater Depth as a Function of Stemming for Various DOBs

[REDACTED]

with that of craters on level ground, but the resulting crater will be asymmetrical; it will be wider up-slope and will have a larger lip down-slope. Figures 2-85a and b show a photograph and a schematic drawing, respectively, of the crater from a nuclear event buried 30 meters below a 30 degree slope in tuff. The shape of the crater formed by this explosion was influenced by the slope of the surface because almost all the debris formed a rock slide originating at the lower edge of the crater and terminating about 240 meters down the slope.

Limited small-scale cratering experiments have been conducted in moist, sandy soil and in desert alluvium on slopes ranging from 40 degrees to vertical wedges. For charges buried on severe but nonvertical slopes, with DOB measured normal to the sloping surface and with the vertical depth of overburden being greater than containment depth, crater dimensions decrease with increasing slope. Optimum vertical DOB appears larger by about one-third than optimum DOB on level terrain.

2-56 Water Tables

A subsurface ground water table in a soil medium will begin to influence the size and shape of the crater when its depth below the surface is equal to or less than three-fourths the predicted apparent crater depth. Its effect is to flatten and widen the crater. Figure 2-86a illustrates the effect of a shallow water table on the shape of the crater. As the water table depth decreases, its effect becomes more evident. Based upon HE experiments, it can be concluded that for a surface detonation, the influence of the water table is not significant for scaled water table depths greater than about $3.5 \text{ m/kt}^{1/3}$, and the apparent radius, volume and lip height increase exponentially as the water table approaches the ground surface. For shallow buried bursts ($\text{DOB}/W^{1/3} < 3 \text{ m/kt}^{1/3}$)

the final crater radius may be as much as 50 percent greater than the predicted value and the depth as little as one-third that of the predicted value.

Figure 2-86b shows a normalization technique that has been developed for plotting crater volume for surface and shallow buried explosions in a layered geology. A shallow water table effectively causes a homogeneous medium to act as a two layered medium

d = depth to water table (thickness of upper layer)

V_a = apparent crater volume

V_u = apparent crater volume predicted in the upper layer alone (usually dry soil)

V_L = apparent crater volume predicted in the lower layer alone (usually wet soil).

The curve fitted to the water table crater volume data in Figure 2-86b is given by the expression

$$\frac{V_a - V_L}{V_u - V_L} = 1 - \exp(-5.4 d/V_a^{1/3}).$$

Iteration is required to solve this expression for V_a ; however, the technique converges very rapidly. It is recommended that the curve in Figure 2-86b be used to predict crater volume for sites having a shallow water table.

2-57 Bedrock

The influence of a bedrock layer below a soil medium is similar to that of a water table, though somewhat less pronounced. For surface explosions it appears that a hard layer may limit the crater depth while causing the crater shape to be more nearly trapezoidal than parabolic or conical (see Figure 2-86c). The bedrock layer may increase the crater radius slightly (5 to 10



Figure 2-85a. NEPTUNE Crater and its Position on Slope of Mesa

2-198

Reproduced from
best available copy.



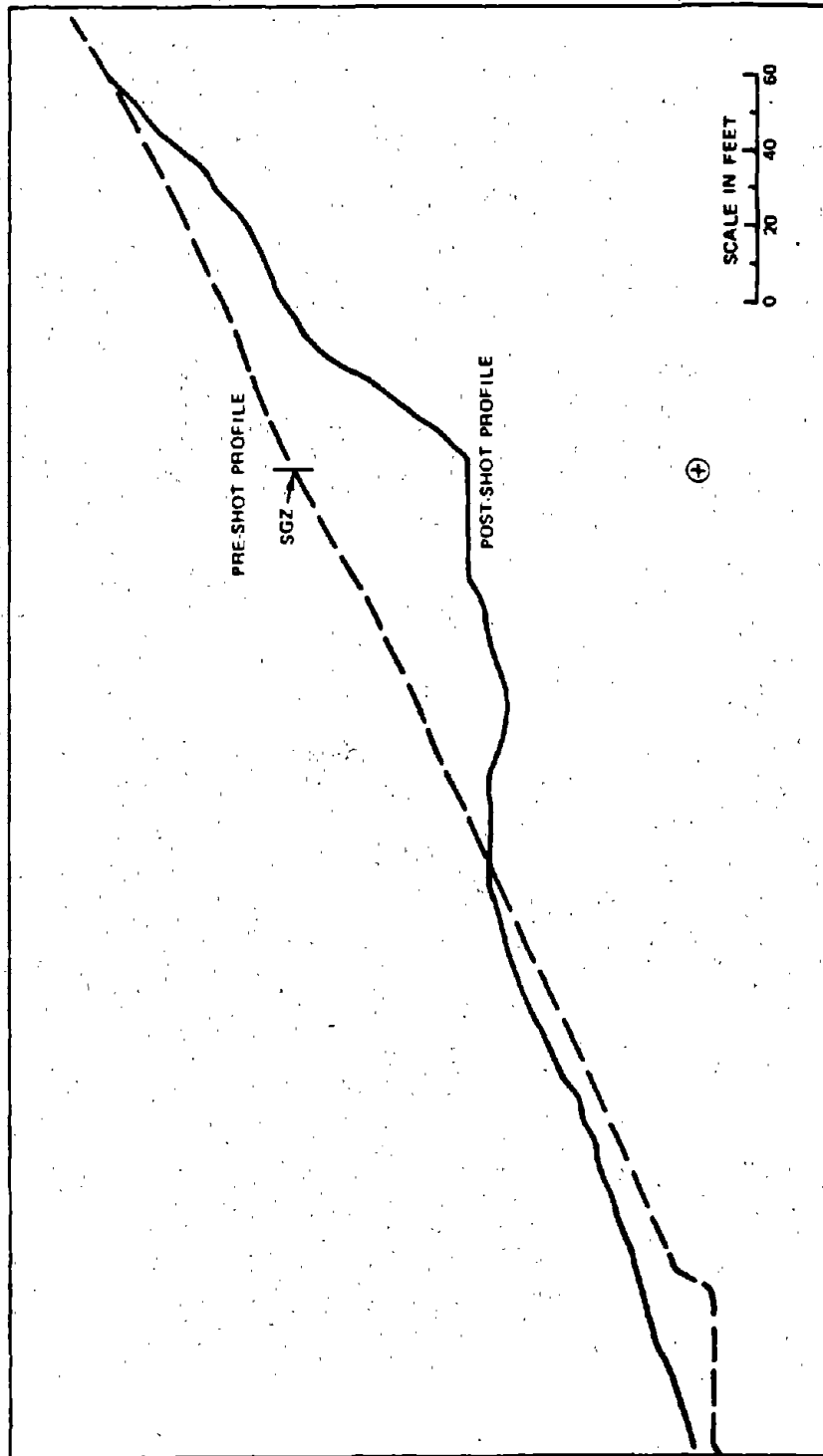


Figure 2-85b. Section of NEPTUNE Crater Normal to Slope Contours

Reproduced from
best available copy.



Figure 2-88a. Crater Formed by a Surface Detonation of a 0.5 kt High Explosive Charge in a Wet Soil Medium with a Shallow Water Table (DIAL PACK Event); a 8.2 m (27 ft.) Diameter Sphere with the Bottom Tangent to the Ground:
 $R_g = 30.48 \text{ m (100 ft.)}$; $D_g = 4.6 \text{ m (15 ft.)}$

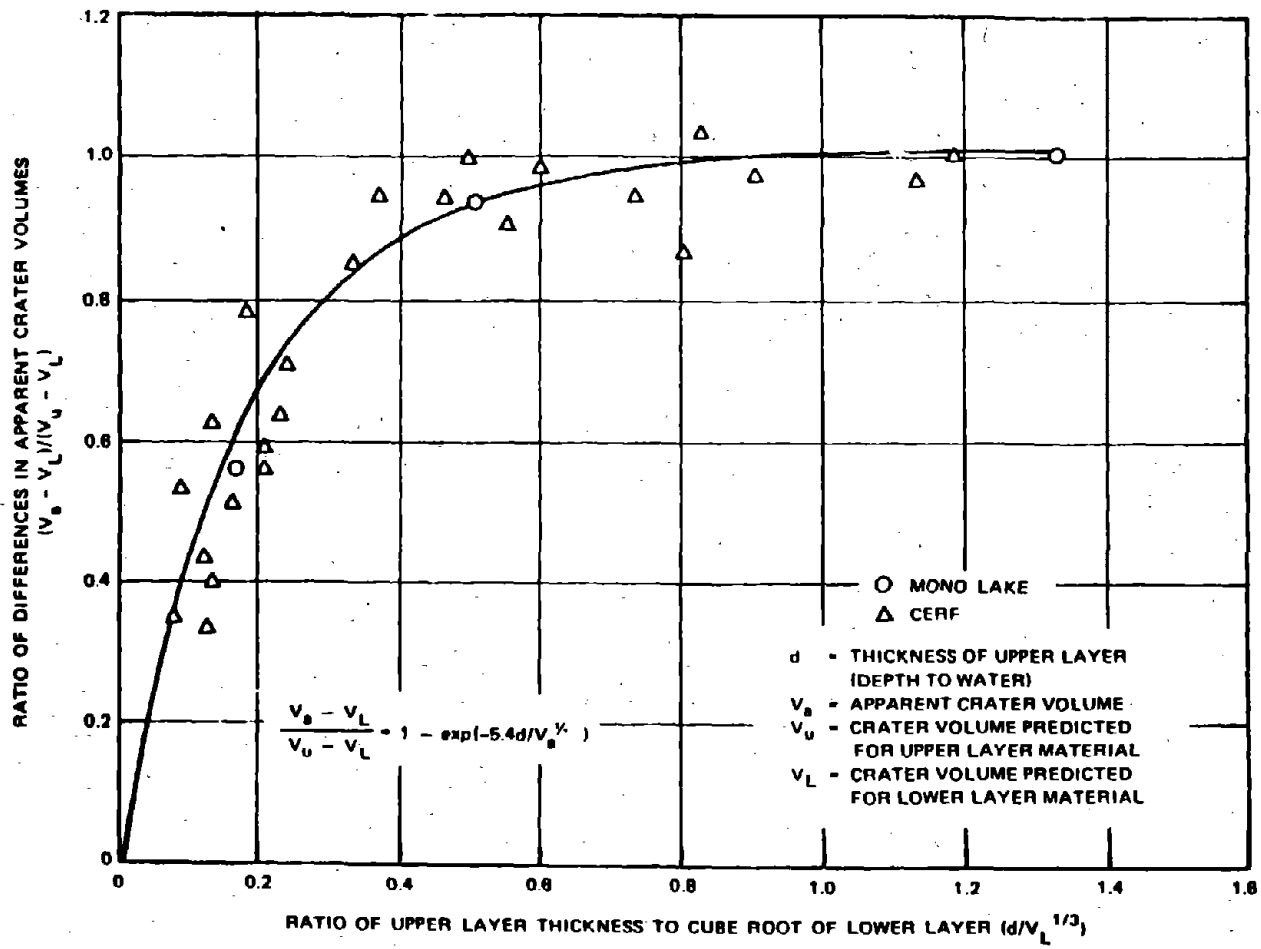


Figure 2-86b. Cratering Data for Dry Soil over Wet Soil

[REDACTED]

percent). The layer may decrease the final crater depth by as much as one-third when the overburden layer is as shallow as one-fourth the predicted apparent crater depth.

Although the effect of a water table and the effect of a hard layer are different, the water table curve is a good approximation for predicting the crater volume in a layered geology involving a gradual transition to rock. The water table curve should *not* be used for geologies involving a sharp transition to rock.

The two-layer problem can be generalized to three layers. Let V_1 , V_2 , and V_3 be the crater volume associated with the top, middle, and bottom materials considered separately. Then, V_{23} is the crater volume associated with the middle layer and bottom layer, and V is the crater volume in the total layered medium.

V_{23} is calculated by neglecting the top layer and then solving a two-layer problem with V_2 as the upper layer and V_3 as the lower layer. The thickness of the middle layer d_2 is used as the depth to the lower layer. This gives

$$\frac{V_{23} - V_3}{V_2 - V_3} = 1 - \exp(-5.4 d_2 / V_{23}^{1/3})$$

V is then calculated by solving another two-layer problem with V_1 as the upper layer and V_{23} as the lower layer. The thickness of the upper layer d_1 is used as the depth of the lower layer. This gives

$$\frac{V - V_{23}}{V_1 - V_{23}} = 1 - \exp(-5.4 d_1 / V^{1/3})$$

2-58 Rock Bedding/Jointing

If a low-yield explosion occurs at or very near the surface, the bedding or jointing planes in rock can influence the shape of the crater produced. The direction of the ejection process

will also be affected. The formation of the crater will tend to follow the direction of the predominant joints, and the crater radius will be increased by as much as one-third in the direction parallel to the joints and decreased by as much as one-third in the direction normal to the joints. The magnitude of the crater depth is usually not affected significantly, but the deepest point may be shifted to one side of the crater. As the yield or the DOB is increased, the influence of rock jointing is reduced.

The dip of bedding planes will influence energy propagation, and this will cause the maximum crater depth to be offset in the down-dip direction. Little overall effect is noted on the size of the crater radius, but differences in ejection angles cause the maximum lip height and ejecta radius to occur down-dip.

2-59 Snow and Ice

Measured craters in snow or ice are a rarity; however, data for a few craters have been recorded for surface HE explosions. In general, these craters are larger than would be predicted in soil and they are characteristically wide and flat. The trends in crater size and shape for a surface explosion in a snow/ice medium are given by the expressions

$$R_a = 38.8 W^{0.26} \text{ meters}$$

$$D_a = 5.75 W^{0.15} \text{ meters}$$

where W is the yield in kilotons.

MULTIPLE BURST GEOMETRIES

Nuclear weapons may be detonated in close proximity to each other to create a linear crater or a series of interconnected craters. When simultaneous explosions are sufficiently close to cause interactions, the shot geometry is termed "multiple burst." A linear array of this nature is referred to as a row crater, as illustrated in Figure 2-87.

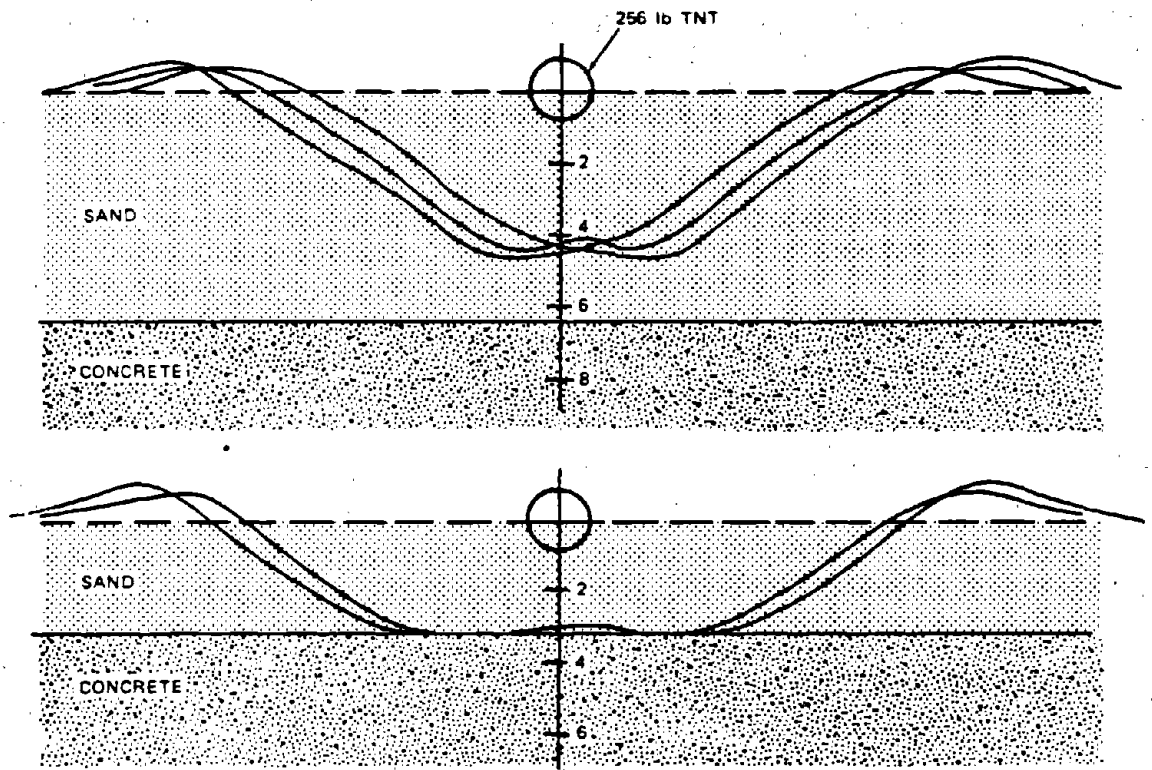


Figure 2-86c. Effects of a Hard Near-Surface Layer on Cratering



Figure 2-87. A Row Crater Produced by Simultaneous Explosions of Five 1.1 kt Nuclear Devices at Optimum DOB (BUGGY Event) in Basalt: DOB = 41 m (135 ft.); Spacing = 45.7 m (150 ft.); Width = 76.2 m (250 ft.); Depth = 19.8 m (65 ft.); Length = 262 m (860 ft.)

In addition to the parameters normally associated with an underground explosion, the results of a row charge also depend upon the spacing between charges (s) and the degree of simultaneity of the explosions. Differences of only a few milliseconds in the times of explosion of adjacent charges can result in significantly degraded row charge crater dimensions. Close spacing of weapons (less than 1.4 times a single weapon crater radius) increases both the crater radius and depth compared to single weapon craters at the same scaled DOB. Experience has shown that a spacing of $1.0 R_a$ (for explosions at optimum DOB) results in a smooth channel with crater depth and radius approximately 20 percent greater than those of single explosions. A spacing of $1.25 R_a$ will still form a smooth channel, but with less enhancement of crater dimensions, while spacing of $1.5 R_a$ will provide an adequate linear obstacle. The length of a row

crater L can be found in the equation:

$$L = s(n - 1) + 2 R_a,$$

where n is the number of charges in the row, and s is the spacing between charges.

SECTION III

GROUND SHOCK PHENOMENA

2-60 General Nature of Free-Field Effects

The position of the weapon at the time of detonation has a marked influence on the amount and nature of the energy transfer into the ground. The effects at depths below the surface from a high air burst will be primarily of the air-induced type. For surface or near surface bursts, both air-induced and direct-transmitted ground shock effects are produced, and both may be of importance. Deep underground bursts cause direct-transmitted effects almost exclusively.

The nuclear field tests of the past several decades involving air, surface, and fully contained bursts have provided the data that permit development of the expressions for predicting the peak values of air-induced and direct-transmitted acceleration, velocity, and displacement. Field observations for regions where the air blast overpressures are less than 1,000 psi generally indicate that, within about 50 to 100 feet of the surface, ground motions are predominantly air-induced. The relatively few measurements of acceleration and displacement that have been made at significant distances below the ground surface show the effects of attenuation and dispersion as the air-induced pulse travels through the ground.

A typical acceleration-time record from a gage mounted near the surface of the ground



exhibits a systematic pulse shape corresponding to the passage of the shock wave, with a random type disturbance often superimposed on this systematic pulse. In the superseismic case, when the air blast propagation velocity is greater than the ground seismic velocity, the downward acceleration is large compared with the following upward acceleration. The velocity-time record is similar in shape to the overpressure-time pulse, at least in the early stages. In cases in which the ground motion outruns the air blast, there is a slower rise in the acceleration; it may even be reversed in direction initially, i.e., upward rather than downward. In such cases, the signals may last for a longer time than the positive phase overpressure duration. The associated velocity wave form usually exhibits a velocity jump as the air-shock wave passes over the position, but the overall record is characterized by a considerable degree of oscillation. When precursors are present, the acceleration and velocity records may exhibit higher frequency components and more random type of oscillation. Wave front dia-

grams for the superseismic and outrunning cases are shown in Figure 2-88.

Most values of velocity have been obtained by integrating acceleration records. In general, velocities appear to be more predictable quantities than accelerations or displacements. Displacement data are even scarcer than velocity data, and only a few direct measurements have been made. For the most part, displacement data consist of integrated acceleration records or extrapolation of displacement spectra to zero frequency.

Knowledge of direct-transmitted ground shock effects is limited. Those data that exist were obtained from buried high explosive shots, from several surface and near surface nuclear detonations, and from a number of fully contained bursts. For a completely buried shot, measurements indicate that at any particular range R , the strain or velocity pulse rises in a parabolic manner to a peak value in a time roughly corresponding to $T_r = R/6c_p$ to $R/12c_p$, where R is the range from the explosion, and c_p

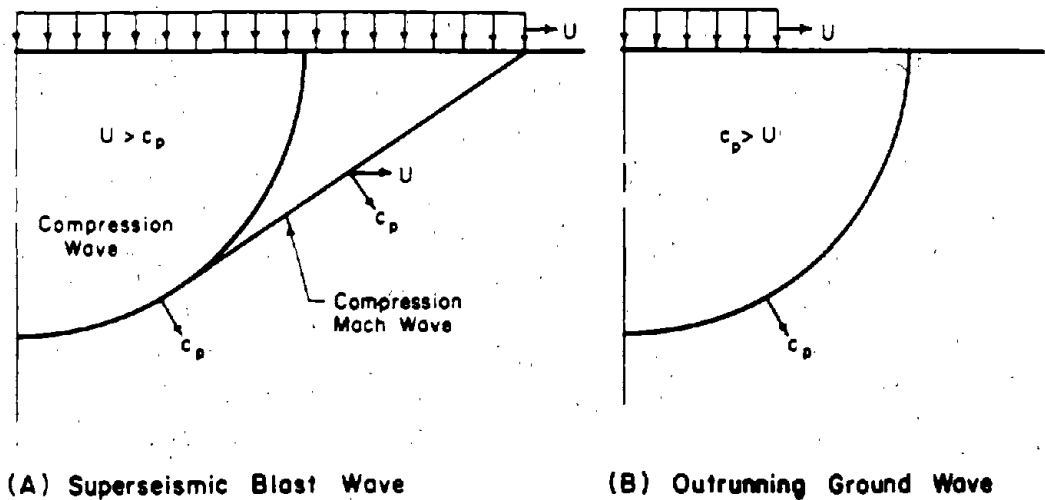


Figure 2-88. Wave Front Diagram for Superseismic Air Blast and Outrunning Ground Wave

2-112
205

is the effective seismic velocity of the medium. The signal then drops slowly with a total positive phase duration corresponding approximately to $T_o = R/2c_p$ to R/c_p . The effects of layering, reflection, and refraction, tend to introduce high frequency and random components of motion.

2-61 Types of Effects

It is convenient to consider the earth shock resulting from a nuclear explosion as producing both systematic and random effects. Systematic effects can be divided further into two major types:

- Air-induced shock associated with the passage of an air shock wave over the surface of the ground, and the overpressure at the surface above the structure transmitted downward with such attenuation and dispersion as may be consistent with the physical conditions at the site.
- Direct-transmitted ground shock that arises from direct energy transfer from surface, near surface, or underground bursts.

Random effects include high frequency ground-transmitted shock, surface-wave effects, reflections, refractions, etc. The dominant effect depends on such factors as weapon yield, point of detonation with respect to the ground surface, range from ground zero, depth of the measurement, and, in particular, the geologic conditions.

Reasonable estimates can be made of the maximum values of displacement, velocity, and acceleration associated with the air-induced shock and in more restricted cases for the direct-transmitted ground shock under more or less uniform geologic conditions.

2-62 Air-Induced Effects

At the surface in a homogeneous medium the maximum transient elastic vertical displacement may be expressed as

2-178.206

$$d_w = \frac{Hp_{so}}{2E}$$

where H is the depth to which the air-induced shock wave extends during the effective duration of the shock, t_i , p_{so} is the side-on overpressure at the surface, and E is the restrained modulus. The duration of the shock may be approximated by

$$t_i \approx 0.37 \left(\frac{100}{p_{so}} \right)^{1/2} (W(Mt))^{1/3}$$

for

$$2 \leq p_{so} \leq 10,000 \text{ psi.}$$

Thus

$$H = c_p t_i = 0.37 \left(\frac{100}{p_{so}} \right)^{1/2} (W(Mt))^{1/3} c_p.$$

The restrained modulus is related to the effective seismic velocity, the mass density, and Young's modulus of elasticity of the medium as follows:

$$\frac{E}{\rho} = c_p^2 = \left(\frac{E}{\rho} \right) \left(\frac{1 - \nu}{(1 + \nu)(1 - 2\nu)} \right),$$

where E is the Young's modulus of elasticity (psi), ρ is the mass density of the medium ($\rho = \gamma/g \text{ lb sec}^2/\text{ft}^4$, where γ is the unit weight of the medium in pounds per cubic foot and g is the gravitational acceleration constant), and ν is Poisson's ratio. For values of ν of 0.25 or less, the relation may be approximated by:

$$E = \rho c_p^2 \approx E.$$

If the unit weight of the soil is about 115 lb/ft³,

an approximate value of \bar{E} is

$$\bar{E} = 25,000 \left(\frac{c_p}{1,000} \right)^2, \text{ psi.}^*$$

Substituting the values for H and \bar{E} gives

$$d_{se} = 9 \left(\frac{P_{so}}{100} \right)^{0.5} \left(\frac{1,000}{c_p} \right) (W(Mt))^{1/3} \text{ inches.}$$

The permanent vertical displacement is not so easily estimated; at present the best estimates can be made by considering the static stress-strain properties of the soil. In the absence of better information, it is suggested that the permanent displacement at the surface be taken to be the following for overpressures greater than 40 psi:

$$d_{sp} = \frac{P_{so} - 40}{30} \left(\frac{1,000}{c_p} \right)^2 \text{ inches,}$$

where c_p is the seismic velocity of the material near the surface.

From wave propagation theory it may be demonstrated that the following relationship exists for particle velocities in terms of the dimensional units defined above.

$$v = c_p \frac{P_{so}}{\bar{E}} = c_p \epsilon,$$

where ϵ is the strain. Upon substitution this gives the maximum velocity

$$v_s = 50 \left(\frac{P_{so}}{100} \right) \left(\frac{1,000}{c_p} \right) \text{ in./sec.}$$

For a rise time of velocity of about 0.002 seconds, and considering a parabolic rise

with a 20 percent increase for nonlinearity, the maximum acceleration at the surface, computed as a rate of change of velocity, may be expressed by

$$a_s \approx 150 \left(\frac{P_{so}}{100} \right) \left(\frac{1,000}{c_p} \right), g.$$

Since the surface acceleration is not related solely to the maximum velocity, but is partially dependent on the weapon yield and other factors, it is recommended that a value of c_p no greater than 2,000 fps be used in this expression, regardless of the actual surface seismic velocity.

Horizontal effects data are lacking for the surface. At present, it is recommended that the maximum horizontal deflection be taken as one-third the vertical, the maximum horizontal velocity as two-thirds the vertical, and the maximum horizontal acceleration as equal to the vertical.

The same type of reasoning can be followed in arriving at maximum values of acceleration, velocity, and displacement at depths below the surface. The difference in deflection between the surface and some point at a depth y beneath the surface cannot exceed the surface stress divided by the lower restrained modulus of deformation, \bar{E} , in the interval y , and multiplied by the depth y . Thus between the surface and a depth y , not greater than 100 ft, assuming no attenuation of pressure with depth, an upper limit of the elastic component of differential displacement is given by

$$d_s - d_y \approx \frac{P_{so}}{\bar{E}} y.$$

The actual difference in deflection is more likely to be one-half this value, and may be

If the unit weight of the medium differs significantly from 115 lb/ft³, a representative value of \bar{E} should be used rather than the approximation given here.

considered to vary linearly to a depth of 100 ft, which results in the following expression

$$d_{se} - d_{ye} = 2.4 \left(\frac{p_{so}}{100} \right) \left(\frac{1,000}{c_p} \right)^2 \left(\frac{y^*}{100 \text{ ft}} \right) \text{ inches}$$

where $y^* = y$ for depths of 0 to 100 ft, and $y^* = 100$ ft for depths greater than 100 ft.

It is not generally considered desirable to assume any attenuation of displacement, except for very soft soils. Since total impulse must be preserved, the wavelength of the strain pulse probably increases with depth, and, therefore, it does not seem reasonable that there should be a reduction in elastic component of displacement consistent with the reduction in peak stress, as given by the attenuation relationships for stress or velocity with depth.

It is recommended that the permanent displacement of soils at depths below the surface be determined by multiplying the permanent displacement at the surface by $(100 - y^*)/100$, i.e.,

$$d_{yp} = d_{sp} \left(\frac{100 - y^*}{100} \right)$$

$$= \frac{p_{so} - 40}{30} \left(\frac{1,000}{c_p} \right)^2 \left(\frac{100 - y^*}{100} \right) \text{ inches.}$$

Thus, permanent displacements below 100 feet would be taken to be zero. At depths less than 100 feet, the total displacement should be taken as the sum of the elastic displacement at the surface, d_{se} , shown previously, and the permanent displacement, d_{yp} , given above.

The value of maximum stress below the surface is given approximately, for any yield or overpressure, by the following expression

$$p_y = \alpha p_{so}$$

where

$$\alpha = \frac{1}{1 + \frac{y}{H}}$$

and for depths that are not near the surface

$$H = 230 \left(\frac{100}{p_{so}} \right)^{0.5} (W(Mt))^{1/3}$$

Note: The attenuation factor, α , that is used in this section is different than the corresponding attenuation factor $1/\beta$ that is used in Section II, "Damage to Belowground Structures," of Chapter 11, "Damage to Structures." The attenuation factor given in Figure 11-29, Section II of Chapter 11 is the result of more recent studies. It reflects the influence of soil type (as represented by its seismic velocity) on peak pressure or soil particle velocity attenuation. The disparity between the two factors increases as the peak overpressure and/or the soil seismic velocity increase, but the disparity is relatively insensitive to variations in weapon yield. As a result of the influence of seismic velocity, the difference between the two factors also increases as the depth below ground surface increases. The factor given in Figure 11-29 gives substantially smaller attenuation rates under high overpressures and high seismic velocities than does the factor used in this section. Consequently, from the "vulnerability analysis" point of view, the factor of Figure 11-29 is more conservative, and its use in shock analysis studies is generally recommended. The attenuation factor obtained from Figure 11-29 may be introduced into the equations of this section by simply replacing " α " of this section with " $1/\beta$," where " β " is obtained from Figure 11-29. As mentioned previously, it is recommended that this replacement be made, in general; however, there is

one important exception. The factor $1/\beta$ is not compatible with the shortcut vulnerability curves shown in Figures 11-48 through 11-50, and calculations of similar curves that are compatible with the $1/\beta$ attenuation factor have not been performed at this time. It is for this reason that the α attenuation factor is introduced here, and its use will be illustrated in Problem 2-27. The use of the $1/\beta$ attenuation factor is illustrated in Problems 11-3 and 11-4.

At depths below the surface, it is recommended that velocities be attenuated in about the same manner as the maximum stress. Thus, the vertical velocity at any depth y is given by

$$v_y = \alpha v_s$$

The peak downward acceleration attenuates sharply with depth, especially near the surface. The sharp attenuation is caused primarily by the increase of rise time in the stress or velocity with depth.

The time of rise of the maximum velocity from an initial zero value can be taken as one-half the transit time of the shock wave from the surface to depth considered. For a parabolic rise in velocity the acceleration can be considered to be twice the value for a linear rise, which leads to the expression

$$a_y = 2 \frac{v_y}{t_r} = 5 \left(\frac{p_{so}}{100} \right) \frac{100}{y} \alpha g$$

where t_r is the effective velocity pulse rise time. This expression gives values which appear to agree well with test data for depths greater than 10 ft.

In the absence of better information at depths below the surface, it is recommended that the ratios of horizontal to vertical effects be taken equal to those previously specified for the surface, i.e., horizontal deflection is one-third

the vertical, the maximum horizontal velocity is two-thirds the vertical, and the maximum horizontal acceleration is equal to the vertical.

Layered media pose a complicated situation, but with care and judgment, reasonable estimates of acceleration, velocity, and displacement can be made. A convenient method is to use the stepwise passage of a stress wave downward through the medium. In general, the basic concepts governing the computation of displacement, velocity, and acceleration are the same as those described for a uniform medium. The displacements at any particular time may be computed by dividing the average pressure in an interval by the modulus of elasticity to obtain the strain and then multiplying by the length of the interval to obtain the displacement; the total displacement occurring over the length of the pulse is the sum of the incremental displacements.

Complications arise at the interface of two media because of stress transmission and reflection. For soil and rock, the interface may not be sharply defined and the reflected and transmitted stresses probably do not follow the laws governing purely elastic media. If it is known that the interface is fairly sharp, an estimate of the reflected and transmitted stresses can be made from the following relationships:

$$p_t = \frac{1 - \psi}{1 + \psi} p_i$$

$$p_r = \frac{2}{1 + \psi} p_i$$

where ψ is the ratio of the impedances of the two media. The stresses at the interface must be taken as equal, and, from considerations of continuity, the displacements also are equal.

2-63 Outrunning Ground Motion

Outrunning ground motion occurs when the air-shock velocity U decays below the seis-

mic wave velocity c of the medium. In the most general sense, outrunning ground motions and direct-transmitted ground shock are different phenomena. Direct-transmitted ground shock is ground motion propagated through the ground media from the region of the crater (this is often denoted outrunning when it clearly arrives, as reflected or refracted waves from deep-seated layers, ahead of the blast front). Outrunning ground motion occurs when the air-induced ground motion begins to propagate more rapidly than the air blast shock front, as illustrated in Figure 2-88. In actual fact, the motion-time history at a point in the medium can be quite complicated, even random in nature, when air-induced, outrunning, and direct-transmitted effects all arrive at about the same time.

Some information on outrunning motions observed in field tests can be found in "Nuclear Geoplosics" (see bibliography). Computer codes that are presently being developed should provide guides to even better estimates of outrunning motions.

2-64 Direct-Transmitted Ground Shock

The energy transmitted directly to the earth from a surface or near-surface burst can be propagated effectively through competent material for long distances. Experimental data that demonstrate this are available from buried high explosive shots and from surface and contained nuclear weapon tests.

For a completely buried shot, the first portion of the strain or velocity record at a distance R from the point of burst has the form described in paragraph 2-60, i.e.,

$$T_R = \frac{R}{6c_p} \text{ to } \frac{R}{12c_p} \quad \text{and} \quad T_o = \frac{R}{2c_p} \text{ to } \frac{R}{c_p}$$

Without serious error, the relation between peak strain ϵ and peak particle velocity v is given by the equation previously shown in

paragraph 2-62, i.e.,

$$v = c_p \frac{P_{80}}{E} = c_p \epsilon.$$

Assuming that the steepest part of the velocity-time curve has a slope that is twice the average slope during the rise phase leads to the following relationship between the range of peak acceleration, peak velocity, and strain, all in the radial direction.

$$a_r = \frac{2v_r}{T_r} \approx \frac{12c_p^2}{R} \epsilon \text{ to } \frac{24c_p^2}{R} \epsilon.$$

An estimate of the maximum displacement d_r in the radial direction may be obtained by integrating the area under the positive phase of the velocity curve. If the velocity waveform is parabolic, then

$$d_r = \frac{2}{3} v_r T_o \approx \frac{1}{3} R \epsilon \text{ to } \frac{2}{3} R \epsilon.$$

If data for strain, acceleration, or displacement are available, approximate relations for the other quantities may be obtained. In general, the seismic velocity enters into the relationships as indicated in equations shown above.

Most of the available test data from which direct-transmitted shock effects may be estimated were obtained from buried nuclear and high explosive detonations. To extrapolate from the test data to estimate shock effects produced by surface nuclear detonations requires establishment of the equivalence factor relating buried HE to buried nuclear yield, and also establishment of the equivalence of fully buried detonations to surface detonations of the same type of explosive.

A yield effectiveness factor of 0.2 to 0.5 has been used to relate fully contained nuclear

explosions to fully contained HE explosions. To relate a surface nuclear burst to a fully contained nuclear burst, factors of 0.02 for a burst slightly above the surface to 0.05 for a burst slightly below the surface are recommended. Significant uncertainties exist regarding these equivalence factors.

Expressions for acceleration, velocity, and displacement have been derived on the basis of test data available for accelerations from shot RAINIER in Operation HARDTACK in volcanic tuff with a seismic velocity of 6,000 fps. For scaled ranges of $2,500 \text{ ft/Mt}^{1/3}$ and closer, and an equivalence factor of 0.05 as just discussed, the acceleration may be expressed as follows:

$$a_r = 0.4 \left(W(\text{Mt}) \right)^{5/6} \left(\frac{1,000}{R} \right)^{3.5} \left(\frac{c_p}{1,000} \right)^2, g.$$

Using the relations between acceleration, velocity, and displacement, and choosing the equations with coefficients of 12 and 1/3, respectively, this equation for acceleration may be used to arrive at the following equations for radial velocity and displacement for materials with seismic velocities less than 10,000 feet per second:

$$v_r = 12 \left(W(\text{Mt}) \right)^{5/6} \left(\frac{1,000}{R} \right)^{2.5} \left(\frac{c_p}{1,000} \right) \text{ in./sec}$$

$$d_r = 4 \left(W(\text{Mt}) \right)^{5/6} \left(\frac{1,000}{R} \right)^{1.5} \text{ inches.}$$

There is little or no information on tangential motions, and until additional information becomes available, it is recommended that maximum values of tangential acceleration, velocity, and displacement be taken as 1, 2/3, and 1/3 times the corresponding radial values.

It is desirable to consider the direct-transmitted effects as being applicable only at some distance below ground surface, except possibly at close in ranges. At scaled distances greater than $2,500 \text{ ft/Mt}^{1/3}$, the limited available data suggest a decrease in the rate of decay of motion with distance. Approximate expressions for radial acceleration, velocity, and displacement for materials with an average seismic velocity less than 10,000 fps are as follows:

$$a_r = 0.081 \left(W(\text{Mt}) \right)^{0.25} \left(\frac{1,000}{R} \right)^{1.75} \left(\frac{c_p}{1,000} \right)^2, g.$$

$$v_r = 4.8 \left(W(\text{Mt}) \right)^{0.5} \left(\frac{1,000}{R} \right)^{1.5} \left(\frac{c_p}{1,000} \right) \text{ in./sec}$$

$$d_r = 3.19 \left(W(\text{Mt}) \right)^{0.75} \left(\frac{1,000}{R} \right)^{1.25} \text{ inches.}$$

These expressions give only very approximate values. Geologic conditions can produce large and random variations in the motions at large distances. For materials with seismic velocities greater than 10,000 fps, e.g., granite rock materials, the field test data suggest the following relationships as being applicable at scaled ranges of about $2,700 \text{ ft/Mt}^{1/3}$ and closer.

$$a_r = 180 \left(W(\text{Mt}) \right)^{5/6} \left(\frac{1,000}{R} \right)^{7/2} \left(\frac{165}{\gamma} \right)^{5/6} \left(\frac{c_p}{18,000} \right)^{1/3}, g.$$

$$v_r = 30 \left(W(\text{Mt}) \right)^{5/6} \left(\frac{1,000}{R} \right)^{5/2} \left(\frac{165}{\gamma} \right)^{5/6} \left(\frac{18,000}{c_p} \right)^{2/3}, \text{ ft/sec.}$$

(U)

$$d_r = 12 \left(\frac{W(Mt)}{\gamma} \right)^{5/6} \left(\frac{1,000}{R} \right)^{3/2} \left(\frac{18,000}{c_p} \right)^{5/3}, \text{ inches.}$$

As would be expected from the different scaling relationships, the expression for materials with seismic velocities less than 10,000 feet per second and those for materials with seismic velocities greater than 10,000 feet per second show lack of agreement at a seismic velocity of 10,000 feet per second, which divides the areas of applicability. This matter is currently receiving further attention, but in the interim it is believed that the expressions provide the best estimates of such motions.

No expressions exist for motions at large distances in hard materials that are comparable to the expressions presented above for soft materials. It was necessary to make approximate estimates to develop the relationships presented in Section III, Chapter 11.

2-65 Spectrum Concepts - Simple Systems

When structural systems or equipment are subject to a base disturbance, such as that arising from the ground motion associated with a nuclear explosion, the response of the system is governed by the distribution and magnitudes of the masses and resistance elements. A knowledge of the response of systems subjected to such loadings is extremely important from the standpoint of design in order to proportion the structure so that it will not undergo complete collapse, and to protect the structure, equipment, and personnel from shock damage. One of the simplest interpretations of ground motion data involves the concept of the response spectrum, which is a plot of the maximum response of a simple linear oscillator subjected to a given input motion as a function of frequency.

2-784
212

The time history of the actual motions of the earth caused by the passage of a shock wave over the surface is complex and is subject to considerable uncertainty. However, the principal effects on equipment and structural components can be described by use of the concept of the shock-response spectrum.

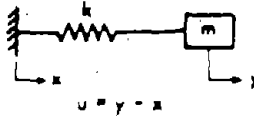
Consider a piece of equipment or an internal element of a structure supported at a point on an underground structure that is subjected to motion from blast. The equipment or element can be represented as a simple oscillator, consisting of a mass m attached by a linear spring of spring constant k to the base as shown in Figure 2-89(a). The natural frequency f of the oscillator is

$$f = \omega/2\pi = \frac{1}{2\pi} \sqrt{\frac{k}{m}}$$

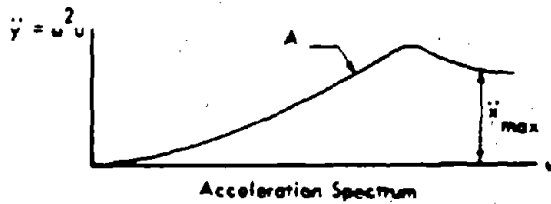
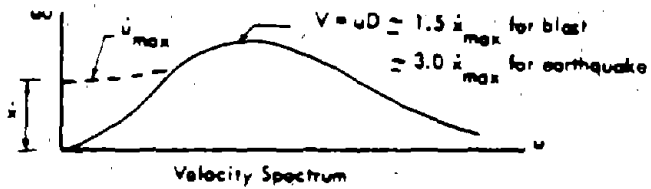
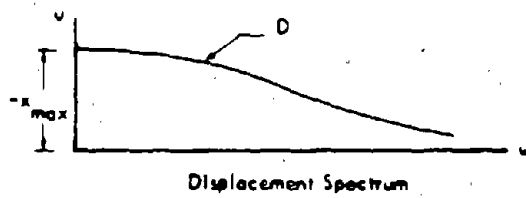
For a given transient ground motion x , the mass m will be set into motion. If the motion of the mass m is designated by the coordinate y and the motion of the base by the coordinate x , the deformation in the spring u is $(y-x)$ and is positive when y exceeds x . For such a system the most useful spectra are found to be the following: the maximum relative displacement u of the system; the maximum relative velocity \dot{u} ; the maximum pseudo relative velocity or the quantity ωu , the circular frequency ω times the displacement u , which is not quite the same as \dot{u} and differs considerably from \dot{u} at low frequencies; and the absolute acceleration of the mass, $\omega^2 u$, which is nearly the same as \ddot{y} . A plot of the maximum values (denoted D , \bar{V} , V , and A_g , respectively) as a function of the frequency of the system for a given type of input constitutes a response spectrum for the particular function. These quantities are defined as follows:

$$A_g = |\omega^2 D| = (2\pi f)^2 D$$

$$V = |\omega D| = 2\pi f D$$



(a) SINGLE-DEGREE-OF-FREEDOM SYSTEM



(b) TYPICAL SPECTRA

Figure 2-89. Single-Degree-of-Freedom System and Typical Response Spectra



[REDACTED]

The maximum energy absorbed in the spring is associated with V . The quantity \bar{V} is not particularly useful.

For inputs of the type associated with air-induced or direct-transmitted ground shock, the spectra for a simple system will have the characteristic appearances shown in Figure 2-89(b). The limiting conditions that apply to the spectra illustrated in Figure 2-89(b) are of particular interest. For example, as the frequency of the system approaches zero, the mass m does not move when the base of the system has a given motion applied. Then the relative displacement u is equal to the negative value of x , and the relative velocity \dot{u} is equal to minus the maximum base velocity \dot{x} . The dotted line in Figure 2-89(b) indicates the difference between \dot{u}_{max} and V that may be observed in the region of low frequencies; likewise, there is some difference between \dot{u}_{max} and V at the high frequency end, but these differences are of a smaller order of magnitude. Typical values of V that might be expected for blast conditions are shown in Figure 2-89(b). An additional control is that as the frequency of the system becomes large, the displacement y approaches the displacement x , i.e., u approaches zero, and the acceleration \ddot{y}_{max} approaches \ddot{x}_{max} . These controls are of special importance in arriving at design shock spectra.

Ordinarily, the input for ground motion consists of two parts, a systematic portion on which is superimposed a series of random oscillations. The magnitude of the peaks of the random components may be either small or large compared to the systematic portion. The random part may exist over the entire range of the systematic portion, over only part of the range, or even may be prior to the systematic portion.

For a random series of pulses, the relative velocity peak of the spectrum compared with the maximum input velocity can be high, but it is not likely to be much higher than about 3, unless an almost resonant condition is obtain-

ed with several pulses of alternate positive and negative signs of exactly the same shape and duration. Such a resonant condition for velocity is extremely unlikely from blast loading, although it has been observed in long duration earthquake phenomena. Even if, for some reason, partial resonance is achieved, the dampening in the system being excited will reduce the peaks considerably.

In general, the combined effect of the two input motions, systematic and random, depends on their individual effects. It can be shown that the combined spectrum will be either equal to or less than the sum of the absolute values of the spectra corresponding to the individual inputs. It also appears reasonable that the combined spectrum can be expected to be approximately equal to the square root of the sum of the squares of the individual spectra, point by point. In most practical cases of the type under consideration, the frequencies for which the spectrum values are important differ by a considerable amount, and the sums of the spectra or the square root of the sums of the squares are nearly the same as the maximum individual modal value.

2-66 Shock Spectra for Free Field Ground Motion

Using the concepts discussed above, it is possible to derive shock spectra that can be used in design to assess the relative effects in a structure (above or below ground) or the effects on equipment within a structure. Such spectra can be described best by the use of a logarithmic plot that permits values of displacement, pseudo-velocity, and acceleration to be read versus frequency in accordance with the relations given by the equations in paragraph 2-65.

In accordance with the limiting conditions discussed for Figure 2-89, the response spectrum can be represented by three regions, each region defined by a straight line constituting an envelope to the actual spectrum. An

example of such a spectrum for air-induced shock for conditions of 100 psi surface pressure, 5 Mt yield, and an acoustic velocity of 2,500 ft/sec is shown in Figure 2-90 for situations at the surface and at a depth of 100 ft. The left hand region, at the low frequency side, is influenced primarily by the maximum elastic transient displacement. The intermediate part of the spectrum (horizontal line) is a function of the maximum velocity reached in the free field. The right hand side depends on the maximum acceleration. In brief, the approximate response spectrum "envelope" is described by three straight lines (actually there are discrepancies that may be as high as a factor of 2 in some areas, but the actual ground motions are now known even this accurately, and the simplification of the spectrum in this way is permissible).

- A line $D = \text{constant}$, parallel to the displacement scales, drawn with a magnitude equal to the maximum ground displacement.
- A line $V = \text{constant}$, drawn with a magnitude of 1.5 times the maximum ground velocity.
- A line $A = \text{constant}$, parallel to the acceleration scales, drawn with a magnitude equal to twice the maximum ground acceleration.

Spectra may be sketched for horizontal and vertical motions at various depths and employed as appropriate. Detailed procedures for constructing more accurate spectra may be found in "Effect of Inelastic Behavior on the Response of Simple Systems to Earthquake Motions," A. S. Veletsos and N. M. Newmark, and "Response Spectra Approach to Behavior of

Shock Isolation Systems," A. S. Veletsos and N. M. Newmark (see bibliography). In general, the air-induced and direct-transmitted ground motions, as well as the out-running ground motions, if applicable, are computed. The spectra of each are plotted, and the design is made according to the envelop of the spectra. If it is known that the motions will arrive at significantly different times, the design or analysis is only made for the worst case.

The response spectrum, such as that shown in Figure 2-90, may be used directly for elastic systems. If the frequency of equipment within a structure and its type and mode of support are known, it is possible to ascertain certain results in terms of the response of the system. For example, for a single-degree-of-freedom system, the number of gravities of acceleration corresponding to the natural frequencies may be considered as applied to the body to ascertain the dynamic stresses. For more complex systems, the analysis is more difficult, although consideration of the most significant mode will lead to useful estimates of dynamic loadings in many cases.

For purposes of comparison and interest, three shock spectra determined from reed gages or ground motion records in atomic field tests are shown in Figure 2-91. The Operation HARDTACK spectra exhibit high accelerations; this is likely to be the result of the high water table that tends to emphasize the high frequency end of the spectrum. The maximum velocity is much higher than would be expected in a typical soil site. The Operation PLUMBBOB data approximate the type of response that would be expected for more normal soil conditions.

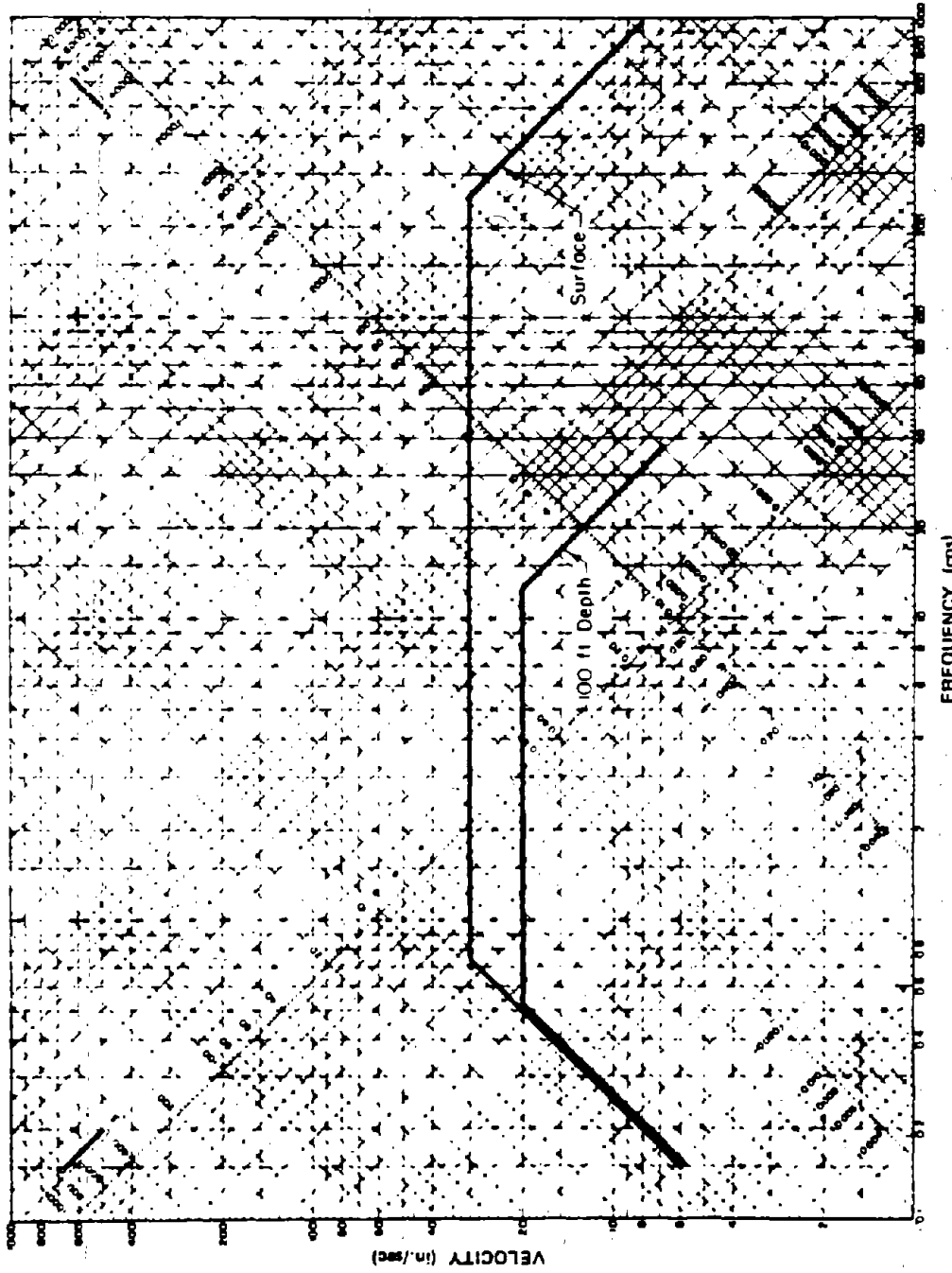


Figure 2-90. Response Shock Spectra, 100 psi Overpressure, 5 Mt Yield.
 c = 2,500 fps (Vertical Motion - Air-Induced Effects)

2-788
 716

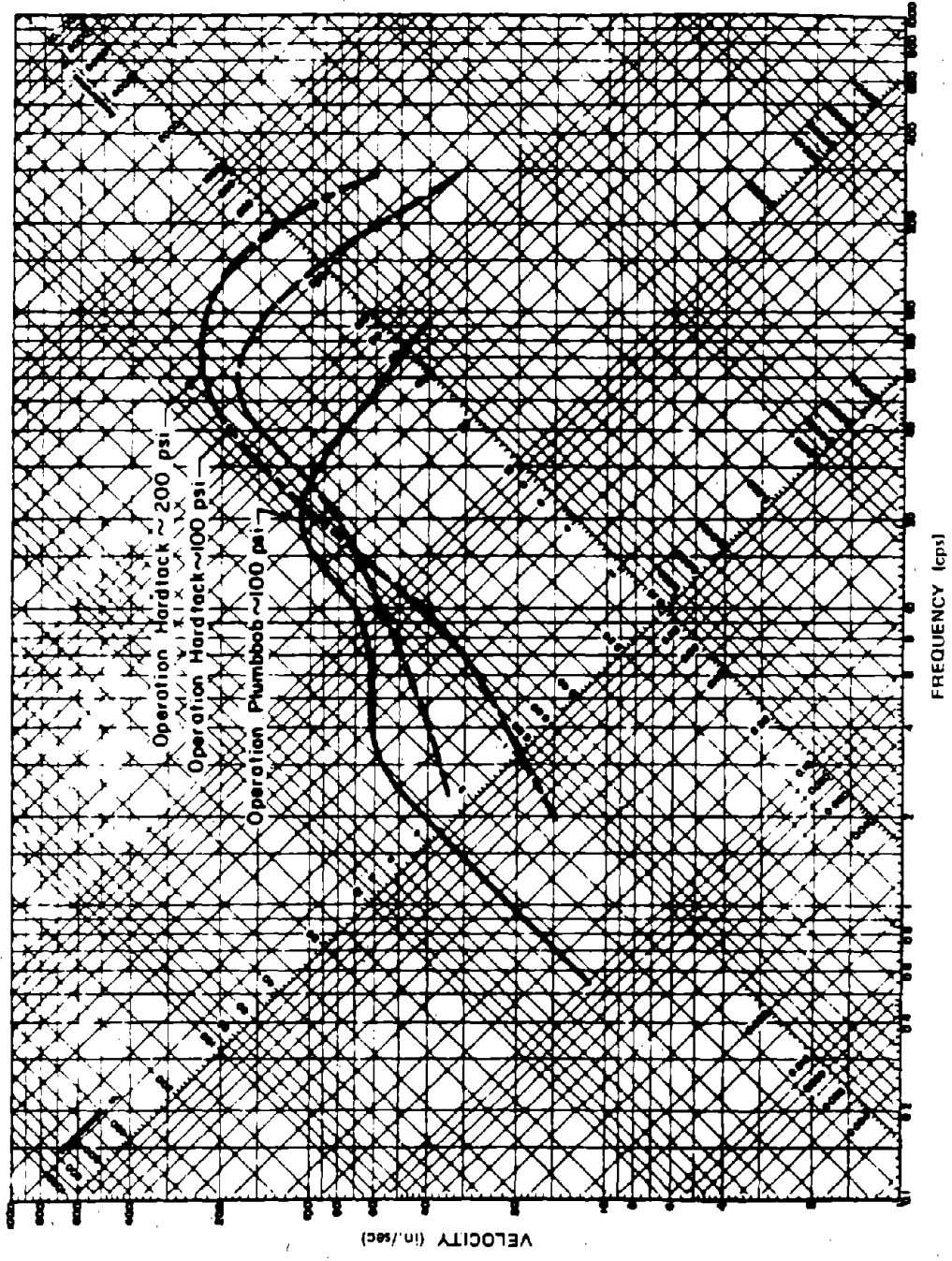


Figure 2-91. Typical Shock Spectra from Field Tests - Surface Data

**Problem 2-27. Calculation of the Ground Motions from
a Nuclear Explosion at the Surface**

The nature of the free field effects of ground motion are described in paragraphs 2-60 through 2-66. The attenuation factor α that is defined in paragraph 2-62 is used in the example presented below. As noted in paragraph 2-62, it generally is preferable to use the factor $1/\beta$ for attenuation, where β is described in Section II of Chapter 11, and more specifically in Figure 11-29. However, $1/\beta$ attenuation is not compatible with the equipment vulnerability curves in Figures 11-48 through 11-50. Therefore, the following example illustrates the use of the attenuation factor described in paragraph 2-62; use of the $1/\beta$ attenuation is illustrated in Problems 11-3 and 11-4.

Example

Given: A 1 Mt weapon burst on the surface of a medium that has a seismic velocity of 5,000 ft/sec.

Find: The vertical and horizontal displacement, velocity, and acceleration at a point 50 feet below the surface and at a ground distance of 1,500 feet from the explosion.

Solution: The equivalent distance for 1 kt

$$d_1 = \frac{d}{(W(kt))^{1/3}} = \frac{1,500}{(1,000)^{1/3}} = 150 \text{ feet.}$$

From Figure 2-17, the overpressure at the surface is about 1,000 psi.

a. *Air Induced Motions:* The maximum elastic vertical displacement at the ground surface is given by the equation shown in paragraph 2-62:

$$d_{se} = 9 \left(\frac{P_{so}}{100} \right)^{0.5} \left(\frac{1,000}{c_p} \right) (W(Mt))^{1/3}$$

$$= 9 \left(\frac{1,000}{100} \right)^{0.5} \left(\frac{1,000}{5,000} \right) (1)^{1/3} = 5.7 \text{ inches.}$$

It is reasonable to assume that impulse is preserved in the stiff medium described in this case. Therefore, the vertical elastic displacement at a depth of 50 feet will be the same as that at the surface, i.e., 5.7 inches. As described in paragraph 2-62, the permanent displacement at a depth of 50 feet is

$$\begin{aligned} d_{yp} &= \frac{P_{so} - 40}{30} \left(\frac{1,000}{c_p} \right)^2 \left(\frac{100 - y^*}{100} \right) \\ &= \left(\frac{1,000 - 40}{30} \right) \left(\frac{1,000}{5,000} \right)^2 \left(\frac{100 - 50}{100} \right) \\ &= 0.6 \text{ inches.} \end{aligned}$$

Thus, from paragraph 2-62 the total vertical displacement is

$$d_y = d_{se} + d_{yp} = 5.7 + 0.6 = 6.3 \text{ inches.}$$

The peak vertical velocity given in paragraph 2-62 is:

$$v_y = \alpha v_s,$$

where

$$v_s = 50 \left(\frac{P_{so}}{100} \right) \left(\frac{1,000}{c_p} \right),$$

$$\alpha = \frac{1}{1 + \frac{y}{H}}$$

and

$$H = 230 \left(\frac{100}{p_{so}} \right)^{0.5} (W(Mt))^{1/3}$$

This gives

$$H = (230) \left(\frac{100}{1,000} \right)^{0.5} (1)^{1/3} = 73$$

$$\alpha = \frac{1}{1 + \frac{50}{73}} = 0.59$$

$$v_x = 50 \left(\frac{1,000}{100} \right) \left(\frac{1,000}{5,000} \right) = 100 \text{ in./sec.}$$

$$v_y = (0.59)(100) = 59 \text{ in./sec.}$$

The vertical acceleration is given by the equation in paragraph 2-62 as:

$$\begin{aligned} a_y &= 5 \left(\frac{p_{so}}{100} \right) \left(\frac{100}{y} \right) \alpha \\ &= (5) \left(\frac{1,000}{100} \right) \left(\frac{100}{50} \right) (0.59) = 59 \text{ g.} \end{aligned}$$

As described in paragraph 2-62, the horizontal values of the motions are taken to be 1/3, 2/3, and 1 times the vertical displacement, velocity and acceleration, respectively, i.e.,

$$d_x = 1/3 d_y = \left(\frac{1}{3} \right) (6.3) = 2.1 \text{ inches,}$$

$$v_x = \frac{2}{3} v_y = \left(\frac{2}{3} \right) (59) = 39 \text{ in./sec,}$$

$$a_x = a_y = 59 \text{ g.}$$

b. *Direct Transmitted Motions:* The expressions given in paragraph 2-64 are applicable for direct transmitted motions. The radial motions are essentially horizontal for the distance and depth of this example. These are (note the distance is less than 2,500 ft/Mt^{1/3}):

$$\begin{aligned} d_r &= 4 (W(Mt))^{5/6} \left(\frac{1,000}{R} \right)^{1.5} \\ &= (4) (1)^{5/6} \left(\frac{1,000}{1,500} \right)^{1.5} = 2.2 \text{ inches.} \end{aligned}$$

$$\begin{aligned} v_r &= 12 (W(Mt))^{5/6} \left(\frac{1,000}{R} \right)^{2.5} \left(\frac{c_p}{1,000} \right) \\ &= 12 (1)^{5/6} \left(\frac{1,000}{1,500} \right)^{2.5} \left(\frac{5,000}{1,000} \right) \\ &= 22 \text{ in./sec.} \end{aligned}$$

$$\begin{aligned} a_r &= 0.4 (W(Mt))^{5/6} \left(\frac{1,000}{R} \right)^{3.5} \left(\frac{c_p}{1,000} \right)^2 \\ &= (0.4) (1)^{5/6} \left(\frac{1,000}{1,500} \right)^{3.5} \left(\frac{5,000}{1,000} \right)^2 \\ &= 2.4 \text{ g.} \end{aligned}$$

In this case, the motions normal to the radial motions may be taken to be vertical. These are 1/3, 2/3, and 1 times the corresponding radial values of displacement, velocity and acceleration, i.e.,

$$d_y = \frac{1}{3} d_r = \left(\frac{1}{3} \right) (2.2) = 0.7 \text{ inches,}$$

$$v_y = \frac{2}{3} v_r = \left(\frac{2}{3} \right) (22) = 15 \text{ in./sec,}$$

$$a_y = a_r = 2.4 \text{ g.}$$

[REDACTED]

Answer: The peak values of both horizontal and vertical motions, for air-induced and direct-transmitted shocks are:

	<u>d(in.)</u>	<u>v(in./sec)</u>	<u>a(g)</u>
<u>Vertical</u>			
Air-induced	6.3	59	59
Direct-transmitted	0.7	15	2.4
<u>Horizontal</u>			
Air-induced	2.1	39	59
Direct-transmitted	2.2	22	2.4

In this particular example the air-induced motions, with the exception of the horizontal displacement, are the largest values for both the vertical and horizontal directions. In the horizontal direction, the direct-transmitted value of displacement is nearly equal to that of the air-induced value. In many cases, especially at short range and for stiff media, it will be found that the direct-transmitted motions will be the largest, and will control the analysis. From paragraph 2-66, the bounds for the shock response

spectra are obtained by multiplying the controlling displacement, velocity, and acceleration values by 1, 1.5, and 2.0, respectively.

Vertical Response Spectrum Bounds:

$$D = 1.0d = 6.3 \text{ in.}$$

$$V = 1.5v = 89 \text{ in./sec}$$

$$A = 2.0a = 118g$$

Horizontal Response Spectrum Bounds:

$$D = 1.0d = 2.2 \text{ in.}$$

$$V = 1.5v = 59 \text{ in./sec}$$

$$A = 2.0a = 118g$$

These spectra bounds are shown in Figure 11-51. They show the response spectra for a single-degree-of-freedom system. These bounds are used in the analysis of the vulnerability of equipment mounted in an underground structure in Problem 11-8.

Related Material: See paragraphs 2-24, 2-60 through 2-66, and Sections II and III of Chapter 11.

[REDACTED]

SECTION IV
[REDACTED] UNDERWATER EXPLOSION
PHENOMENA [REDACTED]

[REDACTED] An underwater nuclear explosion is characterized initially by the formation and propagation of an underwater shock wave. The dissipation of heat at the shock front causes the water to vaporize in the vicinity of the explosion and results in the formation of a large bubble of steam. The interaction of the bubble and the shock wave with the air-water interface produces various surface phenomena, including spray domes, columns, plumes, base surges, radioactive pools and surface waves. If the explosion is on or near the bottom, a crater is formed.

[REDACTED] An underwater nuclear explosion also can result in thermal, nuclear, and electromagnetic radiation above the surface, but these phenomena are insignificant, except in the case of a shallow burst. These phenomena, when caused by a shallow burst, should approximate those from a shallow underground explosion.

2-67 Underwater Bubble [REDACTED]

[REDACTED] An underwater nuclear explosion releases large amounts of thermal and nuclear radiation, essentially all of which is absorbed by the surrounding water within several feet of the explosion (some radiation in the visible spectrum can be radiated to greater distances, depending on the transparency of the water).

[REDACTED] During the early stages of the explosion, the warhead materials attain a very high temperature (tens of millions of degrees) and a very high pressure (on the order of millions of atmospheres). Energy acquired by these materials is transferred to the layer of water nearest the bomb, which is heated and compressed and which, then, heats and compresses the next outward layer. A compression wave (or hydrodynamic shock front) is formed by this mechanism, and this wave moves outward from the

explosion at a speed greater than that of sound. This shock front expands faster than the material that it engulfs, which also moves outward, but at a slower rate.

[REDACTED] As the shock front moves away from the point of explosion, energy is dissipated as heat, which raises the temperature of the water engulfed by the shock front. The largest temperature increase occurs near the center of the explosion, where the water is not only vaporized but dissociated as well. At greater distances, the water is vaporized and turned to steam at the shock front. At still greater distances, the water is not heated by the shock front sufficiently to boil. The bubble that is formed does not have a clearly defined "surface." Figure 2-92 shows this progression in a highly stylized form.

[REDACTED] Thus, shortly after an underwater burst an expanding bubble is formed, which is composed largely of vaporized water with radioactive bomb debris at its center, surrounded by heated water. Large quantities of neutron-activated elements in the sea water are also present in the steam and layer of surrounding water; however, the total induced radioactivity is relatively small compared to the fission product radioactivity. Continued expansion of this bubble reduces the pressure within it. As the bubble pressure falls below the vapor pressure of the heated water, additional water flashes to steam at the interface of the bubble and the water.

[REDACTED] If the explosion is deep underwater, the bubble continues to expand at a decreasing rate until a maximum size is reached. If it is not too near the surface or the bottom, the bubble remains nearly spherical to this point. As a result of the inertia of the water surrounding the expanding bubble, the bubble actually overexpands, i.e., when it attains its maximum size, its pressure is below the ambient water pressure. The high pressure around the bubble then causes it to contract with an increase in its pressure and

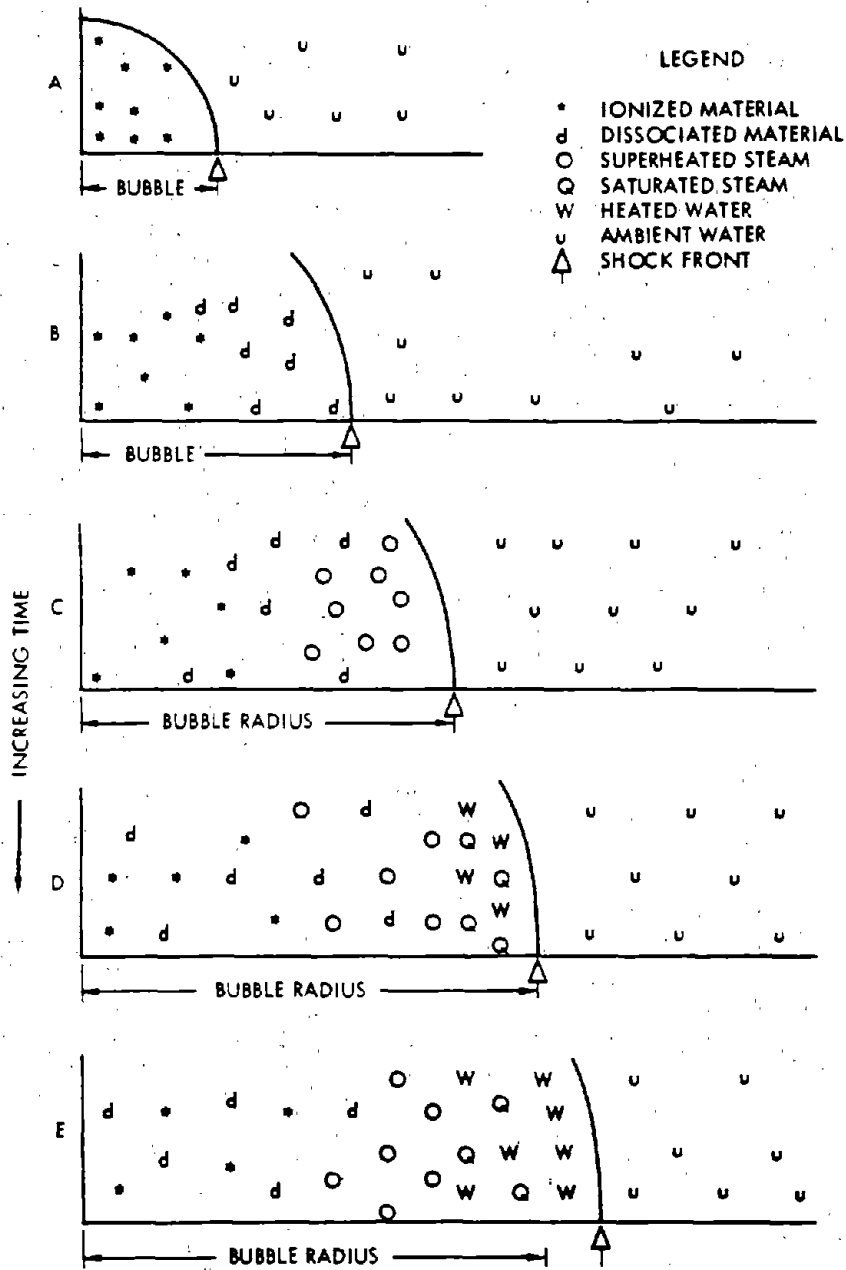


Figure 2-92. Representation of Bubble Development

condensation of some of its steam. Since the hydrostatic pressure is larger at the bottom of the bubble than at the top, the bubble does not remain spherical during the contracting phase. The bottom moves upward faster than the top (which may even remain stationary) and contacts the top to form a toroidal, or doughnut-shaped, bubble as viewed from above. This causes turbulence and mixing of the bubble contents with the surrounding water.

The inertia of the water set in motion by the bubble contraction causes it to overcontract, and its internal pressure becomes very much higher than the ambient water pressure. A second compression wave (the first bubble pulse) commences when the bubble reaches its minimum volume. This wave has a lower peak pressure, but a longer duration, than the initial shock. A second cycle of bubble expansion and contraction begins.

When the bubble pulse is emitted, the bubble surface becomes exceedingly unstable; a multitude of water spray jets shoot inward, thereby condensing much of the steam and degrading the bubble energy. Figure 2-93 shows the relative partitioning of the energy of the explosion with time qualitatively.

The bubble is relatively stationary during the initial expansion cycle, but upon contracting, it begins to migrate upward under the action of buoyant forces. The rate of upward migration is greatest when it is contracted and nearly zero when it is expanded.

If the bubble is far enough below the surface, it continues to pulsate and rise, though after three complete cycles enough steam will have condensed to make additional pulsations unlikely. During the pulsation and upward motion of the bubble, the water surrounding the bubble acquires considerable upward momentum and eventually breaks through the surface with a high velocity (about 200 mph for Wigwam, a deep underwater shot) thereby creat-

ing a large plume.

If the explosion is at a shallow depth, the bubble may break through the surface during one of the early pulsations, or even during the first pulsation cycle. If such a breakthrough occurs when the bubble pressure is higher than ambient (as with a very shallow explosion), a phenomenon known as a "blowout" occurs. If a breakthrough occurs when bubble pressure is below ambient, "blowin" occurs. The surface effects differ markedly for the two phenomena (see Figures 2-100 and 2-101 and accompanying text). A migrating bubble will not produce a bubble pulse if the bubble minimum occurs at or above the original water surface.

A strongly migrating bubble might continue to expand and not pass through a maximum size, somewhat like a balloon rising through the atmosphere. This is the balloon effect. A bubble migrating in this manner will not emit any bubble pulses. The conditions that cause a nuclear bubble to balloon rather than to pulsate are still subject to speculation; however, the absence of an expected bubble pulse might be explained by the balloon effect.

The maximum bubble radius and the first bubble period (time between burst and first minimum) are related to yield and depth of burst, as illustrated by the following two equations, which pertain to submerged bursts, i.e., the depth of burst, d_b , is greater than A_{max} :

$$A_{max} = J' \frac{W^{1/3}}{Z^{1/3}},$$

$$T_1 = K' \frac{W^{1/3}}{Z^{5/6}},$$

where

A_{max} = Maximum bubble radius (ft),

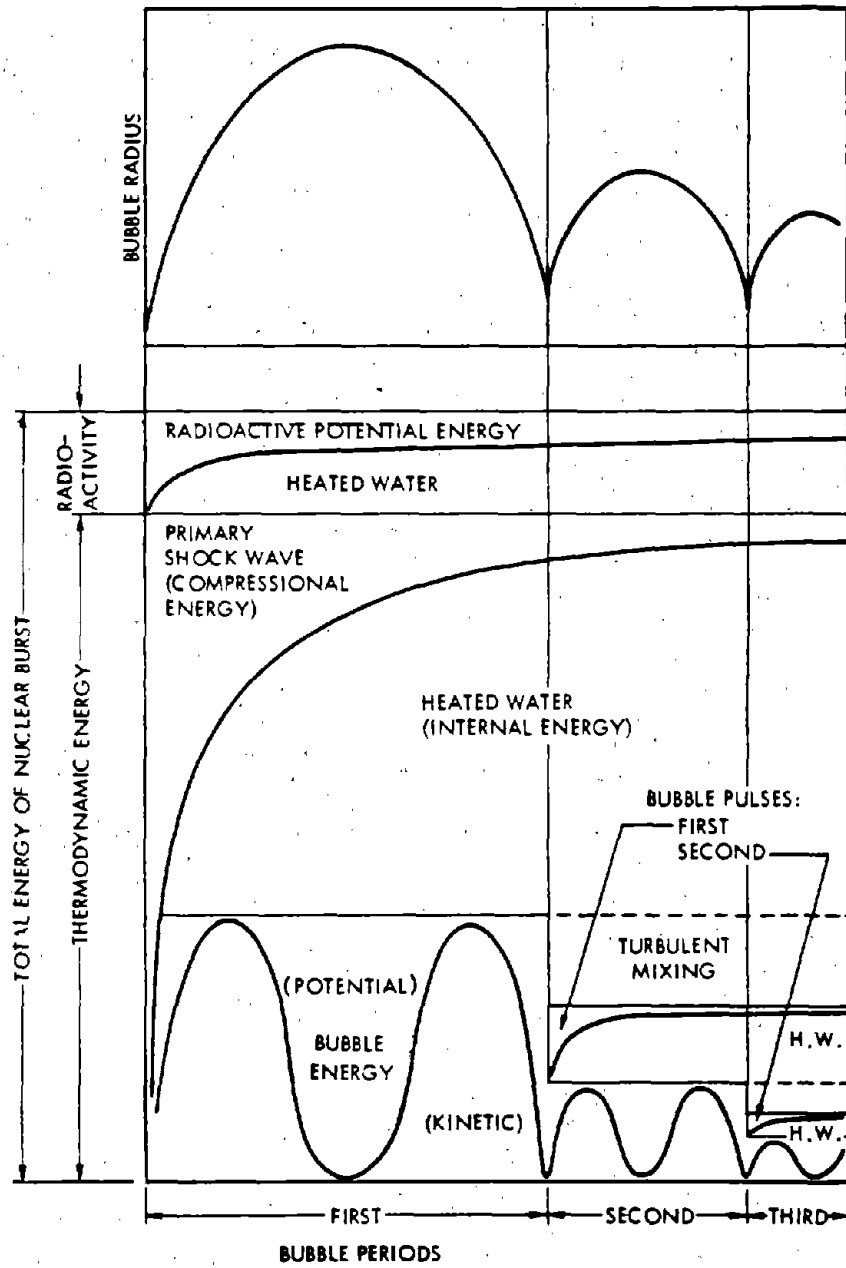


Figure 2-93. Energy Distribution Following an Underwater Nuclear Burst

2-796-
224

J' = Empirical constant, 1500,

K' = Empirical constant, 515,

T_1 = First bubble period (sec),

W = Yield (kt),

Z = Hydrostatic head ($d_b + 33$) (ft).

The form of the equations is the same as those given by Cole for high explosives. The constants, J' and K' , are slightly different because an underwater nuclear burst forms a steam bubble rather than gas bubble (as do high explosives) and because of other differences, mainly the distribution of total energy between bubble energy, shock wave energy, and residual radioactive energy.

It is likely that the constants J' and K' are actually somewhat dependent on depth. This can be understood qualitatively as follows: J' and K' implicitly include the fraction of explosion energy included in the bubble. As the depth of burst is increased, a smaller fraction of explosion energy is converted to steam by the expanding shock wave (and more energy goes into heating water) because of the greater hydrostatic pressure that must be overcome to boil water.

The second and third bubble maximum radii, the periods between minima, and the migration between periods, depend on the fraction of bubble energy that remains following succeeding bubble minima. The energy loss that occurs is due primarily to steam condensation at bubble minima as previously described, but the amount of energy loss is influenced by the depth at which the minimum occurs. An analytical representation of the energy as a function of bubble migration, which is best solved by use of a high-speed computer, has been developed,* however, satisfactory solutions to bubble problems can be obtained by use of curves derived from the rep-

resentation, as illustrated in Problem 2-28.

WATER SHOCK WAVE AND OTHER PRESSURE PULSES

The initial shock wave from an underwater explosion propagates radially from the source. This shock wave is characterized by an abrupt, virtually instantaneous, increase in pressure followed by a decrease that is approximately exponential. Near the explosion, the peak shock wave pressure is extremely high, but energy losses to the water cause the pressure to decrease somewhat faster than inversely with radius. Similarly, early shock wave propagation velocities are high, but by the time the peak pressure falls to about 3,000 psi, the propagation velocity becomes nearly equal to the acoustic speed in water (about 5,000 ft/sec), and the energy losses become small.

If an explosion takes place far from either the surface or the bottom, the shock wave remains spherical as long as it propagates into water having constant acoustic velocity. This velocity depends on temperature, hydrostatic pressure, and salinity, however, and in regions of the ocean in which significant sound velocity gradients exist, the shock wave can be bent or refracted. Refraction can either increase or decrease the shock wave pressures locally, depending on ambient water conditions. No general prediction techniques can be given, but the subject is discussed further in paragraph 2-71.

When a shock wave moving in water encounters another medium, it may be reflected as a tensile or rarefaction wave, as in the case of a water-air boundary; a compression or shock wave, as in the case of a water-bottom interface if the angle of incidence is not too far from the normal; or a distorted pulse having in general

* This expression is described in "The Parameters of Underwater Nuclear Explosion Bubbles" (see bibliography).

[REDACTED]

both a positive and a negative phase, as in the case of more glancing incidence at the bottom. These are discussed separately in the following paragraphs.

2-68 Surface Reflection

The rarefaction wave, generated by the reflection of the primary shock wave from the surface, propagates downward and relieves the pressure behind the primary shock wave. If the shock wave is treated as a weak (acoustic) wave, this interaction instantaneously decreases the pressure in the primary shock wave to a value that might be well below the vapor pressure of the water, as shown by the broken line in Figure 2-94, Point A. Cavitation occurs in seawater when its pressure decreases to a value somewhat below its vapor pressure. The pressure of the primary shock wave is, therefore, reduced to a value which, when compared with the peak pressure, is usually so close to ambient water pressure that the shock wave pulse appears to have been truncated, i.e., reduced to ambient pressure.

For a strong primary shock wave, the reflected rarefaction wave propagates into water that has already been set in motion by the shock wave. Therefore, the rarefaction wave arrives earlier than predicted from the acoustic approximation, and the pressure cutoff is not instantaneous. This effect typically gives a pulse shape shown by the solid line for Point A of Figure 2-94. The shallower the point at which pressure measurements are made, the sooner the primary shock pulse is "cut off" and, hence, the shorter its duration (see Figure 2-94, Point B). At sufficiently shallow locations, the rarefaction wave interacts with the shock front and reduces the peak pressure (see Figure 2-94, Points C and D). The region in which peak pressure is reduced is known as the "anomalous region."

The effects of surface reflection decrease rapidly with increased depth of either the explo-

sion or the point of measurement. Conversely, as the depth of burst is decreased (or the yield increased for a given depth of burst), the effects increase. The size of the anomalous region increases with decreased depth of burst until, for a surface burst, the anomalous region ~~increases~~ ^{includes} all points beneath the water surface except those close to the explosion and directly under it.

A limited amount of data are available concerning the reflection of shock waves from an ice layer. To date all tests have been with relatively small explosive charges (a majority of the test shots have been in the 1- to 40-lb range, with one shot of 630 lb). The situation is complicated by reflection and refractions at both the water-ice boundary and the ice-air boundary.

2-69 Bottom Reflection

Under certain circumstances, the shock wave from the bottom can be more damaging to surface ships and shallow submarines than the primary shock. Although the peak pressure of the reflected wave is usually smaller, the wave arrives at a steeper angle, and therefore may induce more damaging shock motion to a target at or near the surface.

2-70 Secondary Shocks and Pressure Waves

An underwater burst can cause compression waves in addition to those described above, but these effects are usually negligible. These waves include retransmitted pulses, cavitation pulses, bubble pulses, and others that are described briefly below.

- *Retransmitted Pulses.* Upon reflecting from the surface and bottom, some primary shock energy is transmitted into the air or bottom material, and some of this energy can be retransmitted back into the water.
- *Cavitation Effects.* As noted earlier, the reflection of the shock wave from the sur-

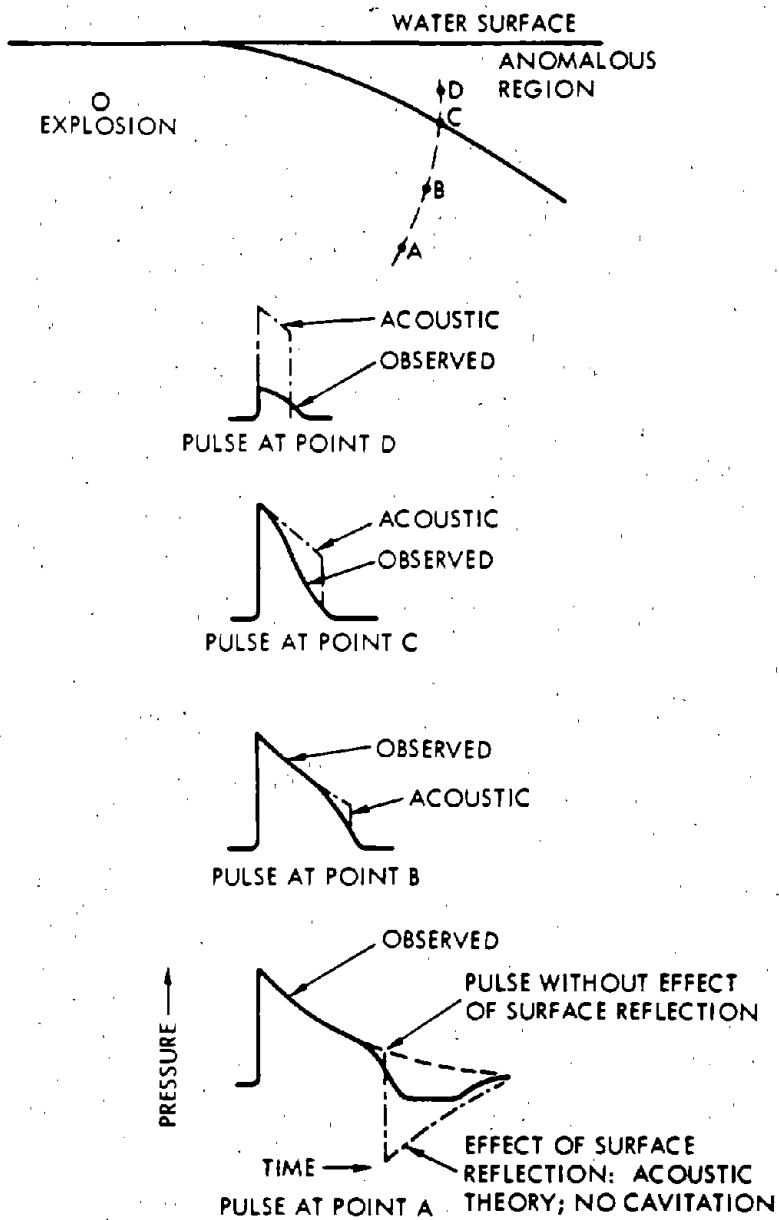


Figure 2-94. Typical Pressure Pulses Affected by Surface Reflection

face can lead to bulk cavitation below the surface. During the period of cavitation, the cavitated region can absorb further shock waves impinging on it. In the formation of the cavitation region, the rupture of the water by the shock wave causes a liquid surface layer (sometimes called "spall") to project upward in almost a ballistic trajectory. The impact of this spall when it returns to the surface can lead to further secondary shock waves. These shock waves account for the occasional larger damage to ships at intermediate ranges compared with the damage at shorter or longer ranges.

- *Bubble Pulses.* If an explosion is deep enough for one or more bubble pulsations to occur, compression waves are generated at the time of each bubble minimum.
- *Other Pulses.* All pressure waves are subject to multiple reflection from the surface and bottom. Also, in areas of irregular bottom topography, more than one reflected pulse can be generated.

Figure 2-95 shows typical shock wave and pressure pulse patterns for various burst and measurement conditions.

2-71 Refraction of Shock Waves

The shock front from an explosion far from a boundary (surface, bottom, etc.) remains spherical provided that it expands into water having constant acoustic velocity (isovelocity). However, the acoustic velocity in water depends on the temperature, salinity, and hydrostatic pressure, and these properties are not necessarily constant throughout a large body of water. As a result of variations in these properties, generally in horizontal layers, a region of water can have a characteristic acoustic velocity profile (sound velocity vs depth). Under such conditions, the shock wave is bent (refracted) because one part of the wave moves faster than another.

Refraction of the shock wave can result in convergence and reinforcement of the shock wave. This reinforcement commonly occurs along a surface called a "caustic." This effect may be illustrated by the use of a ray diagram* (Figure 2-96). The acoustic velocity profile that corresponds to the ray diagram is also shown in the figure. The formation of several caustics for one burst is observed frequently. Regions of relatively low pressure also occur, such as the "shadow zone" above the caustic in the figure.

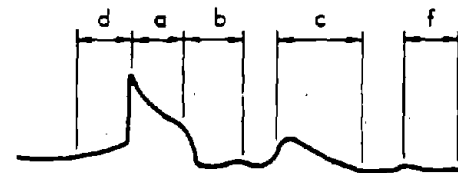
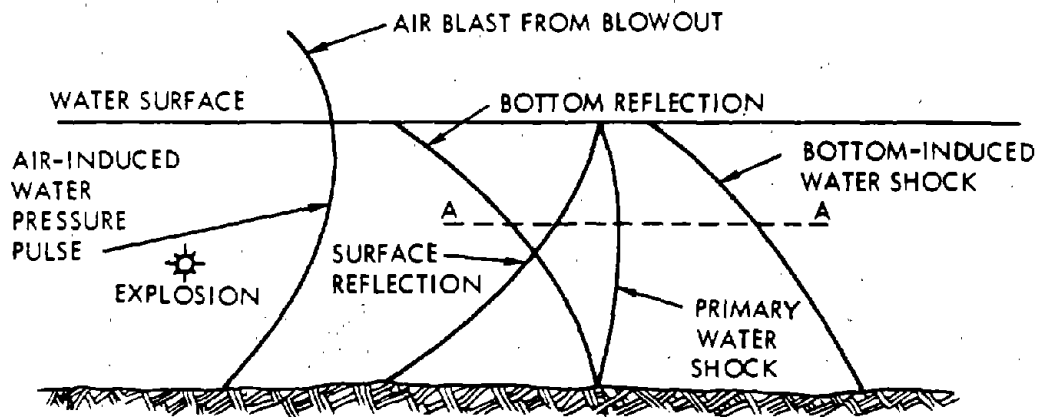
The caustic can reinforce the peak pressure by a factor of five or more over the isovelocity value, while the pressure observed deep in the shadow zone can be essentially negligible. Shock wave impulse amplification factors do not go through a maximum at the caustic position. They remain much closer to unity than do peak pressure and energy factors.

As a result of ocean currents and underwater swells, the acoustic velocity profile in the ocean is rarely stable. Thus, the location of the caustics can shift rather quickly and unpredictably (similar to optic mirages).

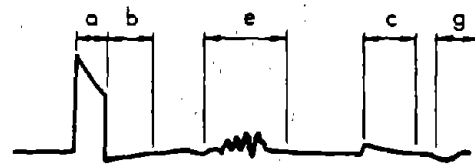
Common types of sound velocity profiles can give rise to caustics at various distances greater than about one mile. In particular, in about half of the areas of the oceans, a caustic occurs at what is known as the convergence zone, typically 30 (10 to 40) miles from an underwater burst. Therefore, it is conceivable that a submarine might suffer damage from its own multi-kiloton weapon detonated at a distance of about 30 miles if it happened to lie on the caustic of its shot.

In Figure 2-96, sound speed is considered to vary with depth only. Actually this would rarely happen. The velocity can vary considerably across the ocean within the range of interest. Generally, the region of focusing is sharper

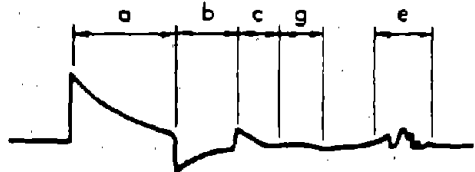
* A ray is generated by a curve that is always perpendicular to the expanding shock front.



1. SHALLOW EXPLOSION IN SHALLOW WATER
MEASUREMENT IN SHALLOW WATER



2. DEEP EXPLOSION IN MUCH DEEPER WATER
MEASUREMENT AT SHALLOW DEPTH



3. DEEP EXPLOSION IN MUCH DEEPER WATER
MEASUREMENT AT DEEP DEPTH

- a. PRIMARY SHOCK WAVE
- b. SURFACE REFLECTION
- c. BOTTOM REFLECTION

- d. BOTTOM-INDUCED PRESSURE PULSE
- e. SHOCK FROM CAVITATION COLLAPSE
- f. AIR-INDUCED WATER SHOCK
- g. OTHER

Figure 2-95. Typical Shock Wave Patterns Along Line A-A

2-202
2 30

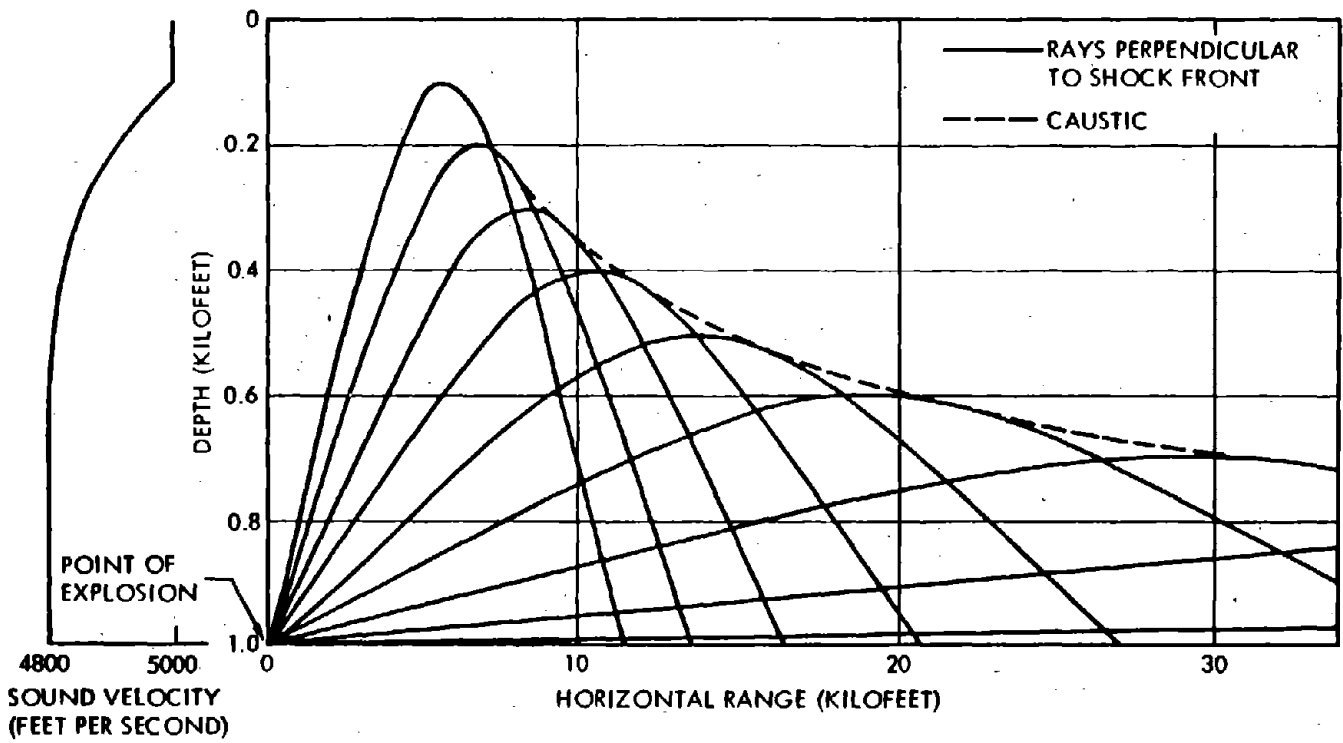


Figure 2-96. Ray Diagram for an Idealized Velocity Profile

[REDACTED]

and the maximum value of the amplification is greater for smaller yields.

2-72 Air Blast

The air blast wave has one to three pulses of various amplitudes, depending on the burst depth and the location of the observation point with reference to surface zero. These pulses are generated by two underwater explosion mechanisms: One is the underwater shock wave that transmits a portion of its energy across the water-air interface. The other is the underwater explosion bubble, which manifests itself in two ways: for burst depths shallower than about $35W^{1/3}$ feet, the bubble vents, causing an air pressure pulse; for burst depths deeper than $35W^{1/3}$ feet, a spray dome is pushed up by the expanding bubble, causing a bow wave.

For burst depths shallower than about $50W^{1/3}$ feet the transmitted pulse and the bubble generated pulse are formed almost simultaneously, resulting in a single intense pressure pulse over surface zero. For burst depths between $50W^{1/3}$ feet and about $150W^{1/3}$ feet, up to three pulses can be seen. The transmitted shock in air bifurcates near surface zero to form two air pulses, and the bow shock causes the third air pulse. For burst depths deeper than about $150W^{1/3}$ feet, the spray dome rises so slowly that no bow shock is formed and only the air pulse from the transmitted shock is important.

This discussion of the generation of air blast from underwater bursts is a simplified discussion of a complex subject. Much analytical, theoretical, and experimental work has been done to understand the physics of air blast generation. More complete discussions of the subject are given in Malme, Carbonell and Dyer (1966); Peckham and Pittman (1968); Pittman (1968); and Rudlin and Silva (1960) (see bibliography). Only a limited number of air blast measurements are available from nuclear weapon tests. The data are not sufficient to form a basis

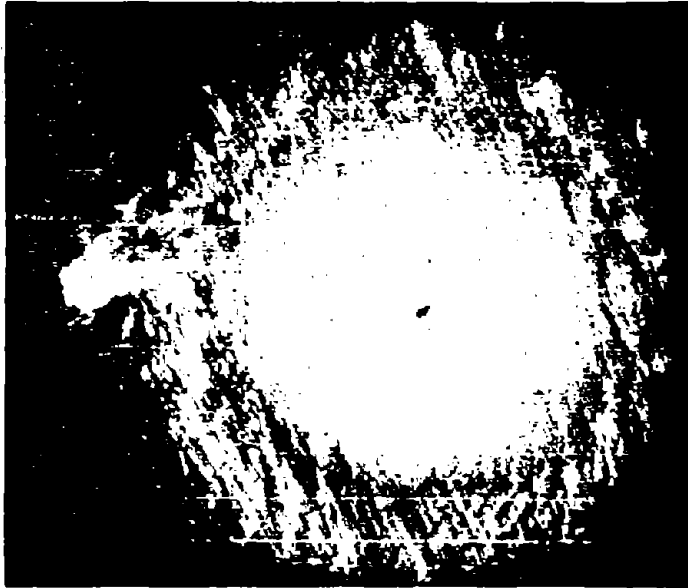
for predicting air blast for a spectrum of burst depths and pressure levels. The available predictive measures are based mainly on high explosive tests as described in Problem 2-31.

SURFACE EFFECTS OTHER THAN WAVES

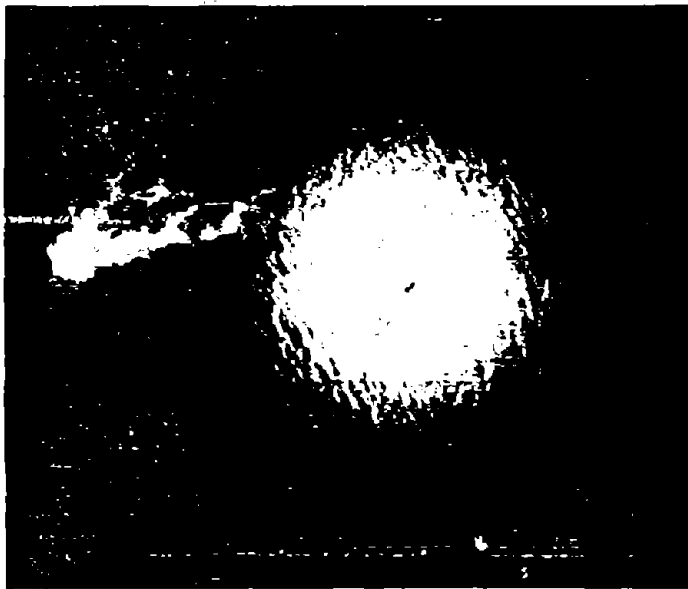
The first surface effect of an underwater burst is caused by the intersection of the primary shock wave and the surface. Viewed from above, the effect frequently appears to be a rapidly expanding ring of darkened water, often called the "slick" (Figure 2-97). A white circular patch (the "crack") follows closely behind the darkened region. The crack probably is caused by underwater cavitation produced by the reflected rarefaction wave. Shortly after appearance of the crack, the water above the explosion rises vertically and forms a white mound of spray, called the "spray dome" (Figure 2-98). This dome is caused by the velocity imparted to the water near the surface by the reflection of the shock wave and the subsequent breakup of the surface layer into drops of spray. Additional slick, crack, and spray dome phenomena may result if the bottom-reflected shock waves and bubble-pulse compression waves reach the surface with sufficient intensity (Figure 2-99).

The spray dome from a shallow burst changes rapidly to a shallow column formed by the upward and outward motion of the water surrounding the explosion bubble. If blowout occurs, the upper part of the column is likely to resemble a crown, which contains explosion products blown out of the column (Figure 2-100). If blowin occurs, the crown is likely to be absent (Figure 2-101a). In its later stages, the column may break up into column jets (relatively broad spouts of water that disintegrate into spray as they travel through the air) (Figure 2-101b).

If the burst is sufficiently deep to prevent blowout, but shallow enough for the bubble to continue to oscillate as it approaches the



(b) CAVITATION PULSE
Slick and Spray Ring
(0.73 sec after burst)



(a) PRIMARY SHOCK WAVE
Slick and Spray Dome
(0.28 sec after burst)



Figure 2-97. Slick Spray Dome and Cavitation Pulse Spray Ring (serial view)

2-204
232



Reproduced from
best available copy.




[REDACTED]



Figure 2-98. Spray Dome (3.3 sec after burst)

2-206
233

[REDACTED]

Reproduced from
best available copy. 

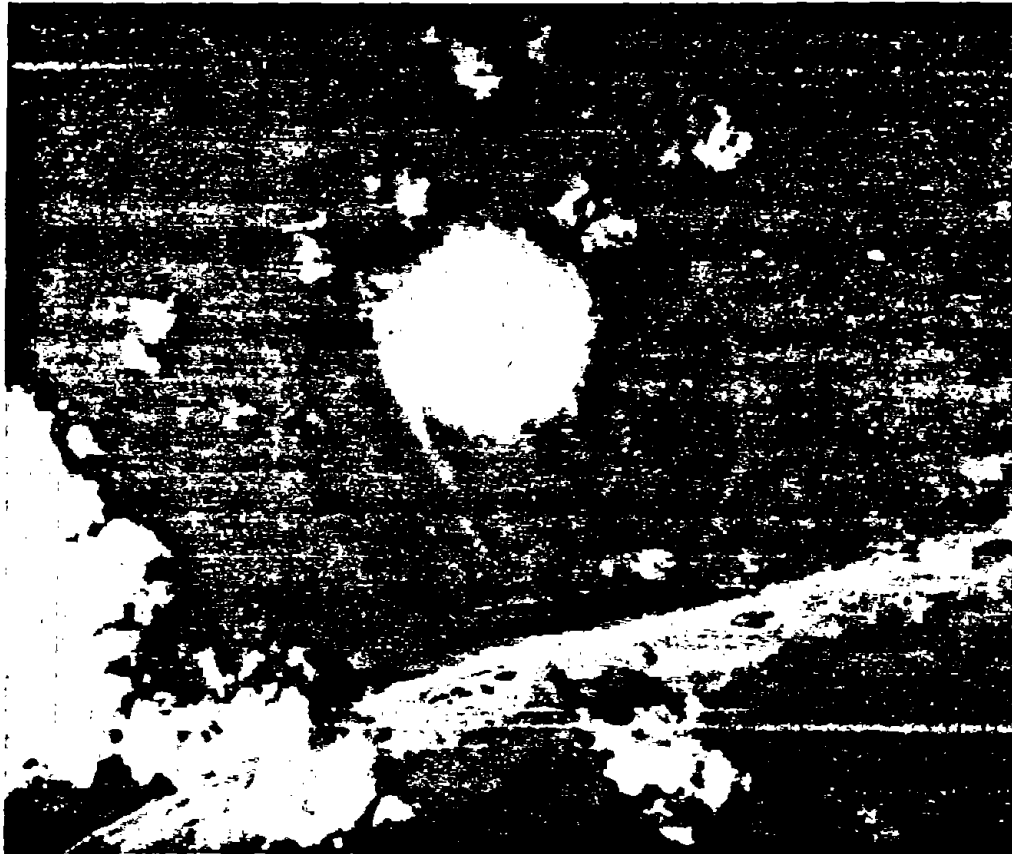


Figure 2-99. Bottom-Reflected Shock Wave Slick
(aerial view 1.38 sec after burst)

2-266
234

Reproduced from
best available copy.




[REDACTED]



Figure 2-100. [REDACTED] Very Shallow Burst Showing Crown of Explosion Products on Column (oblique aerial view 0.7 sec after burst) [REDACTED]

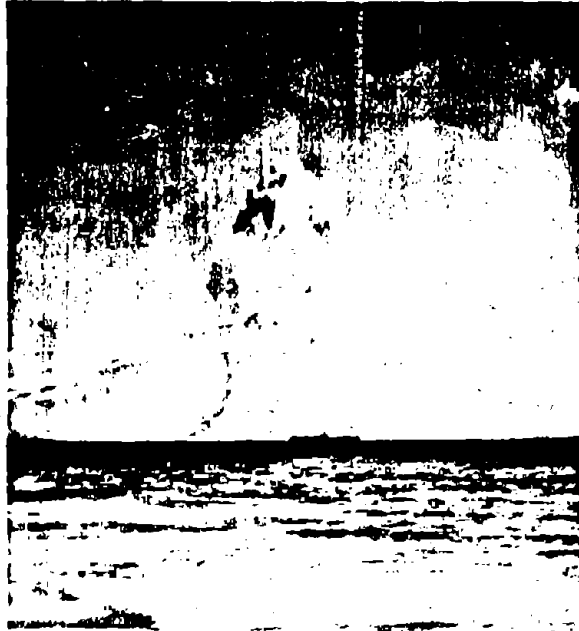
2-202
235

[REDACTED]

Reproduced from
best available copy. 

2-288
252

Reproduced from
best available copy.



(a) EARLY STAGE
(2.5 sec after burst)



(b) LATER STAGE SHOWING COLUMN JETS
(8.2 sec after burst)

Figure 2-101. Column from Shallow Underwater Burst (no blowout)

surface, plumes of upwelled water and steam can occur (Figure 2-102).

Upon subsidence of the column and plumes from an underwater explosion, a "doughnut-shaped ring" of mist is formed, which is called the base surge and which is highly radioactive (Figure 2-103). This ring, or series of rings, expands radially in the absence of wind, but in the presence of wind, it elongates and drifts with the wind until it dissipates. A train of surface waves also expands radially from the explosion.

After dissipation of the base surge, the water surface around the explosion appears white (Figure 2-104). This "foam-patch" results from the upward motion of water and gaseous explosion products in the vicinity of the bubble, their spreading over the surface of the patch, and their downward motion at the edge of the patch. During its later stages, the foam-patch appears as a ring of foam and debris that is left floating where the water circulates downward.

As previously noted, the surface phenomena described above vary with the weapon yield and the depth of burst. Although clear-cut distinctions cannot be made in all cases, six explosion categories have been established to aid in establishing safe weapon delivery criteria. These categories are defined in Table 2-8. The classifications have been tested at yields as large as 30 kt, but they probably are valid for yields up to about 100 kt.

The limits of the relations given in Table 2-8 are plotted in Figure 2-105, and the phenomena that establish the categories are described below.

- *Near-surface bursts.* The layer of water above the burst is vaporized by the explosion. The surface phenomena for this type of burst and the associated hazards are unknown. The radiological hazard of the base surge is considered to be unimportant compared with air blast and fallout

Table 2-8. Classification of Burst Depth Categories

Classification	Definition
Near surface	$0 < d_b < 21W^{1/3}$
Very shallow	$21W^{1/3} < d_b < 75W^{1/3}$
Shallow	$75W^{1/3} < d_b < 240W^{1/4}$
Deep	$240W^{1/4} < d_b < 700W^{1/4}$
Very deep	$700W^{1/4} < d_b$
Contained*	$1550W^{1/4} < d_b$
No spray dome*	$2500W^{1/3} < d_b$

* These values are derived from H.E. tests. They have not been confirmed by nuclear tests; therefore, they are to be interpreted as "containment possible" and "possible limiting depth for spray dome formation."

hazards.

- *Very shallow bursts.* The bubble vents early during the first expansion cycle, i.e., when the bubble pressure is greater than ambient, and fission products are blown out at that time.
- *Shallow bursts.* The bubble vents late during the first cycle, after the bubble pressure has dropped below ambient, and fission products are blown in.
- *Deep bursts.* The depth of burst is equal to or greater than the radius of the fully expanded bubble, but not as deep as the very deep burst described below.
- *Very deep burst.* The explosion is at sufficient depth that the bubble breaks up, becomes a vortex ring, or loses its identity before reaching the surface.

The surface radioactivity from a very deep burst is operationally insignificant within about an hour and may be faint enough to escape detection.

[REDACTED]

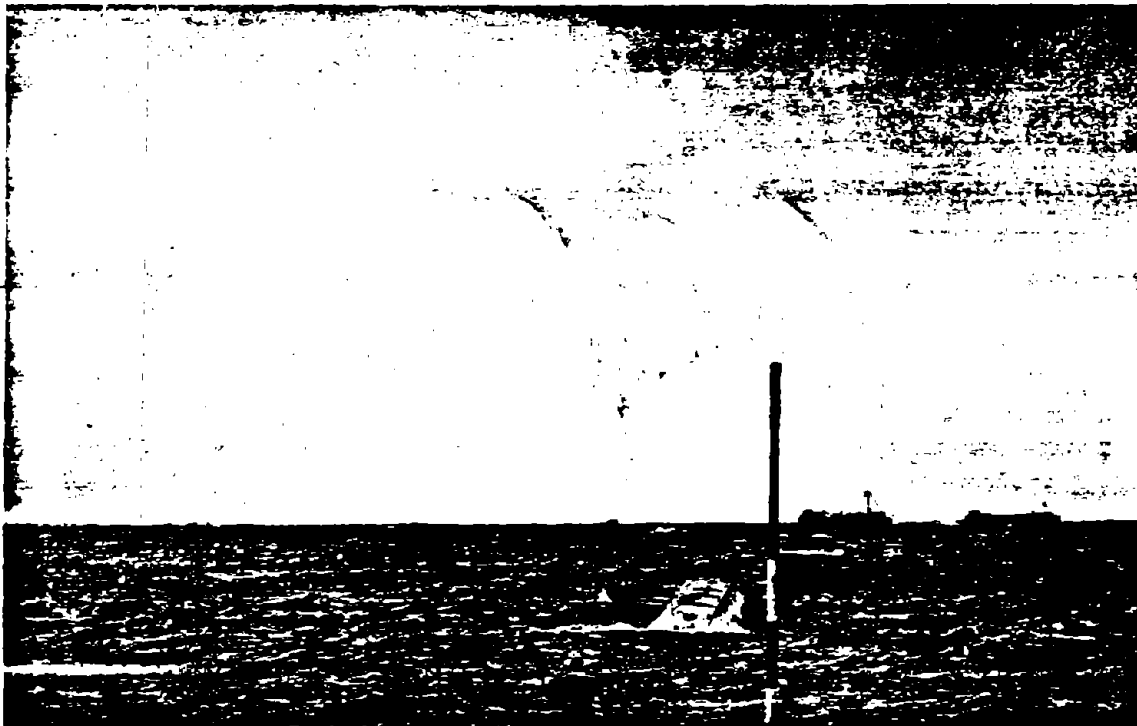


Figure 2-102. [REDACTED] Plume from Upwelling of Water from Very Deep Burst (24 sec after burst) [REDACTED]

2-218-
238

Reproduced from
best available copy.



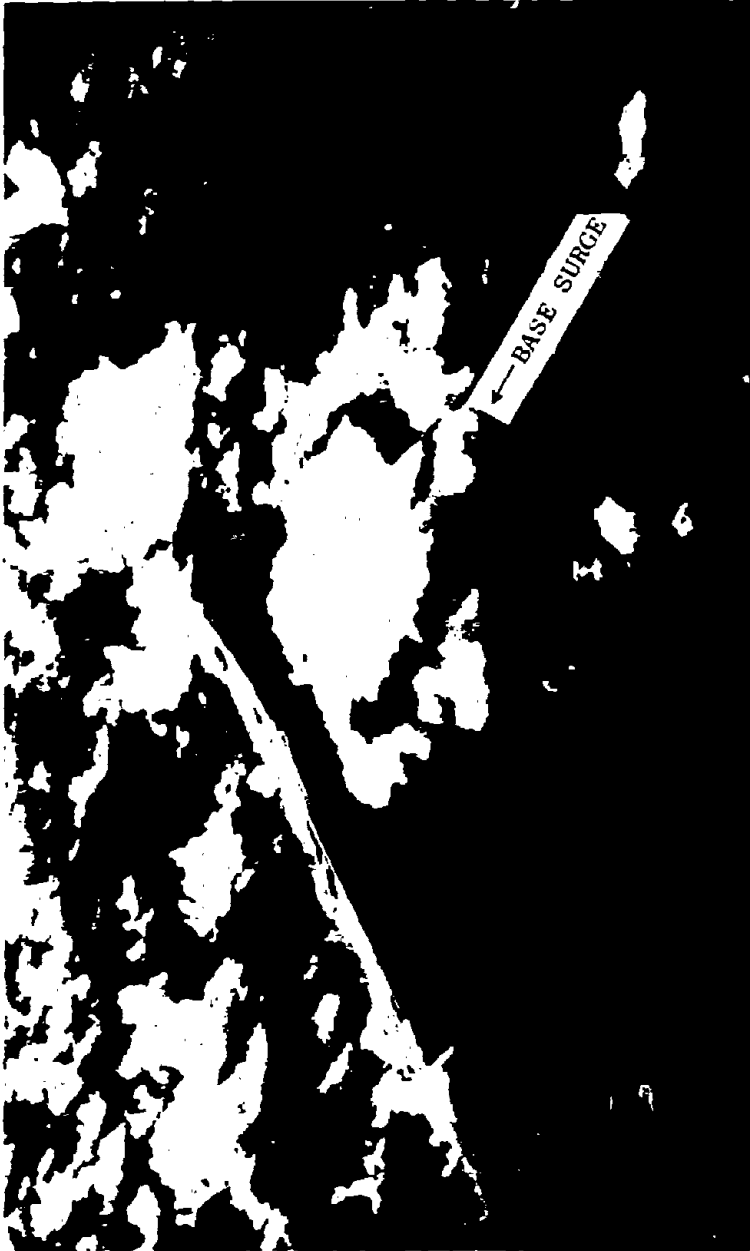


Figure 2-103. Base Surge "Doughnut-Shaped" Ring (oblique aerial view 100 sec after burst)

2-74
239





Figure 2-104. Foam Patch (oblique aerial view 8.3 min after burst)

2-242
240

Reproduced from
best available copy.



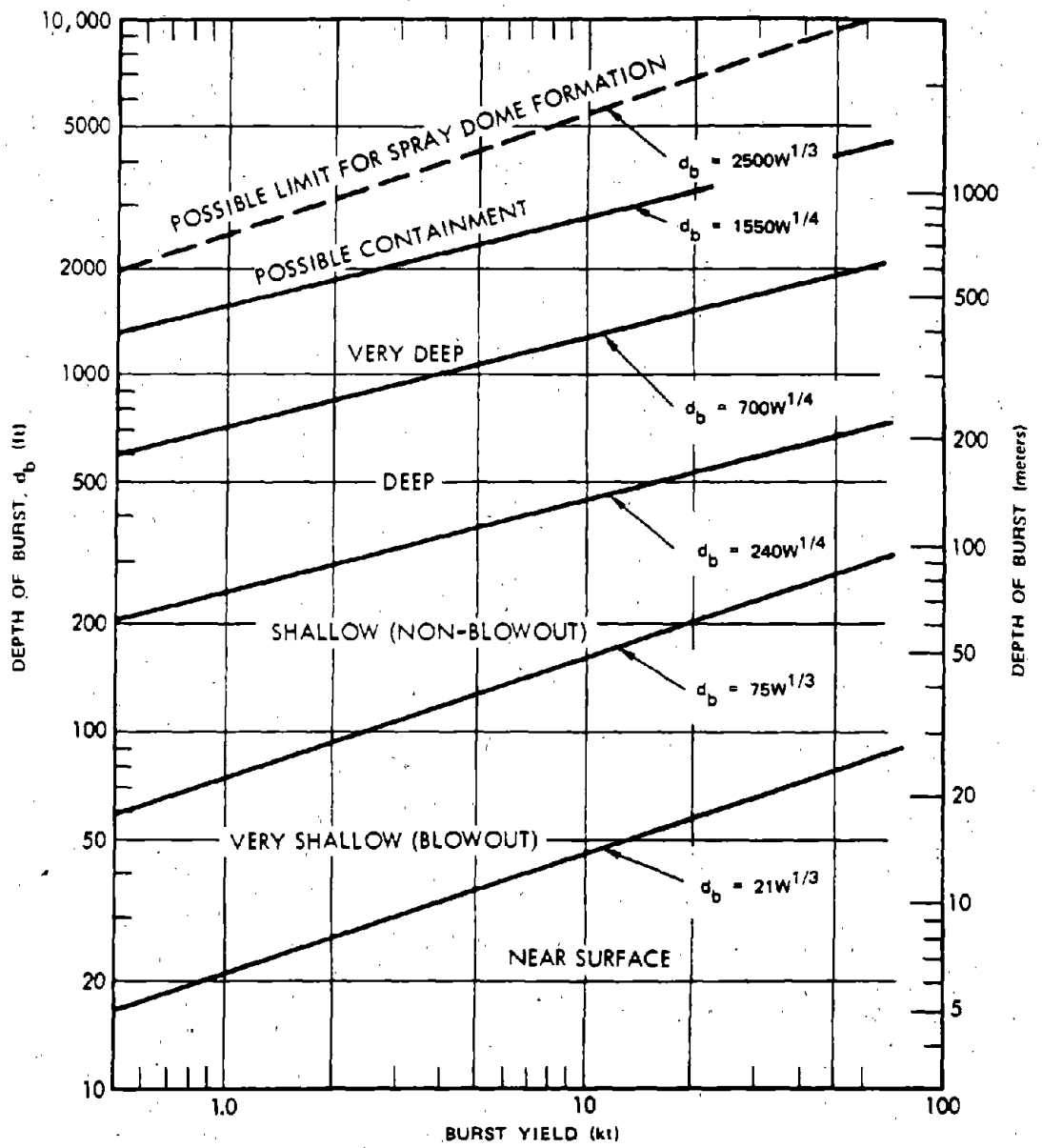


Figure 2-105. Classification of Underwater Nuclear Bursts

[REDACTED]

No radioactive debris would be observed on the surface from contained bursts. The probability of containment of the radioactive debris is a function of the oceanic density profile. The relation in Figure 2-105 probably is valid in certain tropical waters, but bursts at these same depths in northerly latitudes probably would not be contained.

No surface effects due to bubble pulsation or migration occur as a result of bursts that do not produce a spray dome.

Although water depths may also influence surface phenomena, and consequently burst classification, the mathematical definitions in Table 2-8 do not include this influence.

The various surface phenomena can be divided into two categories according to their origin, i.e., those produced by shock waves and those produced by the water motion accompanying bubble pulsation and rise. In the former category, the slick, crack, and spray dome are of operational importance. In the latter category, columns, plumes, base surge, and the long-lasting foam patch can be significant. More detailed descriptions of the surface phenomena are given in the following paragraphs.

2-73 Spray Dome [REDACTED]

The spray dome (or spall), is formed by the acceleration and breakup of the surface water layer. The initial surface velocity directly above the burst is the sum of the water particle velocities imparted by the incident and reflected waves; elsewhere, the initial velocity is approximately the sum of the vertical components of these velocities (some initial surface velocities have been observed to be higher than so calculated). The height of the spray dome is limited by deceleration of gravity and air drag.

If the depth of burst is sufficiently deep for one or more bubble oscillations to occur before venting, there may be secondary spray domes from reflection of compression waves

emitted by the later bubble expansions. These can be several times higher than the primary dome from very deep bursts.

The calculations of spray dome extent, vertical water velocity, and spray height are described in Problem 2-32. Plumes appear over the central portion of the spray dome from shallow bursts; therefore, a calculation of spray dome height may have little value.

2-74 Plumes, Column, Cauliflower Cloud [REDACTED]

If the burst is deep enough to prevent blowout (shallow to very deep bursts), expansion, pulsation, and rise of the bubble produce a violent upheaval and expansion of water above the surface to form plumes. In those deep explosions where the bubble collapses just beneath the surface, the rising bottom of the bubble jets through the layer of water above the bubble and probably will form a plume. In deep and very deep explosions, the upward motion of the water about the rising bubble also forms a plume.

The water displaced by the expanding bubble from very shallow bursts forms a dome-shaped shell of water over the bubble. Later, this shell ruptures and blows out the bubble constituents. For a very shallow nuclear explosion, blowout is accompanied by the formation of a "cauliflower cloud" at the top of the plume.

Since there are insufficient data for a comprehensive prediction technique, predictions of plumes, columns, and clouds are based on direct scaling from four nuclear bursts. Predictive relationships and examples of their use are given in Problem 2-33.

2-75 Base Surge [REDACTED]

As the plume from a deep burst or the column from a shallow burst falls back to the surface, it generates a cloud of fine spray, or aerosol, called "base surge," which usually is a

[REDACTED]

radiation hazard. The base surge expands and circulates as a toroidal cloud under the influence of the collapsing water plume. The expansion is rapid at first (exceeding 100 ft/sec); however, it decelerates upon mixing with the ambient air. During this period, part of the cloud evaporates and cools the air. As its kinetic energy dissipates and the cloud reaches its maximum diameter, it tends to thin out, and it may even become invisible as a consequence of diffusion and continued evaporation. In a sense, the base surge still exists, because some ocean salts and detonation products remain airborne.

[REDACTED] Two types of base surge have been encountered during weapon tests:

- "Doughnut-shaped" clouds from very shallow and shallow detonations
- "Disc-shaped" clouds or, more properly, a series of concentric "doughnut-shaped" clouds from deep and very deep detonations.

[REDACTED] Although visible configurations are actually quite irregular, the base surge configuration for very shallow and shallow detonations can be represented as a hollow cylinder or a hollow truncated cone for radiation exposure estimates. The inner diameter of the cylinder is approximately two-thirds the outer diameter. For very deep and deep bursts, a cylinder or truncated cone are adequate model configurations. The height of the visible base surge clouds at various weapon tests have varied between about 1,000 and 2,000 ft, probably as a result of turbulence and meteorological conditions.

[REDACTED] A base surge is transported by the wind during its formation and growth. As a general rule, the transport should depend upon the wind speeds at altitudes between the surface and the maximum surge height. The downwind growth curve may be predicted by adding the highest

wind speed reported between these levels to the average growth curves. The upwind growth should lie between a predicted curve based on subtracting half the surface wind speed (a rule-of-thumb to account for friction with the surface) and a curve obtained by subtracting the wind speed used for the downwind curve. At early times the former would be more accurate while at later times the latter would be more correct. Base surge prediction relationships and an example of their use are given in Problem 2-34.

2-76 Foam Patch and Ring [REDACTED]

[REDACTED] After subsidence of the plume, column, and base surge, a roughly circular area of disturbed water is still visible. This area is primarily defined by its white color and indications of turbulence at the perimeter. In the case of deep explosions, the patch can result from an upsurge of water caused by bubble migration. This water spreads out and then sinks, the overall motion being somewhat toroidal. Foam and flotsam tend to collect at the edge of the patch.

[REDACTED] The whiteness from deep shots is believed to be caused by foam generated by the agitation of the water, particularly as the plumes fall back. Similar foam patches occur from shallow detonations, but their whiteness is caused partly by suspended bottom material. The foam patch contains appreciable quantities of weapon debris and presents a potential radiation hazard to personnel in small boats or ships.

[REDACTED] The foam patches developing from test explosion have been on the order of 1.5 to 2.5 miles in diameter about 15 min after detonation, but they continued to expand slowly and irregularly with water currents and diffusion into the water, until the last visible manifestation was a ring of foam and debris. Their radioactivity could be traced for many days, although they had been invisible for quite some time.

[REDACTED]

WATER SURFACE WAVES

2-77 Generation and Propagation of Water Surface Waves

A submerged nuclear explosion, like any other physical event that produces a localized disturbance on the water surface, generates a group of surface waves that expand radially. The characteristics of explosively generated waves depend upon the yield, the depth of burst, and the range to the point of observation. If the water is sufficiently shallow, the bottom contour also can affect the generation and propagation of the waves.

The following physical description of the wave generation process and the succeeding prediction technique are based on:

- Laboratory experiments with small H.E. charges
- Wave data for the nine nuclear shots that have been fired on or in the lagoons at Eniwetok and Bikini, as listed in Table 2-9.
- Wave data for all the known tests in water with H.E. charges larger than 10 lb, as listed and referenced in Table 2-10.

Surface waves produced by an underwater explosion are generated by pulsations of the cavity formed at the surface when the oscillating bubble breaks through the surface (vents).

At a short range, within a few cavity radii, the first wave crest is so high and steep that it is unstable, and it spills forward turbulently and dissipates much of its energy. However, as the wave train expands and attenuates, the waves become shallow and smooth, their number increases, their energy remains nearly constant, and the highest wave appears successively later in the train. A wave gage record for such an expanded wave train is shown in Figure 2-106. The height H of the highest wave (trough-to-crest) decreases nearly inversely with range R ; but the length, speed, and period all remain

nearly constant for this peak wave, which is the one temporarily located at the first anti-node of the wave envelope as the waves move back in the envelope.

An approximate mathematical theory has been developed for shallow waves propagating from a shallow disturbance on the surface of water with constant depth. The results of this theory compare well with measured wave trains when a motionless "pseudo-cavity" is selected to approximate the wave generator or initial conditions. The "pseudo-cavity" is a shallow motionless depression of the water surface near the explosion. Its shape is derived empirically to correspond with the waves measured far from an explosion, but it does not necessarily correspond accurately with the actual shape of the water surface at any time.

All of the known measurements of peak wave height over deep water for charges greater than 10 lb are plotted in Figure 2-107. The vertical bars indicate the variation of HR for repeated shots and/or various gage ranges R . There is little discernible effect of depth of burst except near the "upper critical depth," where the H.E. charges were only partially submerged and where the peak wave height nearly doubled. Although current studies indicate that the upper critical depth effect may exist for nuclear as well as for H.E. charges, there is no firm evidence to support the inference as yet.

A plot comparable with Figure 2-107 of the data for H.E. charges smaller than 10 lb exhibits a pronounced upward hump in wave height versus depth of burst at $d_b \approx 3W_{HE}^{0.3}$ (and possibly also at $d_b \approx 8W_{HE}^{0.3}$). This increase in wave generation efficiency at the "lower critical depth" occurs when the expanding underwater cavity ruptures the layer of water above it (or vents) just before it becomes fully expanded. For large submerged explosions, the expanded bubble becomes tangent to the surface when the

Table 2-9. Measured Wave Data from Nuclear Tests

NUMBER SERIES SHOT	YIELD	WATER DEPTH AT CHARGE	DEPTH OF BURST	PEAK WAVE* HEIGHT x RANGE	CAVITY RADIUS	$d_w/100(W)^{1/4}$	$HR/2 \times 10^4 \sqrt{W}$
	W (kt) $100(W)^{1/4}$	d_w (ft)	d_b (ft)	$HR/2,000$ (ft) [†] min - max	R_c (ft)		min - max
1 HARDTACK UMBRELLA		140	140				
2 HARDTACK WAHOO		3,000	500				
3 CROSSROADS BAKER	23.5 220	180	90	36 - 60	1,000 [‡]	0.82 Shallow	0.74 - 1.24
4 WIGWAM	32 238	15,000	2,000	118	490 [‡]	63 Very Deep	2.08
5 REDWING FLATHEAD		120	0				
6 REDWING DAKOTA		140	0				
7 REDWING NAVAHO		230	0				
8 CASTLE UNION	7,000 916	145	7	232 - 312	1,000 [‡]	0.16 Shallow	0.16 - 0.28
9 CASTLE YANKEE	13,500 1,080	220	7	426 - 438	1,000 [‡]	0.20 Shallow	0.37 - 0.38

DNA
(2)(3)

*H is twice the measured height of the peak crest except for shots 8 and 9 where H is the measured height of the first crest from the following trough. H is corrected for uniform water depth = d_b by Green's law.

†Value deduced from measured surface wave train (Kaplan and Wallace, see bibliography) is a lower limit considerably smaller than actual values, which are unknown.

‡Measured values of the column radius (Young, DASA 1240-1(9)), see bibliography.

2-217
215

Table 2-10. Measured Wave Data from Large H.E. Tests

SHOT	YIELD	WATER DEPTH	DEPTH OF BURST	PEAK WAVE HEIGHT	CAVITY RADIUS	$d_w/100(W)^{1/4}$	$HR/2 \times 10^4 \sqrt{W}$
	W (kt)	d_w (ft)	d_b (ft)	HR/2 (ft) ²	R_c (ft)		min - max
WES Test Series at Lake Ouachita (from Pinkston and from Whalin)							
125 lb	0.625×10^{-4}	100	0 - 25	80 - 110		22.5	.90 - 1.24
385 lb	1.97×10^{-4}	100	0 - 36	147 - 225		17.0	1.25 - 1.91
WES Test Series at Mono Lake (1965 - 1966) (Preliminary data by private communication with R. Whalin and M. Pinkston and from Walter)							
1965 - 6	0.46×10^{-2} (9,200 lb)	130	0	1650 - 1900	68	5.2	2.4 - 2.8
- 2	↓	↓	.67	2100 - 3900	69	↓	3.1 - 5.7
- 4	↓	↓	1.04	2100 - 2850	71	↓	3.1 - 4.2
- 3	↓	↓	1.40	1750 - 3000	74	↓	2.6 - 4.4
-5, 7, 8, 9	↓	↓	9 - 51		61 - 80	↓	
1966 - 3	↓	≈130	5.2	1150 - 1250		↓	1.7 - 1.8
- 2	↓	↓	23	850 - 1200		↓	1.2 - 1.8
- 1	↓	↓	60	1300 - 1400		↓	1.9 - 2.1
HYDRA 11a (Van Dorn) W = 10 ⁴ lb HBX							
- 7	0.723×10^{-2} (14,450 lb)	300	140	1650 - 1970		10.3	1.94 - 2.31
- 8	↓	↓	80	975 - 1340		↓	1.15 - 1.55
- 9	↓	↓	35.5	1260 - 1590		↓	1.48 - 1.87
- 10	↓	↓	7.1	1610		↓	1.88
- 11	↓	↓	15.9	1510 - 1840		↓	1.77 - 2.16
- 12	↓	↓	15.9	1490		↓	1.75
- 13	↓	↓	17.7	1450		↓	1.71

2-218
37/

[REDACTED]

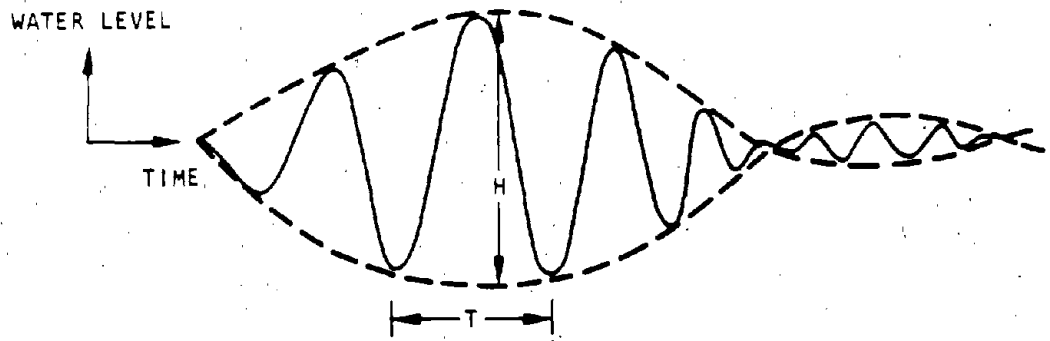


Figure 2-106. [REDACTED] Wave Gage Record for an Explosion-Generated Wave Train [REDACTED]

[REDACTED]

247
2-210
[REDACTED]

248
2-250



Deleted



Figure 2-107. Peak Wave Height vs Depth of Burst for Shots in Deep Water



DNA
(4)(3)



burst depth d_b equals $240W^{1/4}$. The lower critical depth is somewhat smaller at about $d_b = 170W^{1/4}$. However, the effect on wave generation is much smaller for the larger charges in Figure 2-107, and the height of the peak wave generated by large explosions in "deep" water can be approximated simply by

$$HR/W_{HE}^{0.54} = 16 \pm 4,$$

where H is the amplitude of the maximum of the first envelope trough-to-crest in feet, R is the radial distance from the explosion in feet, and W_{HE} is the charge weight in equivalent pounds of TNT. An equivalent approximation is

$$HR = 40,500 (W)^{0.54} \pm 25 \text{ percent},$$

where W is the yield in kilotons and the other symbols are as defined above. Similarly, the length and period of the peak wave can be approximated by

$$L = 15.5 (W_{HE})^{0.288} \text{ ft.}$$

$$T = 1.74 (W_{HE})^{0.144} \text{ sec.}$$

These three relationships were derived empirically from test data for 125- and 385-lb H.E. charges and the two nuclear explosions shown in Figure 2-107. For a pseudo-cavity of a given shape, which has a potential (gravitational) energy comprising a fixed fraction of the explosive yield, all the dimensions of the cavity and the wave train are proportional to $W_{HE}^{1/4}$ or $W^{1/4}$ (Froude scaling), and the exponents in the three equations given above are 1/2, 1/4, and 1/8, respectively. Since the empirical exponent in the first equation was found to be 0.62 for small H.E. charges, it seems reasonable to suppose that the "theoretical" value of 1/2 may be the best

value to use for extrapolation to large yields (the high kiloton and megaton range). With this exponent, the data in Figure 2-107 have been replotted as a function of reduced water depth (rather than charge depth) for use in Problem 2-35 (Figure 2-128).

The horizontal line in Figure 2-128 can be used to predict the peak wave height in deep water. However, it can be derived by the following simple procedure to illustrate qualitatively the physical process of wave generation in "deep" water to define "deep." The approximation is made that an explosion in deep water at any depth of burst above the lower critical depth generates a parabolic (nearly hemispherical) cavity upon venting, and that the potential energy of this cavity E_c is equal to 5 percent of the explosive yield E_o . That is:

$$\begin{aligned} E_c &= \frac{\pi}{6} \rho_w g R_c^4 = 0.05E_o \\ &= 0.05 \times 2.86 \times 10^{12} W \text{ ft-lb.} \end{aligned}$$

This gives the following cavity radius, which is taken equal to the cavity depth and the radius of the plume (or column) of water projected upward:

$$R_c = 256 (W)^{1/4} \text{ ft.}$$

$$\text{if } d_w \geq R_c,$$

and if the density of seawater and the hydrodynamic yield of the explosion are taken as

$$\rho_w g = 65 \frac{\text{lb}}{\text{ft}^3}, \text{ and } e_o = 1,025 \frac{\text{cal}}{\text{gm}}$$

This cavity radius is not much larger than the bubble radius and depth of burst corresponding to the lower critical depth. The restriction on

[REDACTED]

water depth d_w in the equation for R_c is taken as the minimum water depth that can be considered "deep" i.e., the depth for which the assumed cavity shape touches bottom as it vents.

The dissipative effects close to the cavity are approximated by the assumption that the leading peak wave crest spills forward and breaks turbulently at $R = 2R_c$ to the limiting height of a wave that can propagate in a stable manner over deep water (the Michell limit, or $H_{max} = 0.14L$). Finally it is assumed that the amplitude of the wave envelope H is attenuated inversely with range R as it continues to expand without dissipation. This gives the "predicted" peak wave height when the water depth at the charge location is "deep" ($d_w \geq 256W^{1/4}$) as

$$HR = 49,000 \sqrt{W},$$

which corresponds to the horizontal line in Figure 2-128. This "predicted" value can be used for depths of burst ranging from zero to at least five times the lower critical depth (at $d = 170W^{1/4}$) judging by the comparison with WIG-WAM data, even though the cavity radius becomes too large for depths of burst much below the lower critical depth.

The line in Figure 2-128 can be extended into "shallow" water by a comparable simple procedure. In shallow water the cavity both touches bottom and vents to the atmosphere early during its expansion. Hence, much less work is done on the water by the expanding gaseous bubble, and much less energy is propagated as water surface waves over shallow water. Experimental data indicate that explosions in shallow water generate a dry cavity surrounded by a nearly vertical wall of water which extends upward as a thin lip to form the "column." A lower limit for the maximum radius of this cavity (or column) is given by the following relationship, which was derived from the energy calculated from measured wave trains

over shallow water (Table 2-9) and which will be discussed in succeeding paragraphs.

$$R_c = 100 (W)^{1/4} \text{ if } d_w \leq R_c$$

Once again, the dissipative effects close to the cavity are approximated by the assumption that the leading peak wave breaks down to the limiting height of a stable progressive wave, but, for shallow water, the approximation is that $H_{max} = (3/4) d_w = \text{Miche limit at } R = 2R_c$. If this peak wave height is then attenuated inversely with range R , the "predicted" peak wave height when the water depth at the charge location is "shallow," ($d_w \leq 100W^{1/4}$), becomes

$$HR = 150 d_w W^{1/4},$$

which gives the line with the 45 degree slope in Figure 2-128. This "prediction" can be used for any depth of burst ($0 < d_b \leq d_w$) as shown by measured data for H.E. charges in shallow water. As shown in Figure 2-128, there is much scatter in the nuclear wave data in shallow water and some of the measured peak wave heights are more than twice as large as "predicted" by the foregoing equation, which should be regarded only as a rough rule-of-thumb for correlating the measured data in Figure 2-128.

The only actual measured data for the radii of the water columns (or cavities) for nuclear bursts near the surface of water are for shots BAKER and UMBRELLA (Table 2-9). These values of R_c and those measured for submerged H.E. explosives are roughly equal to the value given by the equation for maximum bubble radius in paragraph 2-67, which gives a burst estimate for R_c .

DNA
K(3)

250
2-228

[REDACTED]

[REDACTED]

DWA
(K)(3)

In soil, TNT charges detonated at the surface generate crater radii approximately twice as large as nuclear explosions of the same yield, so the nuclear-TNT equivalence is only about 10 percent. The column radii observed for TNT detonations near the surface of the water are roughly equal to $470W^{1/3}$, which is the bubble radius given by the equation in paragraph 2-67 for a surface burst. This occurs even when the bubble radii exceed the water depth by a factor of 5. Therefore, it might be expected that a nuclear burst at the surface of water would produce a column radius about half as large as the H.E. value, or $240W^{1/3}$. This latter value is much larger than the lower limit estimated above ($R_c = 100W^{1/4}$). This lower limit is also exceeded by the crater radii measured in the bottom after explosions in shallow water, and the water column radii probably exceed the crater radii. Although there are no substantiating data, nuclear explosions at the surface of water of any depth probably generate water columns with radii between $100W^{1/4}$ and $240W^{1/3}$ feet.

2-78 Refraction and Shoaling

Explosion-generated waves, in common with wind waves and tsunami (earthquake-generated) waves, are affected by changes in the depth over which they propagate. As the waves move into water shallower than about one-third their length (or shoal), their period remains fixed, but both their speed and their length decrease (between successive crests) and their height first decreases about 10 percent and then begins to increase. Because of the change in speed, a wave bends or refracts if it moves into shallow water at an angle to the bottom contours. Refraction can increase or decrease the localized wave height, depending on the hydrography over which the wave moves. No general

methods for determining refraction effects are given here; however, such techniques for calculating these effects are available ("Oceanographical Engineering," R. L. Wiegel, see bibliography).

The increase in height of a wave relative to its length (steepening) continues until the wave becomes unstable and breaks, unless the bottom slope is so shallow that bottom friction dissipates the wave before it breaks. In shallow water without dissipation, steepening increases the wave height as the inverse fourth root of the water depth. Many types of waves become unstable and break (or spill) when their height exceeds either 75 percent of the water depth (the Miche limit) or 14 percent of the wave length over deep water (the Michell limit) as described by Weigel (see bibliography).

UNDERWATER CRATERING

If an explosion occurs in or even close to a layer of water overlaying bottom material, a significant crater forms in the bottom material whenever the gaseous bubble or water cavity formed by the explosion contacts the bottom. An underwater crater is similar to an onshore crater formed by an explosion near the ground since both are characterized by a dish-shaped depression, wider than it is deep, and surrounded by a lip raised above the undisturbed surface. In the case of most underwater craters, however, the observed ratio of crater radius to depth is larger and the lip height is smaller than for craters from comparable bursts in similar bottom materials onshore. These differences are caused by water displaced by the explosion washing back over the crater. This flow increases the crater radius by as much as 10 percent and decreases the crater depth by as much as 30 percent. An exception to this general rule occurs when the water layer is so shallow that the lip formed by the initial cratering extends above the surface of the water. Such craters (termed "un-

251
2-282

[REDACTED]

[REDACTED] washed craters") approach onshore craters in appearance, with higher lips and larger depth-to-radius ratios than washed craters. This section describes only the crater characteristics directly related to the explosion. The effects of tidal currents and the collapse of unwashed crater lips by hydrostatic forces are not considered.

[REDACTED] The characteristics of underwater craters can be predicted at least qualitatively from the depth of burst, water depth, bottom composition, and weapon yield. The use of empirical curves relating the depth and radius of the crater for surface and bottom bursts over a clayey-sand bottom is described in Problem 2-36. Predictions for other bottom materials can be made by ap-

plying tabulated factors to the values predicted for clayey sand, as described in Problem 2-36. It is evident that larger craters are produced by moving the charge toward the bottom; increasing the water depth above a bottom burst (up to a point); or decreasing the water depth beneath a surface burst.

[REDACTED] A very large yield is required to form an unwashed crater in water having a depth that is common to most harbors. For example, with 30 ft of water over clayey-sand, 4 Mt would be required on the bottom to produce a dry crater lip. It is quite unlikely that materials that tend to flow, such as oceanic ooze or fine-grained silt, could support the hydrostatic pressure exerted on a dry crater lip.

252
2-224

[REDACTED]

[REDACTED]

**Problem 2-28. Calculations of Underwater
Explosion Phenomena**

Calculations can be performed to determine bubble characteristics described in paragraph 2-67. The characteristics include the maximum radii, bubble periods, and migration between maxima for events to the end of the second bubble period. The calculation methods do not apply to cases where the bubble touches the bottom, and the methods contain uncertainties not yet fully resolved when the bubble center is very close to or above the surface. Furthermore, predictions that are made for events increasingly removed in time from the first maximum have increasing uncertainty. Two methods for calculating these bubble characteristics are demonstrated in the example. The first method uses the equations given in paragraph 2-67 and Figures 2-108 through 2-110. The second method uses equations introduced in the example and Figure 2-111. The first method is graphical and is less accurate than the second, but it provides a quick estimate.

Example

Given: 32 kt fired at a depth of 2,000 ft in very deep water.

Find:

- a. The initial bubble period and radius,
- b. The depth of the second maximum radius,
- c. The second bubble period,
- d. The radius at second maximum,
- e. The depth of third maximum radius,
- f. The third bubble period and radius at third maximum.

Solution (Method 1):

- a. Calculate the initial radius A_1 and the period T_1 , by using equations given in paragraph 2-67:

$$A_1 = J' \frac{W^{1/3}}{Z^{1/3}}$$

$$A_1 = (1,500) \left(\frac{(32)^{1/3}}{(2,000 + 33)^{1/3}} \right) = 376 \text{ ft.}$$

$$T_1 = K' \frac{W^{1/3}}{Z^{5/6}}$$

$$T_1 = (515) \left(\frac{(32)^{1/3}}{(2,033)^{5/6}} \right) = 2.86 \text{ sec.}$$

- b. Find the reduced hydrostatic head:

$$\frac{Z_1}{A_1} = \frac{2,033}{376} = 5.41.$$

From Figure 2-108, for $n = 1$,

$$\frac{\Delta Z_1}{Z_1} = 0.28,$$

$$\Delta Z_1 = (0.28)(2,033) = 569 \text{ ft (migration during first period),}$$

$$d_2 = d_b - \Delta Z_1,$$

$$d_2 = 2,000 - 569 = 1,431 \text{ ft.*}$$

* Note that results are sensitive to graph readings.

c. From Figure 2-109, for $n = 2$,

$$T_2 = 0.90 T_1,$$

$$T_2 = (0.90)(2.86) = 2.57 \text{ sec.}$$

d. From Figure 2-110, for $n = 2$,

$$A_2 = 0.77 A_1 = (0.77)(376) = 290 \text{ ft.}$$

e. From Figure 2-108, using $Z_1/A_1 = 5.41$ and $n = 2$,

$$\frac{\Delta Z_2}{Z_1} = 0.23,$$

$$\Delta Z_2 = 0.23 Z_1 = (0.23)(2,033) = 468 \text{ ft.}$$

$$d_3 = d_2 - \Delta Z_2,$$

$$d_3 = 1,431 - 468 = 963 \text{ ft.}$$

f. From Figure 2-109, for $n = 3$,

$$T_3 = 0.66 T_1,$$

$$T_3 = (0.66)(2.86) = 1.89 \text{ sec.}$$

From Figure 2-110, for $n = 3$,

$$\frac{A_3}{A_1} = 0.47,$$

$$A_3 = 0.47 A_1 = (0.47)(376) = 177 \text{ ft.}$$

Solution (Method 2): This method uses Figure 2-111 to obtain values for bubble energy ratio, r_n/r_{n-1} , and the following reduced equations:

2-226
254

$$\left(\frac{\Delta Z_n}{Z_n}\right) = 3.5 \left(\frac{A_1}{Z_1}\right)^{3/2} \left(\frac{r_n}{r_1}\right)^{1/2} \left(\frac{Z_1}{Z_n}\right)^2,$$

$$\left(\frac{A_n}{A_1}\right) = \left(\frac{Z_1}{Z_n}\right)^{1/3} \left(\frac{r_n}{r_1}\right)^{1/3},$$

$$\left(\frac{T_n}{T_1}\right) = \left(\frac{Z_1}{Z_n}\right)^{5/6} \left(\frac{r_n}{r_1}\right)^{1/3}.$$

a. By the same procedures used in Method 1,

$$A_1 = 376 \text{ ft.}$$

$$T_1 = 2.86 \text{ sec.}$$

b. Using the first reduced equation given above,

$$\left(\frac{\Delta Z_1}{Z_1}\right) = 3.5 \left(\frac{A_1}{Z_1}\right)^{3/2} \left(\frac{r_1}{r_1}\right)^{1/2} \left(\frac{Z_1}{Z_1}\right)^2,$$

$$\left(\frac{\Delta Z_1}{Z_1}\right) = 3.5 \left(\frac{375}{2,033}\right)^{3/2} (1)^{1/2} (1)^2 = 0.277,$$

$$\Delta Z_1 = 0.277 Z_1,$$

$$\Delta Z_1 = (0.277)(2,033) = 564,$$

$$d_2 = d_b - \Delta Z_1,$$

$$d_2 = 2,000 - 564 = 1,436 \text{ ft.}$$

c. The second bubble period T_2 can be obtained from the third reduced equation given above, and T_1 from (a) after finding the energy

ratio between the first and second bubbles. Using the reduced migration $\Delta Z_1/Z_1 = 0.277$ to enter Figure 2-111, the energy ratio is $r_2/r_1 = 0.324$. Thus,

$$\left(\frac{T_2}{T_1}\right) = \left(\frac{Z_1}{Z_2}\right)^{5/6} \left(\frac{r_2}{r_1}\right)^{1/3}$$

$$\left(\frac{T_2}{T_1}\right) = \left(\frac{2,033}{1,469}\right)^{5/6} (0.324)^{1/3}$$

$$\frac{T_2}{T_1} = 0.90,$$

$$T_2 = (0.90)(2.86) = 2.57 \text{ sec.}$$

d. The radius of the second maximum is obtained from the second reduced equation given above.

$$\left(\frac{A_2}{A_1}\right) = \left(\frac{Z_1}{Z_2}\right)^{1/3} \left(\frac{r_2}{r_1}\right)^{1/3}$$

$$\left(\frac{A_2}{A_1}\right) = \left(\frac{2,033}{1,469}\right)^{1/3} (0.324)^{1/3},$$

$$\left(\frac{A_2}{A_1}\right) = 0.765,$$

$$A_2 = 0.765 A_1 = (0.765)(376) = 288 \text{ ft.}$$

e. To calculate the depth of the third maximum, it is first necessary to find the reduced migration $\Delta Z_2/Z_2$. From the first reduced equation,

$$\left(\frac{\Delta Z_2}{Z_2}\right) = 3.5 \left(\frac{A_1}{Z_1}\right)^{3/2} \left(\frac{r_2}{r_1}\right)^{1/2} \left(\frac{Z_1}{Z_2}\right)^2$$

$$\left(\frac{\Delta Z_2}{Z_2}\right) = 3.5 \left(\frac{376}{2,033}\right)^{3/2} (0.324)^{1/2} \left(\frac{2,033}{1,469}\right)^2$$

$$\left(\frac{\Delta Z_2}{Z_2}\right) = 0.303,$$

$$\Delta Z_2 = 0.303 Z_2 = (0.303)(1,469) = 445 \text{ ft.}$$

$$d_3 = d_2 - \Delta Z_2,$$

$$d_3 = 1,436 - 445 = 991 \text{ ft.}$$

f. From c., $r_2/r_1 = 0.324$. Using the reduced migration $\Delta Z_2/Z_2 = 0.303$ to enter Figure 2-111, the energy ratio $r_3/r_2 = 0.158$.

$$\left(\frac{r_3}{r_1}\right) = \left(\frac{r_2}{r_1}\right) \left(\frac{r_3}{r_2}\right)$$

$$\left(\frac{r_3}{r_1}\right) = (0.324)(0.158) = 0.0512.$$

From the third reduced equation

$$\left(\frac{T_3}{T_1}\right) = \left(\frac{Z_1}{Z_3}\right)^{5/6} \left(\frac{r_3}{r_1}\right)^{1/3}$$

$$\left(\frac{T_3}{T_1}\right) = \left(\frac{2,033}{1,024}\right)^{5/6} (0.0512)^{1/3} = 0.658,$$

$$T_3 = 0.658 T_1$$

$$T_3 = (0.658)(2.86) = 1.88 \text{ sec.}$$

From the second reduced equation,

$$\left(\frac{A_3}{A_1}\right) = \left(\frac{Z_1}{Z_3}\right)^{1/3} \left(\frac{r_3}{r_1}\right)^{1/3}$$

$$\left(\frac{A_3}{A_1}\right) = \left(\frac{2,033}{1,024}\right)^{1/3} (0.0512)^{1/3} = 0.467$$

$$A_3 = 0.467 A_1$$

$$A_3 = (0.467)(376) = 176 \text{ ft.}$$

Answer:

	<i>Method 1</i>	<i>Method 2</i>
--	-----------------	-----------------

- | | | |
|---|--|--|
| a. The initial
bubble period
and radius | $A_1 = 376 \text{ ft}$
$T_1 = 2.86 \text{ sec}$ | 376 ft
2.86 sec |
| b. The depth of
the second
maximum radius | $d_2 = 1,431 \text{ ft}$ | $1,436 \text{ ft}$ |

- | | | |
|---|--|--|
| c. The second
bubble period | $T_2 = 2.57 \text{ sec}$ | 2.57 sec |
| d. The radius at
second maximum | $A_2 = 290 \text{ ft}$ | 288 ft |
| e. The depth of
third maximum
radius | $d_3 = 963 \text{ ft}$ | 991 ft |
| f. The third
bubble period
and radius at
third maximum | $T_3 = 1.89 \text{ sec}$
$A_3 = 177 \text{ ft}$ | 1.88 sec
176 ft |

Reliability: The uncertainty in the values for maximum radii calculated by the methods described above are about +20 percent and -35 percent, based on very limited information.

Related Material: See paragraph 2-67.

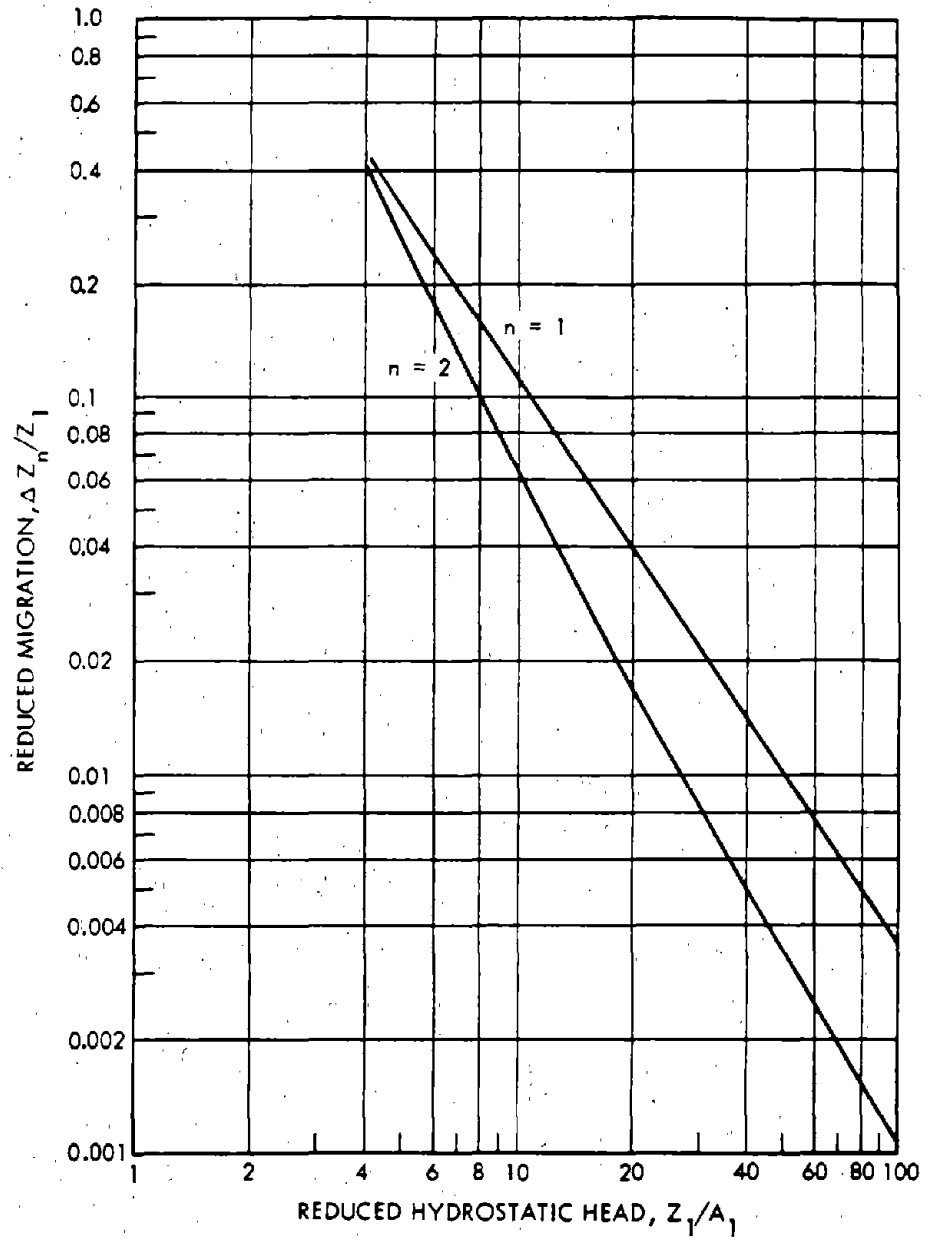


Figure 2-108. Reduced Nuclear Bubble Migration

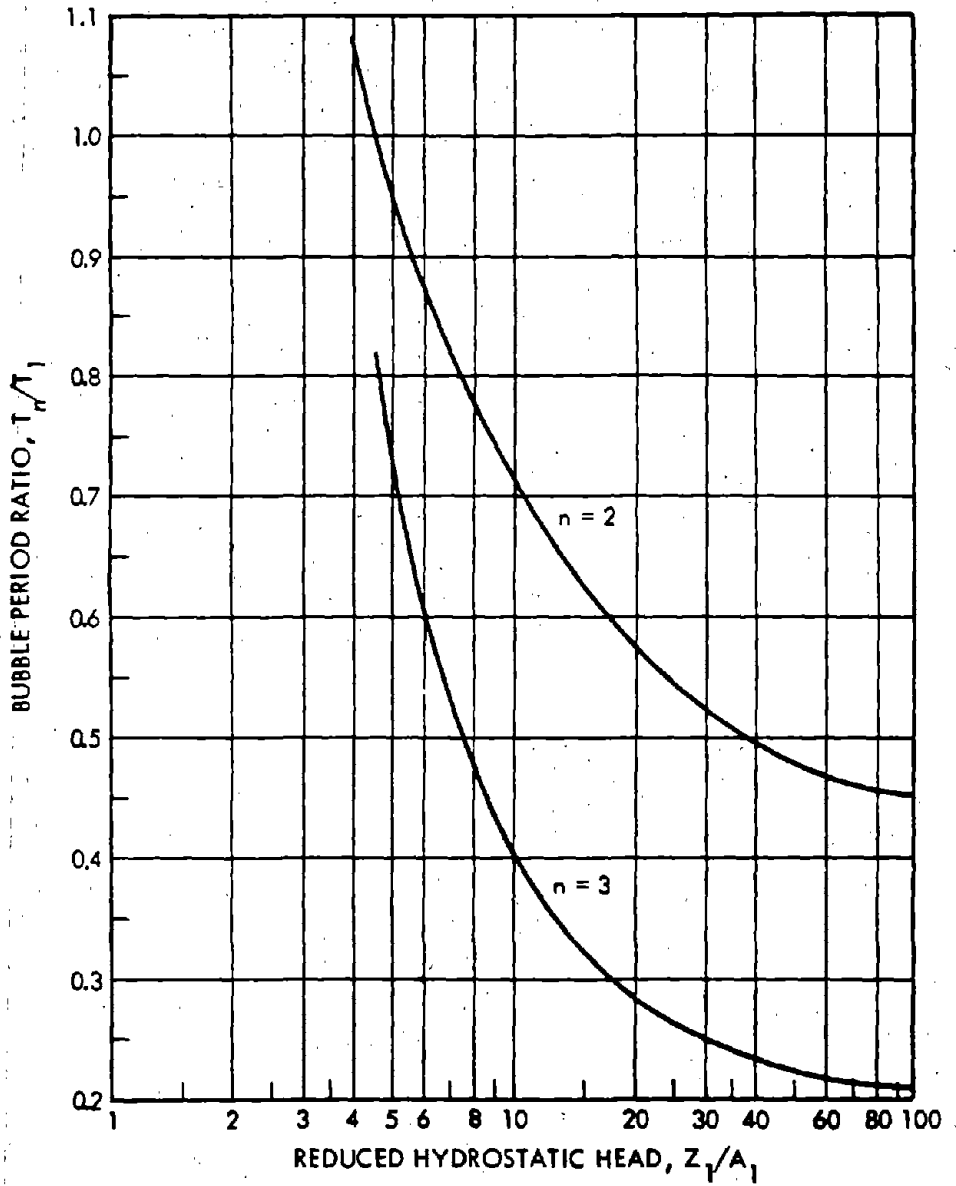


Figure 2-109. Successive Nuclear Bubble Period Ratios

2-238-
258

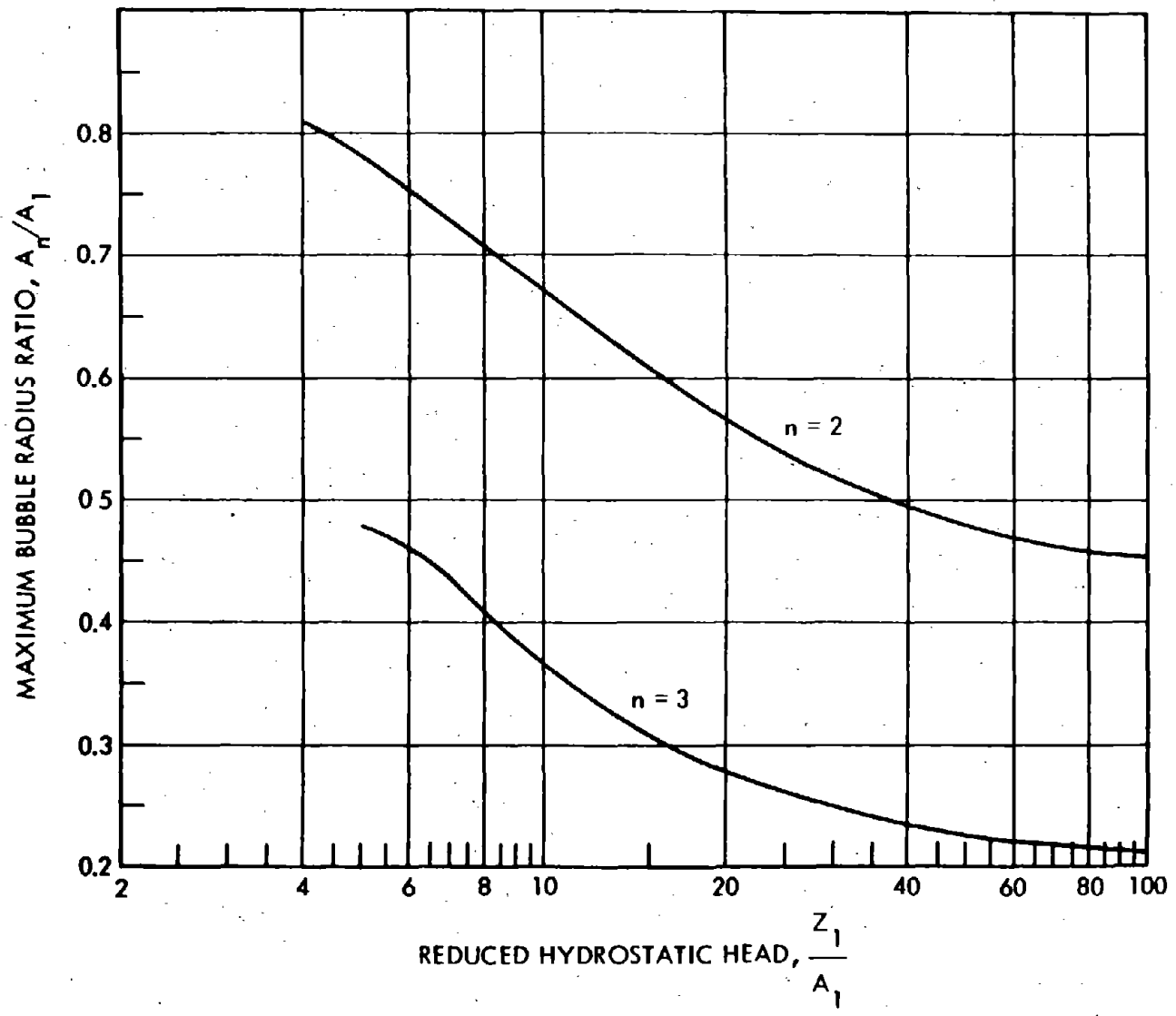


Figure 2-110. Successive Nuclear Maximum Bubble Radius Ratios

2-294
259

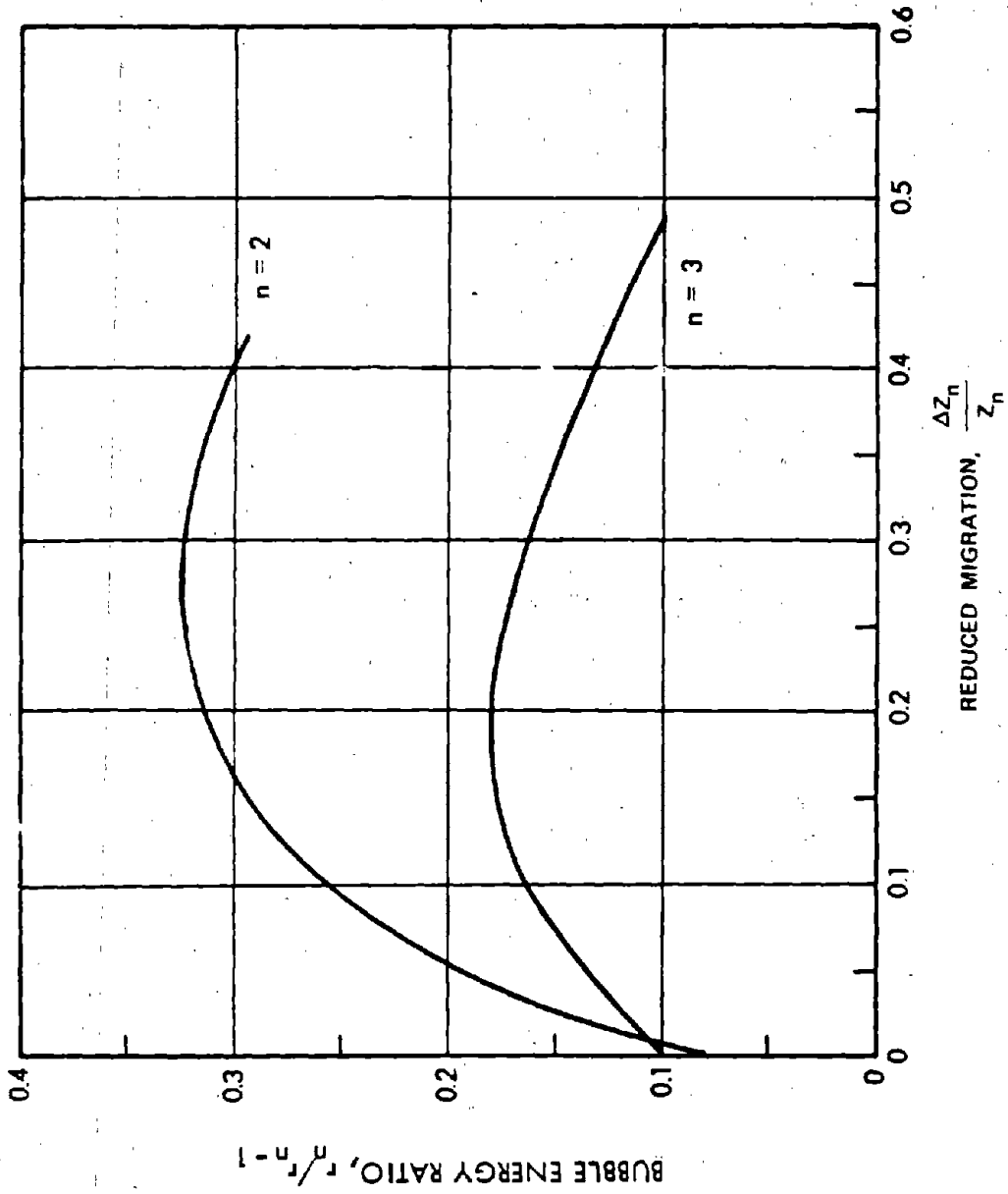


Figure 2-111. Nuclear Bubble Energy Ratios

2-788
2-789

**Problem 2-29. Calculation of Shock Wave Parameters
for Free Water (Deep Bursts)**

Figures 2-112 through 2-116 show the parameters for the primary shock wave from an underwater explosion in free, isovelocity water (no reflections, no refractions). Figure 2-112 shows the peak pressure as a function of slant range for various yields, where the peak pressure is lower than 3,000 psi, and as a function of reduced slant range ($R/W^{1/3}$) for peak pressures above 3,000 psi. Figure 2-113 shows the shock wave impulse as a function of slant range for various yields, while Figure 2-114 shows the shock wave energy flux as a function of slant range for the same yields. These latter two families of curves show values of impulse and energy flux integrated to a time of 6.7θ , where θ is the time constant for the shock wave, which is defined as the time for the shock wave pressure to fall to approximately 37 percent of its peak value.

The time constant θ is shown in Figure 2-115 as a function of slant range for the same family of yields shown in Figures 2-113 and 2-114. Figure 2-116 shows a dimensionless pressure-time curve. Using values of θ from Figure 2-115 and values of p_m from Figure 2-112, Figure 2-116 may be used to construct the pressure-time shape of the shock wave in free water at various ranges from underwater explosions of various yields.

Scaling. For yields other than those shown in Figure 2-112 through 2-115, use linear interpolation between appropriate curves.

Example

Given: A 50 kt burst at a depth of 1,000 ft in deep water.

Find: The peak shock pressure p_m , the shock wave impulse I , energy flux E , and time constant θ at a 1,000 ft depth, 4,000 yd from

the burst.

Solution: The desired shock wave parameters can be read directly from Figures 2-112 through 2-115.

Answer:

$$p_m \approx 470 \text{ psi.}$$

$$I \approx 28 \text{ psi-sec.}$$

$$E \approx 10^3 \text{ in.-lb/in.}^2,$$

$$\theta \approx 50 \text{ msec.}$$

Reliability: Values shown in Figures 2-112 through 2-115 are estimated to be accurate within ± 10 percent for shock pressure, and ± 20 percent for the other parameters for yields between 1 kt and 1 Mt. For yields below 1 kt or above 1 Mt, the values are more uncertain. The assumption of isovelocity water becomes increasingly uncertain for ranges beyond a few kiloyards in the ocean.

Related Material:


See paragraphs 2-68 through 2-72.

Figures 2-112 through 2-115 are based on the following equations:

$$p_m = 4.38 \times 10^6 \left(\frac{W^{1/3}}{R} \right)^{1.13} \text{ psi}$$

$$I \text{ (to } 6.7\theta) = 1.176 \times 10^4 W^{1/3} \left(\frac{W^{1/3}}{R} \right)^{0.91} \text{ psi-sec}$$

$$E \text{ (to } 6.7\theta) = 3.976 \times 10^9 W^{1/3} \left(\frac{W^{1/3}}{R} \right)^{2.04} \frac{\text{in.-lb}}{\text{in.}^2}$$


$$\theta = 2.274 W^{1/3} \left(\frac{W^{1/3}}{R} \right)^{-0.22} \text{ msec.}$$

The values of these parameters are related to those for TNT (Cole, 1948) by an ap-

proximate equivalence factor. Snay and Butler (1957) (see bibliography) report that an underwater nuclear burst with a radiochemical yield of 1 kt gives approximately the same shock wave parameters at the same distance as a TNT charge weighing 0.67 kiloton (where 1 ton = 2,000 lbs).

2-734
262



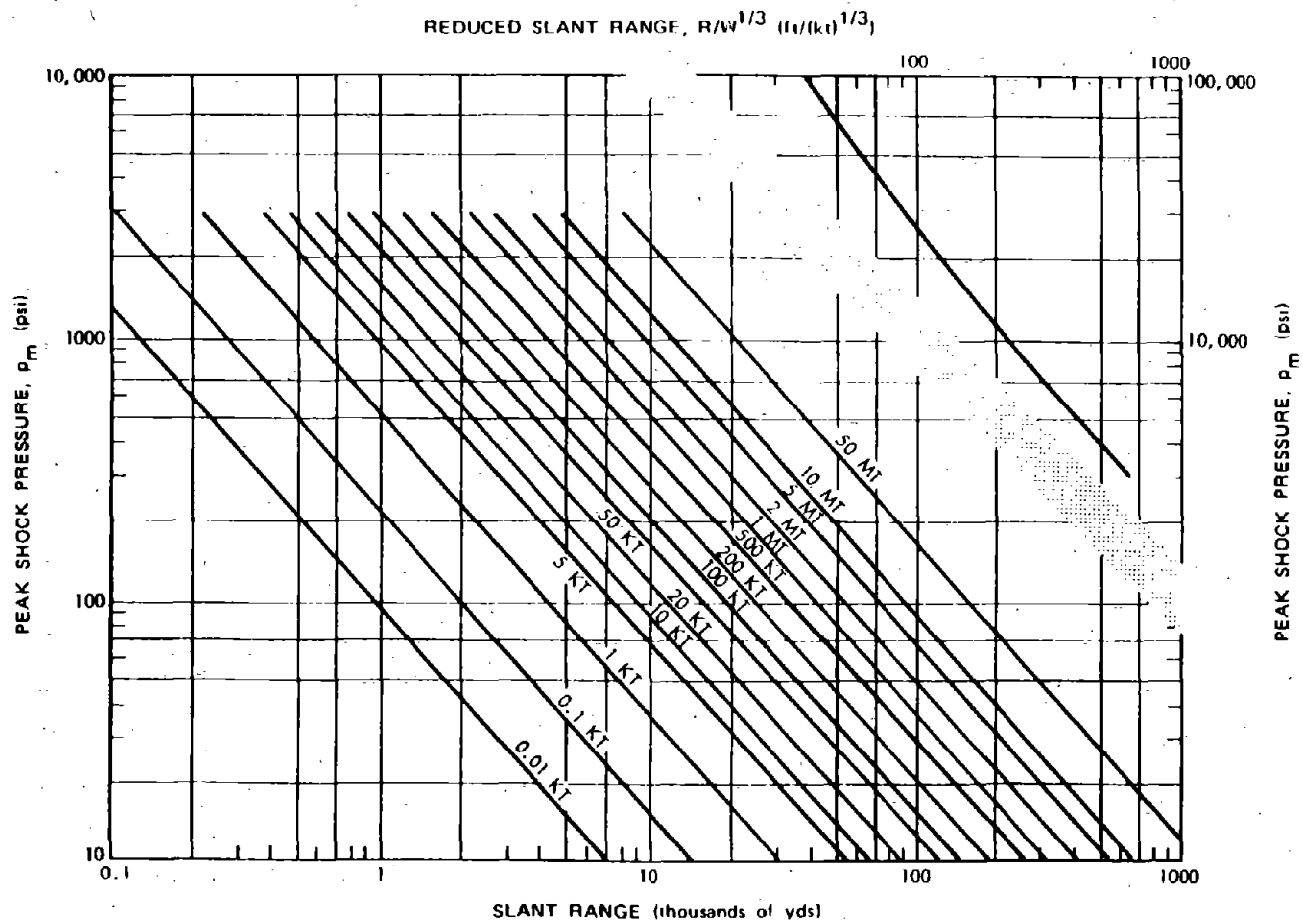


Figure 2-112. Shock Wave Peak Pressure in Free Isovelocity Water

2-288
273

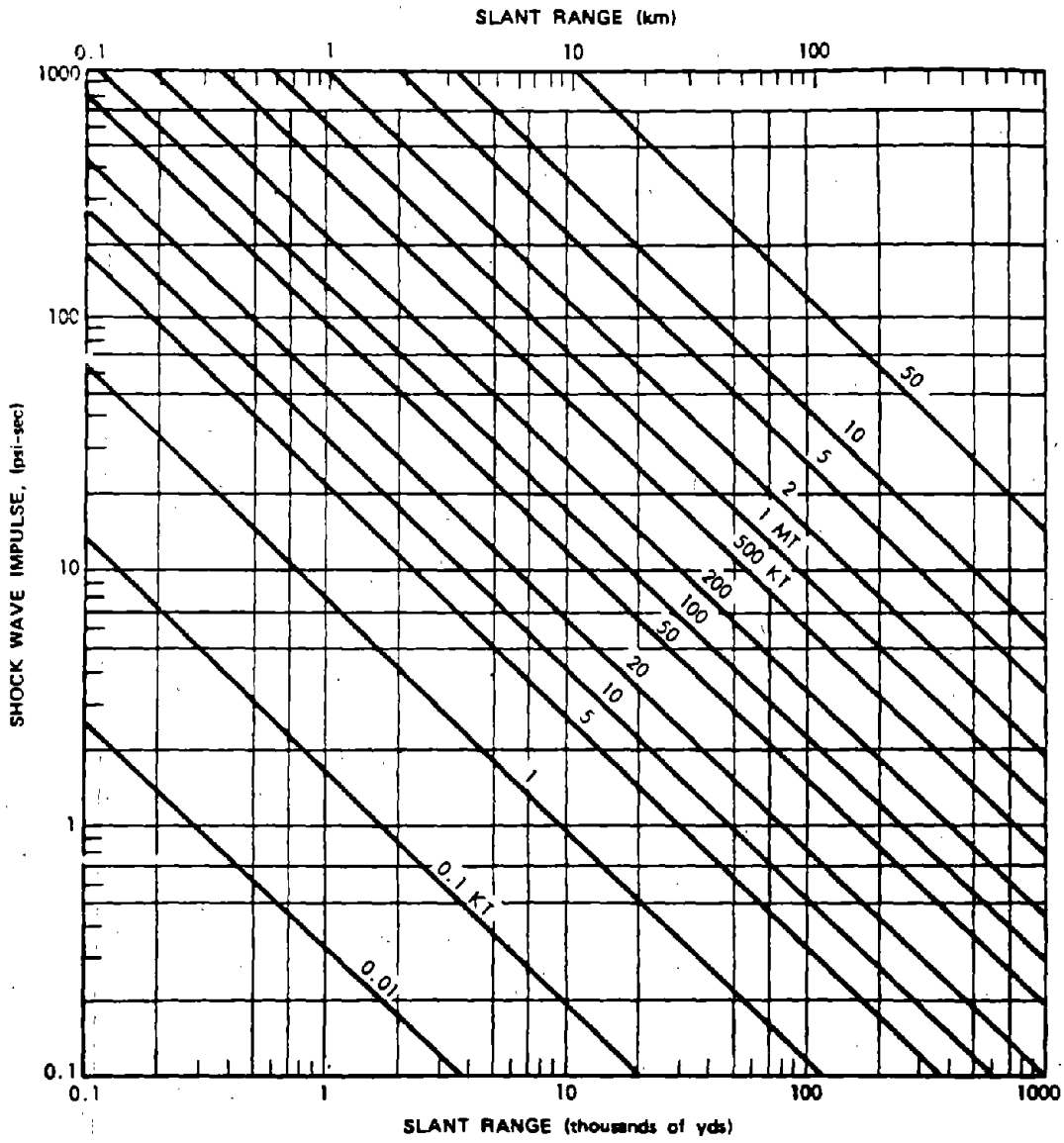


Figure 2-113. Shock Wave Impulse vs Slant Range in Free Isovelocity Water

2-236
264

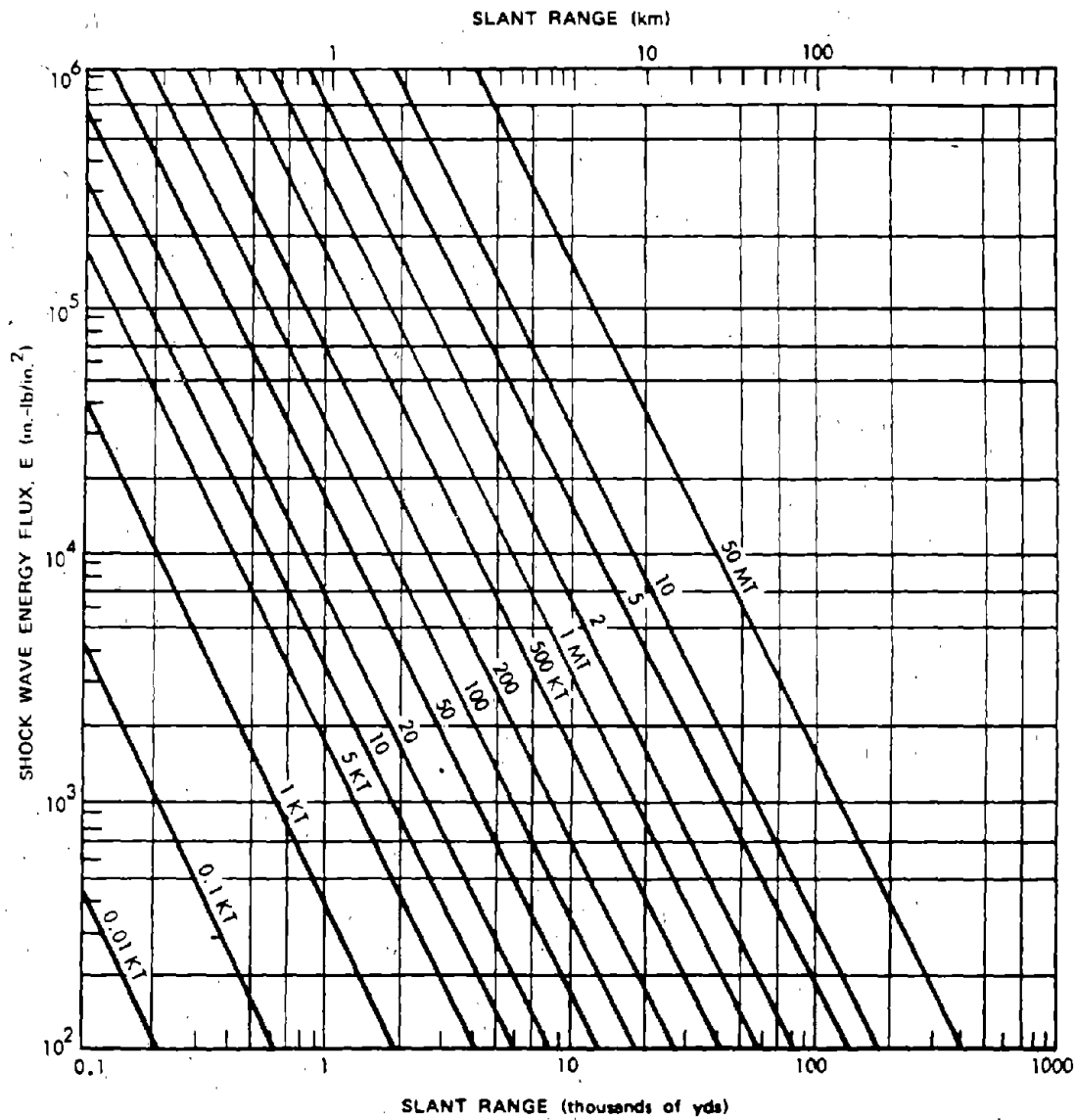


Figure 2-114. Shock Wave Energy Flux vs Slant Range in Free Isovelocity Water

2-282
265

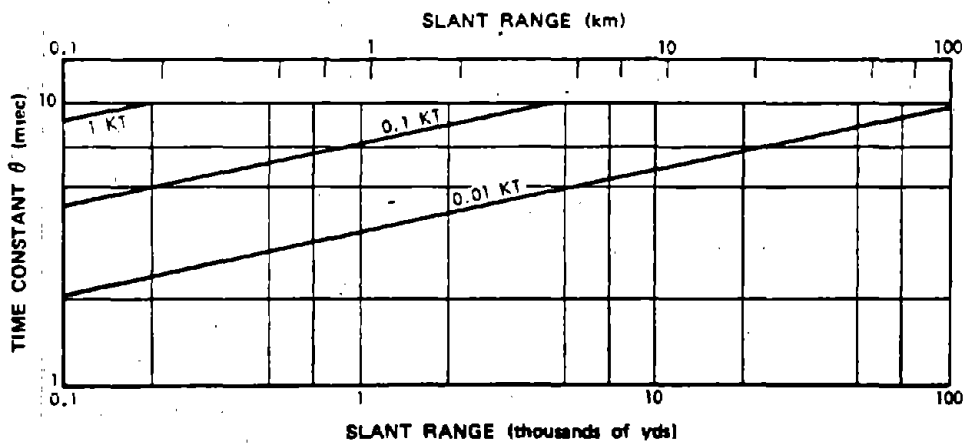
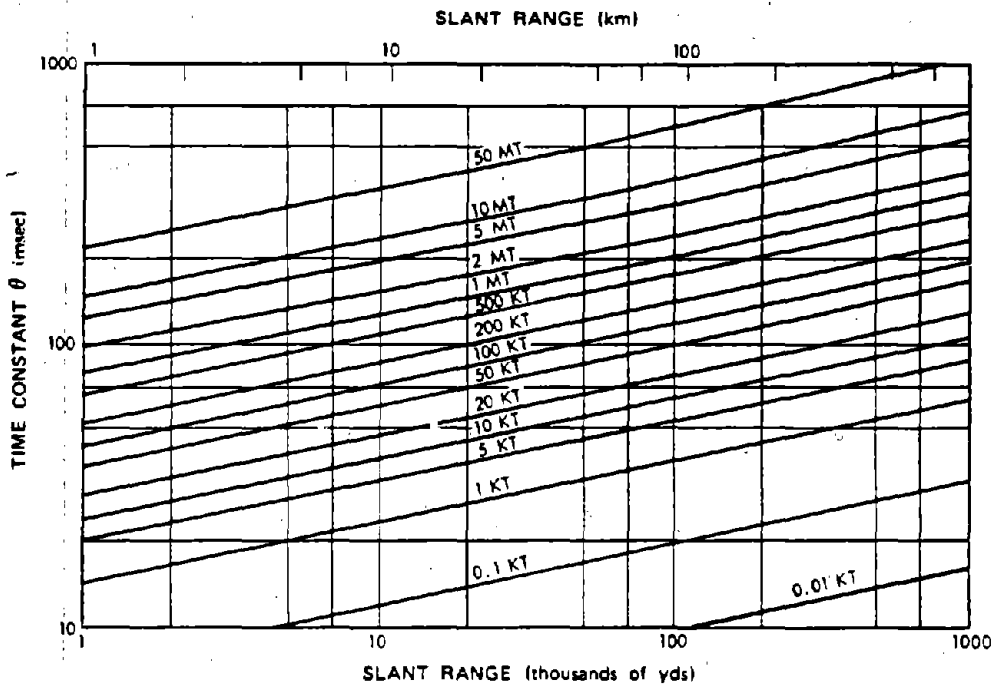


Figure 2-115. Shock Wave Time Constant in Free Isovelocity Water vs Slant Range

2-738-
244

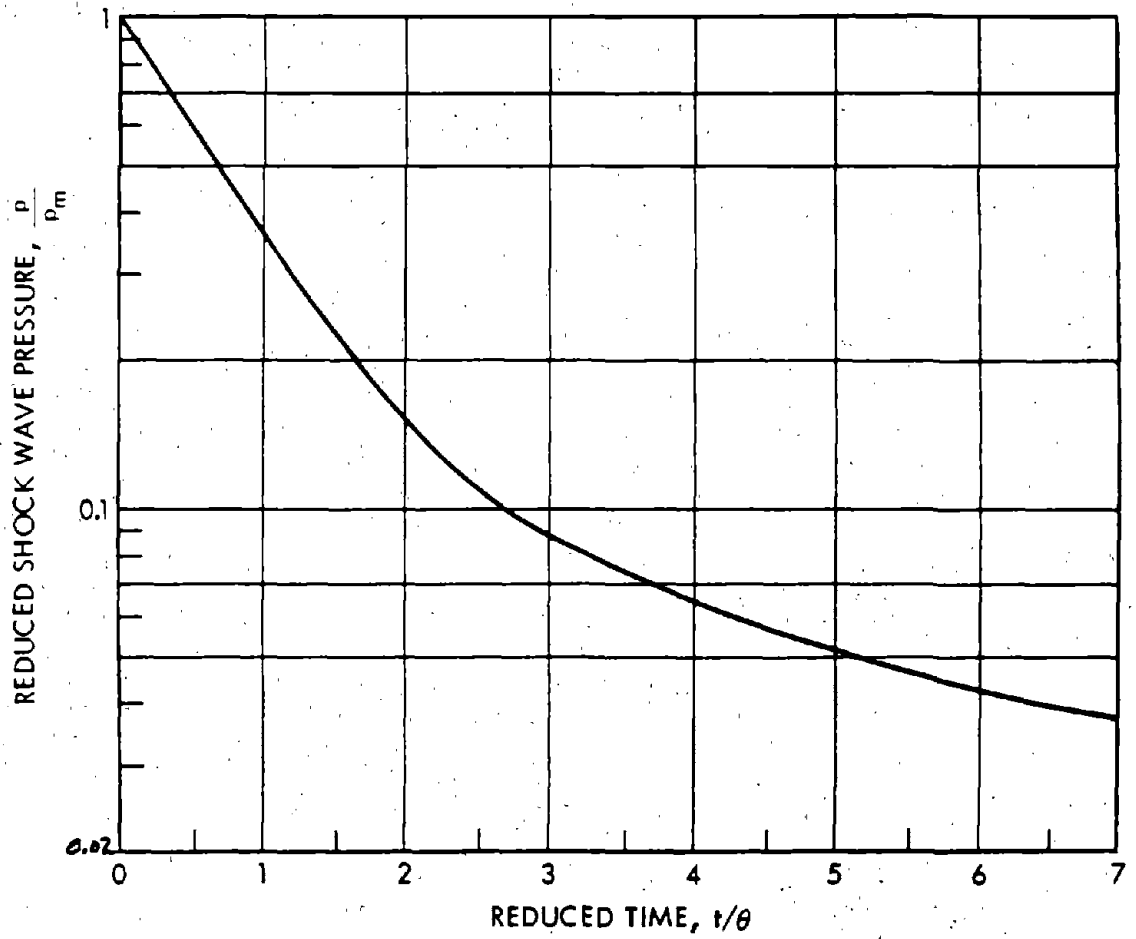


Figure 2-116. Pressure-Time for Free IsovLOCITY Water Shock Waves from Nuclear Explosion

267
2-230

[REDACTED]

**Problem 2-30. Calculation of Shock Wave Parameters for Reduced Water
Depths, $d_w/W^{1/3} < 2,000 \text{ ft/kt}^{1/3}$**

[REDACTED] Figures 2-117 through 2-120 show the influence of surface and bottom reflection on the primary shock wave. The curves are drawn through values of peak pressure and impulse at mid-depth both for explosions at mid-depth (Figures 2-117 and 2-118) and at the bottom (Figures 2-119 and 2-120). The solid curves indicate the approximate coverage of the data. As the water depth approaches zero the dashed curves approach the values for air blast at ground level. Transition to the free-water shock parameters (Figures 2-112 through 2-116) occurs as the water depth increases. In the anomalous region near the water surface, the reflected tension waves lead to a sharp reduction of pressure and impulse (Figure 2-94).

[REDACTED] The curves in Figures 2-117 through 2-120 were derived mainly from H.E. data; however, they were shifted to agree with nuclear data for the limit of free isovelocity water. In most instances, the shift (or conversion factor) was in agreement with the factors determined separately for converting from H.E. to nuclear data in deep water. Most of the data were obtained for the mid-depth location of both the charge and the pressure gauges. All of the curves pertain to either a coral sand or an ordinary sand bottom material.

[REDACTED] Detailed shock wave measurements have been made over concrete, sand, and clayey-silt bottoms to assess the effects of shock reflection from various bottom materials. Measurements were made within 48 ft from 10-lb TNT charges

in 20 ft of water. Both the charge and gauges were placed deeper than mid-depth to minimize the effects of surface reflection.

[REDACTED] Briefly, the following effects were observed for the shock strength, impulse, and energy flux as compared with values at the same range in free water. Near the bottom and away from the charge, the pressure fronts of the incident and reflected shocks were nearly equal. Near the charge and away from the bottom, the reflected shock was about one-fifth as strong as the incident shock. The impulse of the shock wave increased as much as 100 percent near the charge over concrete, but there was little change at the greatest range from the charge. The impulse increased near the charge but decreased further away from it over clayey-silt and sand. The increase was as much as 40 percent over silt and 20 percent over sand. The decrease was as much as 50 percent over silt and 30 percent over sand. The observed changes in energy flux were roughly comparable with those for impulse, although the energy decreased as much as 30 percent away from the charge over concrete.

[REDACTED] The shock wave duration T in milliseconds can be approximated with

$$T = \frac{KI}{P_m}$$

$$K \approx 1.8 + 0.0021 \left(d_w/W^{1/3} \right)$$

$$\text{for } 2,000 > \left(d_w/W^{1/3} \right) > 100$$

$$K \approx 3.0 - 0.01 \left(d_w/W^{1/3} \right)$$

248
2-240

[REDACTED]

[REDACTED]

[REDACTED]

[REDACTED]

for $(d_w/W^{1/3}) < 100$

where

d_w = water depth (ft)

I = shock wave impulse (psi-msec)

p_m = peak shock pressure (psi).

[REDACTED] The shock wave energy flux for an explosion at a reduced depth of approximately $250 \text{ ft}/(kt)^{1/3}$ is related to the shock wave impulse I and peak pressure by

$$E_{250} \approx 1.2 \times 10^{-4} p_m I \text{ in.-lb/in.}^2,$$

and at reduced depths equal to or greater than $2,000 \text{ ft}/(kt)^{1/3}$ by

$$E_{2,000} \approx 9.0 \times 10^{-5} p_m I \text{ in.-lb/in.}^2.$$

For intermediate depths, a linear interpolation between the two values can be adopted.

[REDACTED] The following approximations can be used to estimate the shock parameters at various gauge depths when the charge is at mid-depth, when $250 < R/W^{1/3} < 2,500$ and when $70 < d_w/W^{1/3} < 200$.

Gauge Depth Water Depth	Fraction of Value at Mid-Depth	
3/4 to .1	{	0.9 for peak pressure
		0.8 for impulse
		0.7 for energy impulse
1/4	{	0.8 for peak pressure
		0.7 for impulse
		0.6 for energy flux

0. Use air blast loading

[REDACTED] Example [REDACTED]

Given: A 1 Mt explosion at a depth of 2,500 ft in water having a depth of 5,000 ft.

Find: The peak pressure, the impulse, shock wave duration, and the energy flux depth of 2,500 ft and a horizontal range of 20,000 ft.

Solution: The reduced water depth is

$$\frac{d_w}{W^{1/3}} = \frac{5,000}{(1,000)^{1/3}} = 500 \text{ ft.}$$

The reduced burst depth is

$$\frac{d_b}{W^{1/3}} = \frac{2,500}{(1,000)^{1/3}} = 250 \text{ ft.}$$

The reduced range is

$$\frac{R}{W^{1/3}} = \frac{20,000}{(1,000)^{1/3}} = 2,000 \text{ ft.}$$

Since the explosion is at mid-depth, Fig 2-117 and 2-118 apply. From Figure 2-117, peak pressure is

$$p_m = 700 \text{ psi.}$$

From Figure 2-118, the reduced positive impulse is

$$\frac{I}{W^{1/3}} = 9,000 \text{ psi-msec}/(kt)^{1/3}.$$

Since $2,000 > (d_w/W^{1/3}) > 100$, the shock wave duration equations give

$$K = 1.8 + 0.0021 (d_w/W^{1/3})$$

[REDACTED]

$$K = 1.8 + (0.0021)(500) = 2.85$$

Answer: The peak pressure is

$$p_m = 700 \text{ psi.}$$

The positive impulse is

$$I = (9,000)(W^{1/3}) = 90,000 \text{ psi-msec}$$

The shock wave duration is

$$T = \frac{KI}{p_m} = \frac{(2.85)(9 \times 10^4)}{700} = 366 \text{ msec.}$$

The shock wave energy flux is

$$E_{250} = 1.2 \times 10^{-4} p_m I$$

$$\begin{aligned} E_{250} &= (1.2 \times 10^{-4})(700)(9 \times 10^4) \\ &= 7.6 \times 10^3 \text{ in. lb/in.}^2. \end{aligned}$$

[REDACTED] **Reliability:** Peak pressures obtained from Figures 2-117 and 2-119 are estimated to be reliable within about ± 30 percent. Impulses obtained from Figures 2-118 and 2-120, and energy fluxes are estimated to be reliable to within about ± 50 percent.

[REDACTED] **Related Material:** See paragraphs 2-68 through 2-72.

270
2-702

[REDACTED]

[REDACTED]

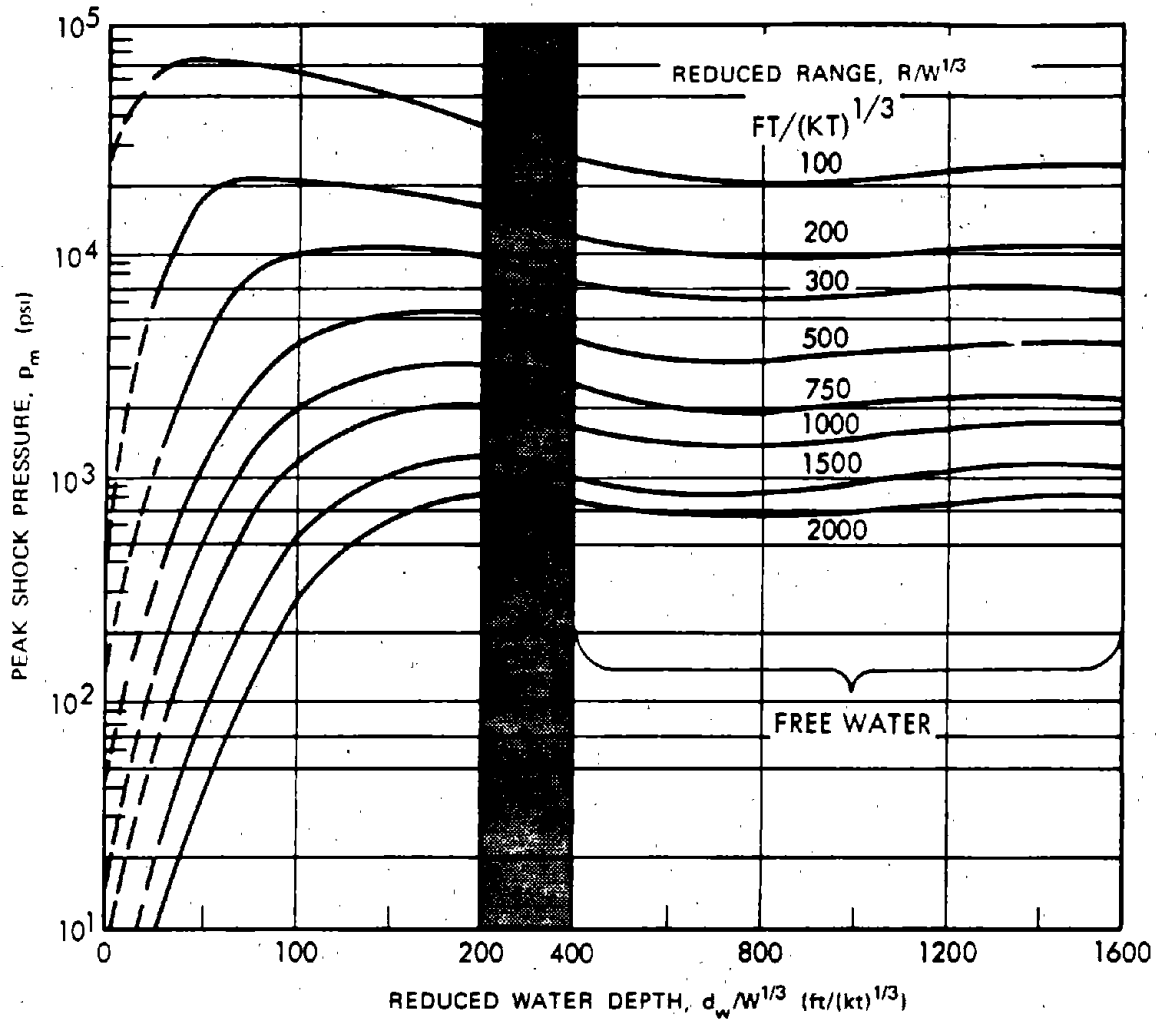


Figure 2-117. Peak Shock Pressure vs Reduced Water Depth. Explosion and Gauges at Mid-Depth.

271
2-288

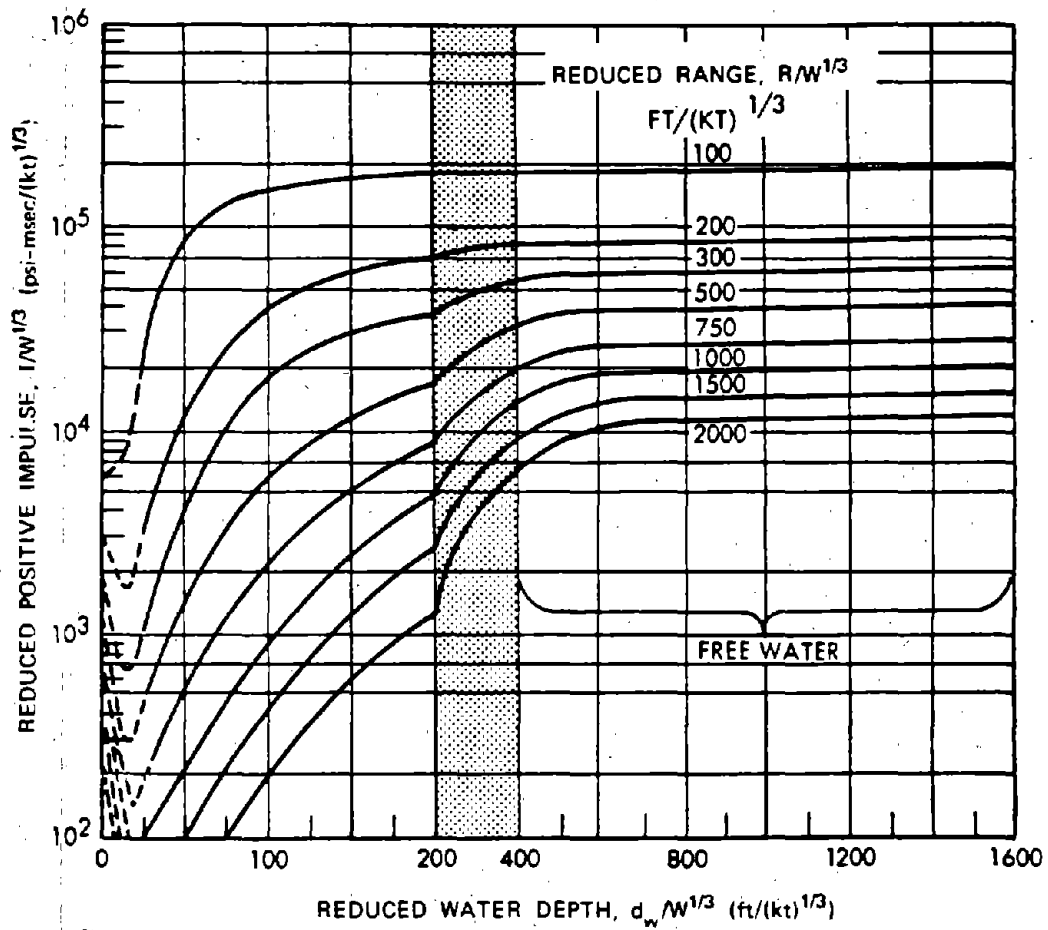


Figure 2-11B. [REDACTED] Reduced Positive Impulse of Shock Wave vs Reduced Water Depth. Explosion and Gauges at Mid-Depth. [REDACTED]

272
 2-244

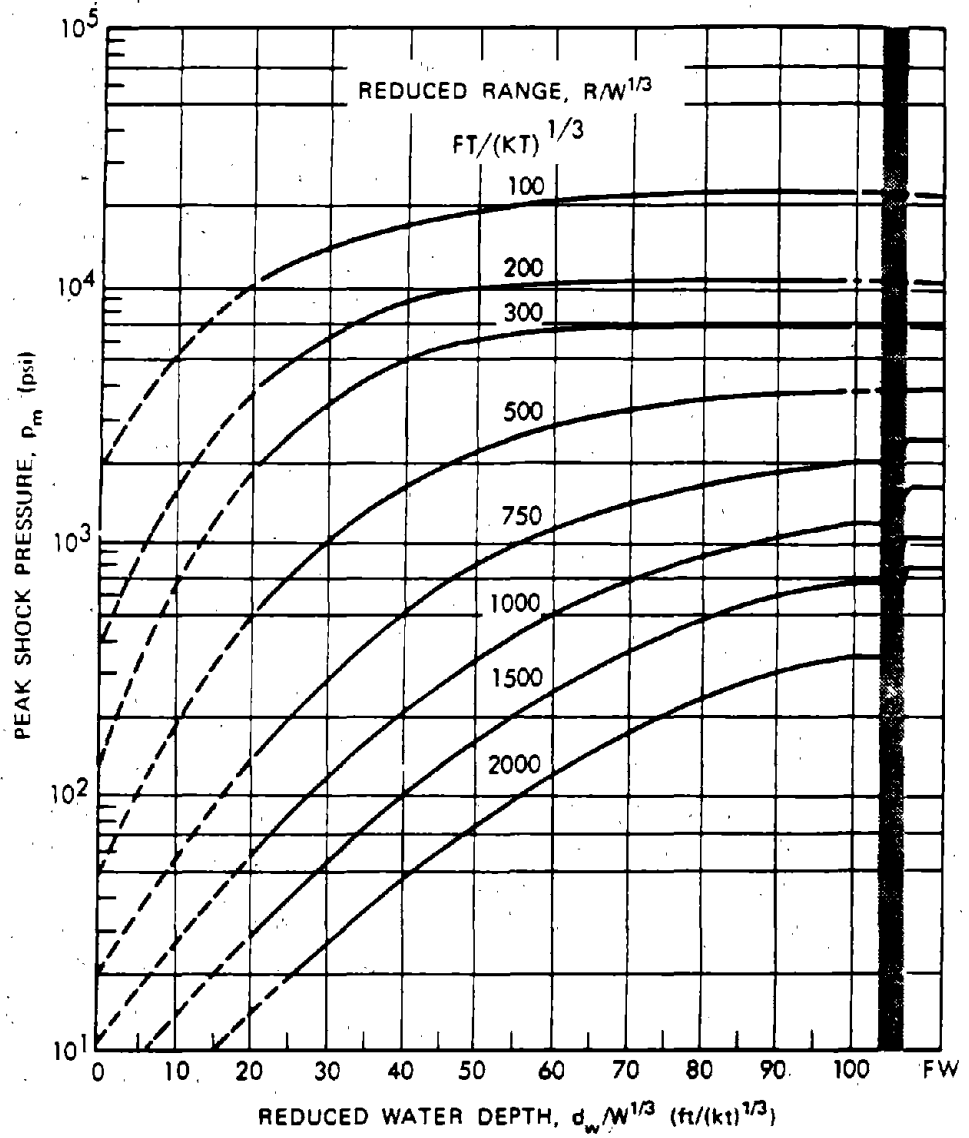


Figure 2-119. [REDACTED] Peak Shock Pressure vs Reduced Water Depth. Explosion on Bottom, Gauges at Mid-Depth. [REDACTED]

273
2-206

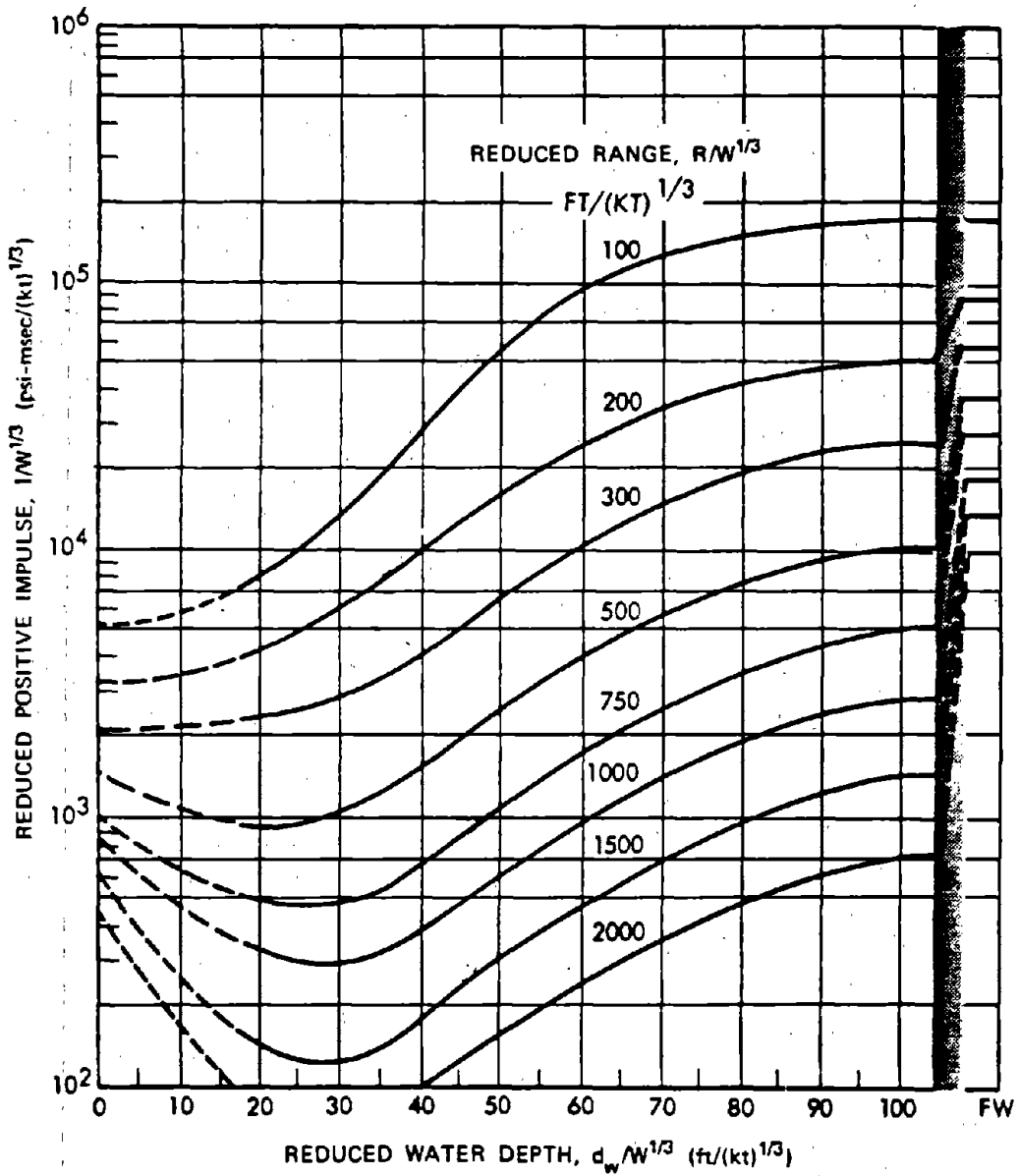


Figure 2-120. [REDACTED] Reduced Positive Impulse vs Reduced Water Depth.
 Explosion on Bottom, Gauges at Mid-Depth. [REDACTED]

274
2-246



[REDACTED]

**Problem 2-31. Calculation of Peak Overpressure Along the Water Surface
as a Function of Underwater Burst Depth**

[REDACTED] Figure 2-121 shows the relations to obtain the maximum air blast overpressure from a scaled underwater explosion as a function of depth of burst and horizontal distance. The air blast is for an altitude just above the surface of the water. To determine the air blast at other altitudes, see the references listed in paragraph 2-72.

[REDACTED] **Example** [REDACTED]

Given: A 10 kt explosion at a depth of 500 ft in deep water.

Find:

- a. The horizontal distance at which a 0.5 psi peak air blast overpressure would be predicted.
- b. The upper and lower limits of the range for item a. that would cover the estimated accuracy.

Solution: The reduced depth of burst is

$$\frac{d_b}{W^{1/3}} = \frac{500}{(10)^{1/3}} = 232 \text{ ft}/(\text{kt})^{1/3}$$

From Figure 2-121, the intersection of the 0.5 psi curve with a reduced depth of $232 \text{ ft}/(\text{kt})^{1/3}$ occurs at a reduced horizontal distance of $0.7 \text{ kft}/(\text{kt})^{1/3}$.

Answer:

- a. The predicted horizontal distance at which 0.5 psi will occur is

$$d = 0.7 W^{1/3} = (0.7)(10)^{1/3}$$

$$d = 1.50 \text{ kilofeet} = 1,500 \text{ feet.}$$

- b. The estimated accuracy in predicting the distance for a given overpressure is ± 30 percent (see "Reliability" below). Thus, the limits are

$$d = 1,500 \times 1.3 = 1,950 \text{ ft (upper limit).}$$

$$d = 1,500 \times 0.7 = 1,050 \text{ ft (lower limit).}$$

[REDACTED] *Reliability:* The accuracy of the relation in Figure 2-121 has not been tested rigorously. The relations provide an approximation based on high-explosive underwater tests and confirmed by a few measurements made at nuclear underwater tests. However, it is felt that ± 30 percent in predicting the distances for maximum overpressure is a realistic accuracy estimate.

[REDACTED] *Related Material:* See paragraph 2-72.

276
2-248

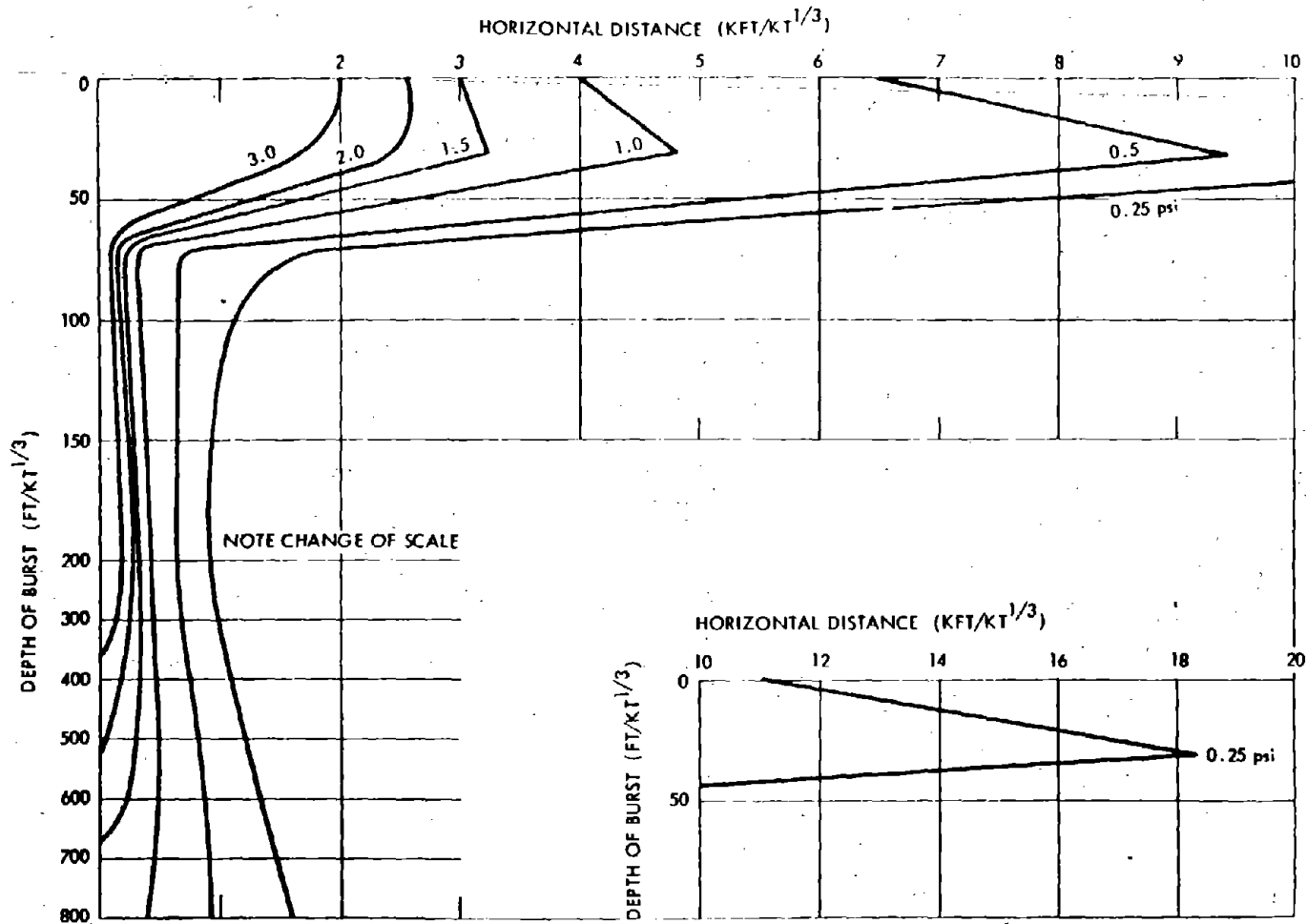


Figure 2-121. Peak Air Blast Overpressure Along the Water Surface from Underwater Nuclear Explosions

[REDACTED]

Problem 2-32. Calculation of the Extent, Initial Vertical Velocity, and Approximate Height of the Spray Dome

[REDACTED] The maximum extent of the spray dome can be estimated with the following relations, which are valid for reduced depths of burst as large as:

$$d_b/W^{1/3} \leq 1.260 \text{ ft}/(\text{kt})^{1/3}$$

$$r_{sd} = d_b \tan \delta_{\max}$$

$$\delta_{\max} = 85.3 - 0.021 (d_b/W^{1/3})$$

where (as shown in the following sketch)

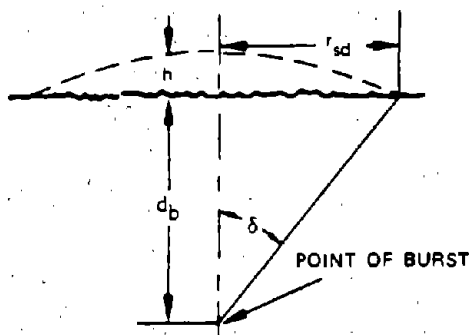
r_{sd} = the horizontal extent of the spray dome (ft).

δ = the spray dome angle, the angle between a vertical line passing through the center of the burst and a line passing through the point of interest on the surface and the center of the burst (degrees).

d_b = the burst depth (ft).

W = the weapon yield (kt).

h = maximum spray dome height (ft).



[REDACTED] Initial spray velocities can be calculated from:

$$V_o = (144 \cos^2 \delta) \frac{p_m}{U}$$

where at a point on the surface.

p_m = peak shock pressure (psi).

U = shock front propagation velocity (ft/sec).

V_o = initial spray velocity (ft/sec.)

[REDACTED] Values of p_m are given in Figure 2-112. Values of U are given in Figure 2-122 as a function of p_m . In practice, the presence of the bottom does not appear to have an influence upon the value for the spray velocity. However, for bursts on the bottom, the yield should be doubled (as an upper limit estimate) when calculating spray velocities.

[REDACTED] Higher velocities than given by the above equation have been observed for deep bursts,* therefore a 50 percent safety factor should be added to calculate values of initial dome velocity.

[REDACTED] An upper limit of dome height h can be derived from:

$$h = V_o t - \frac{1}{2} f t^2$$

where

t = time (sec),

f = retardation factor (ft/sec²),

[REDACTED] Choppy sea, together with "Taylor instability" appear to account qualitatively for this observation.

[REDACTED]

by assuming that gravity is the only retarding force and, therefore, that $f = 16 \text{ ft/sec}^2$. The time that the upper limit height is reached can be determined that the first derivative of h with respect to time (that is, dome velocity) = zero at that time. Therefore,

$$\frac{dh}{dt} = 0 = V_0 - 2(f)t$$

Example

Given:

[REDACTED]

[REDACTED]

DNA
(6)(3)

DNA
(6)(3)

Reliability: Spray dome angles are estimated to be reliable to within ± 10 percent for $d_0/W^{1/3} < 1,260 \text{ ft/(kt)}^{1/3}$. Initial vertical velocities that are calculated by the equations given above might be low by as much as 50 percent, therefore, a safety factor is included in the method. The retardation factor f is taken to be 16 ft/sec^2 to obtain an upper limit for dome height. Actual retardation factors as large as 30 ft/sec^2 have been observed during nuclear tests.

Related Material: See paragraph 2-73.

[REDACTED]

[REDACTED]

[REDACTED]

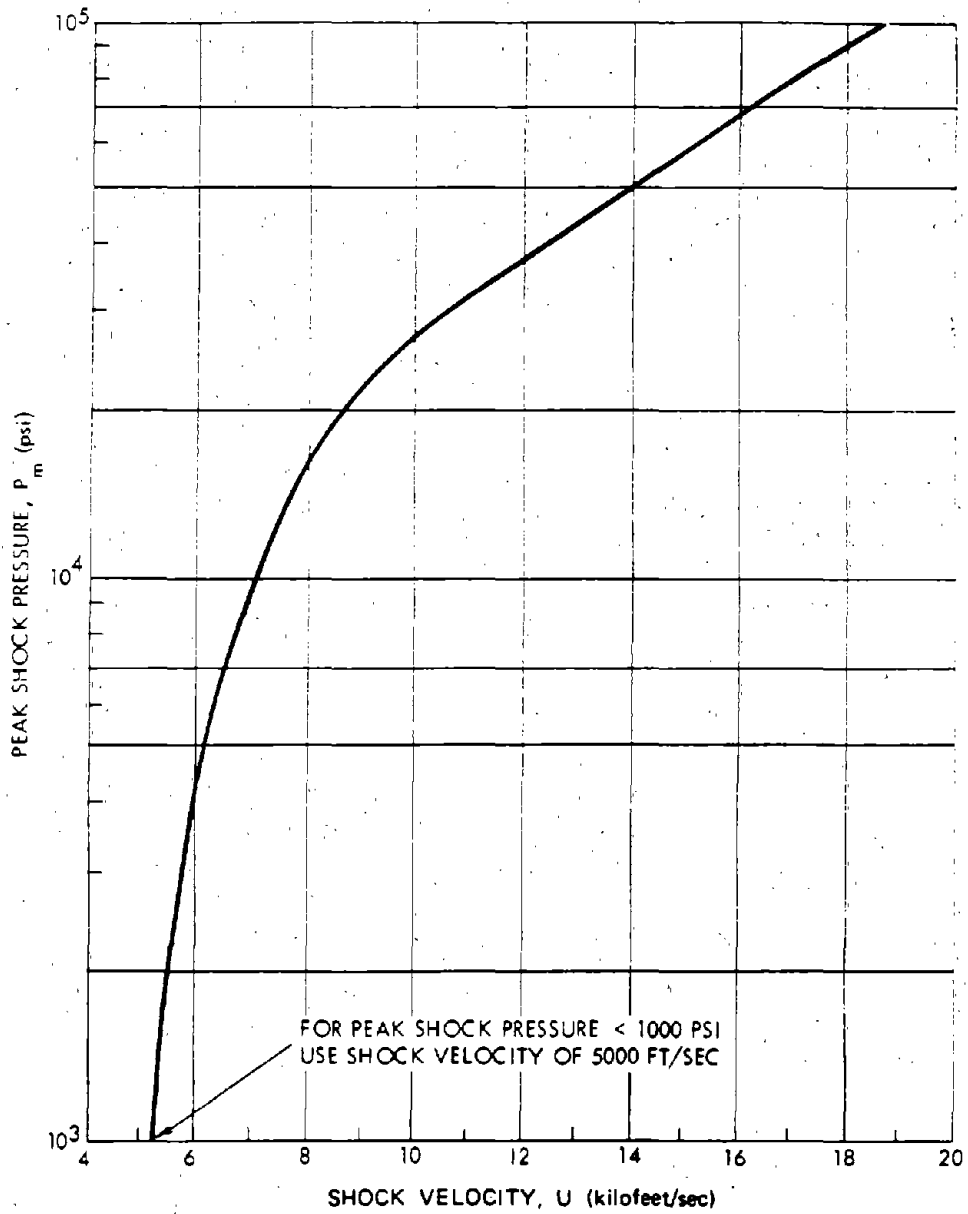


Figure 2-122. Velocity of Shock Wave in Free Water vs Peak Shock Pressure

2-122

[REDACTED]

[REDACTED]

[REDACTED]

**Problem 2-33. Calculation of Plume, Column,
and Cauliflower Formation**

[REDACTED] Figure 2-123 shows reduced plume dimensions as a function of reduced time for very deep and deep explosions. Figure 2-124 shows reduced plume dimensions for shallow bursts and cloud dimensions. The criteria for determining the explosion categories as a function of depth of burst and weapon yield are given in Figure 2-105 and Table 2-8. The accuracy of the predictions obtained from Figures 2-123 and 2-124 has not been established firmly because of the limited number of nuclear tests upon which they are based.

[REDACTED] **Example** [REDACTED]

Given: A 10 kt explosion at a depth of 500 ft in deep water.

Find: The plume radius and plume height 15 seconds after the explosion.

Solution:

$$240 W^{1/4} = 427 \text{ ft}$$

$$700 W^{1/4} = 1,245 \text{ ft.}$$

Since $240 W^{1/4} < d_b < 700 W^{1/4}$, this is a deep burst. The reduced time is

$$\frac{t}{W^{1/3}} = \frac{15}{(10)^{1/3}} \approx 7 \text{ sec}/(\text{kt})^{1/3}.$$

From Figure 2-123, the reduced plume height is about $800 \text{ ft}/(\text{kt})^{1/3}$, and the reduced plume radius is about $700 \text{ ft}/(\text{kt})^{1/3}$.

Answer:

$$\begin{aligned} \text{Plume height} &\approx 800 W^{1/3} \approx (800)(10)^{1/3} \\ &\approx 1,700 \text{ ft.} \end{aligned}$$

$$\begin{aligned} \text{Plume radius} &\approx 700 W^{1/3} \approx (700)(10)^{1/3} \\ &\approx 1,500 \text{ ft.} \end{aligned}$$

[REDACTED] *Reliability:* The curves in Figures 2-123 and 2-124 are estimated to be reliable to within ± 30 percent. For safety considerations, multiply the radius and the height by 1.3. For assurance of damage, multiply the values obtained from the figures by 0.7.

[REDACTED] *Related Material:* See "SURFACE EFFECTS OTHER THAN WAVES," in particular paragraph 2-74. See also Table 2-8 and Figure 2-105.

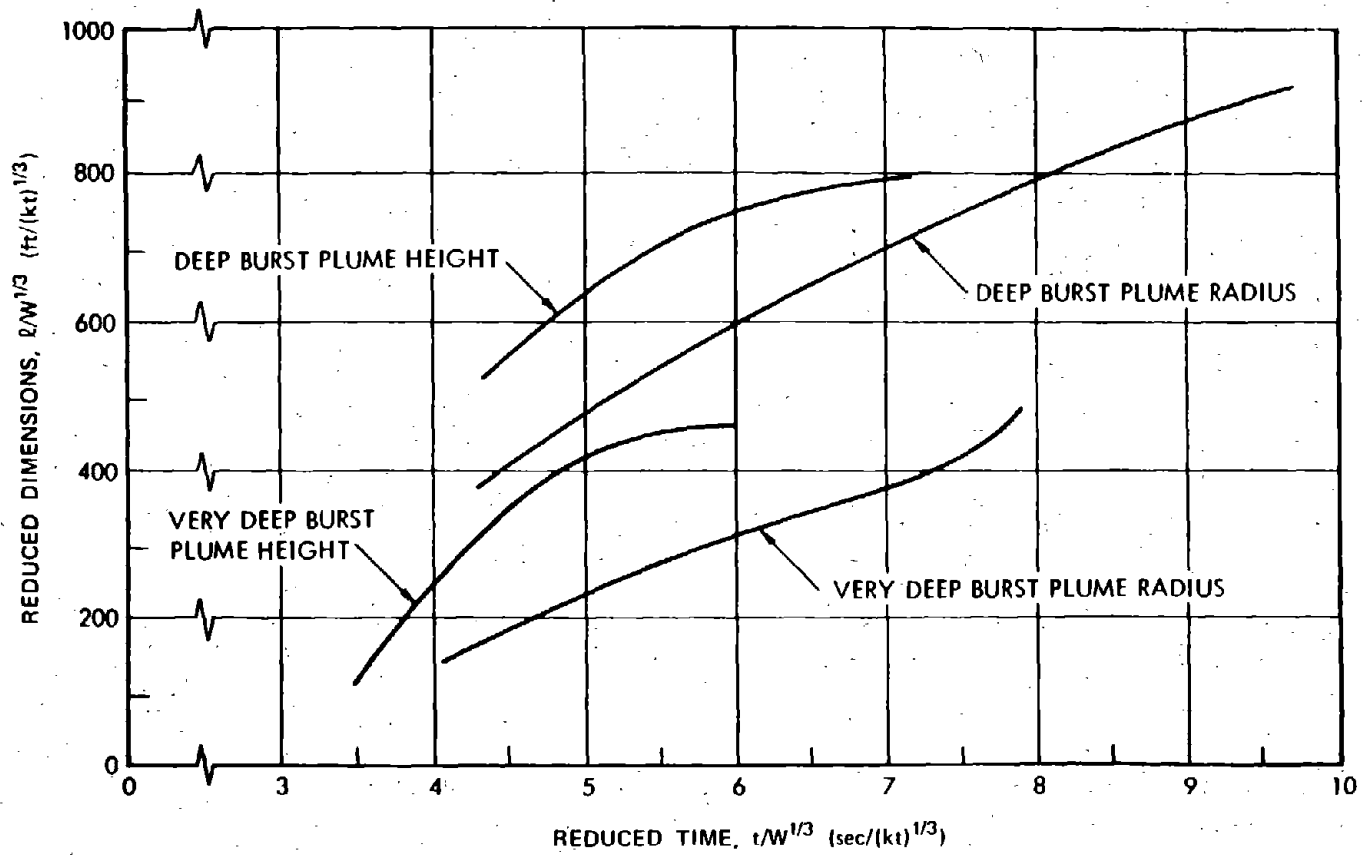


Figure 2-123. Plume Dimensions for Deep and Very Deep Underwater Bursts

281
2-253

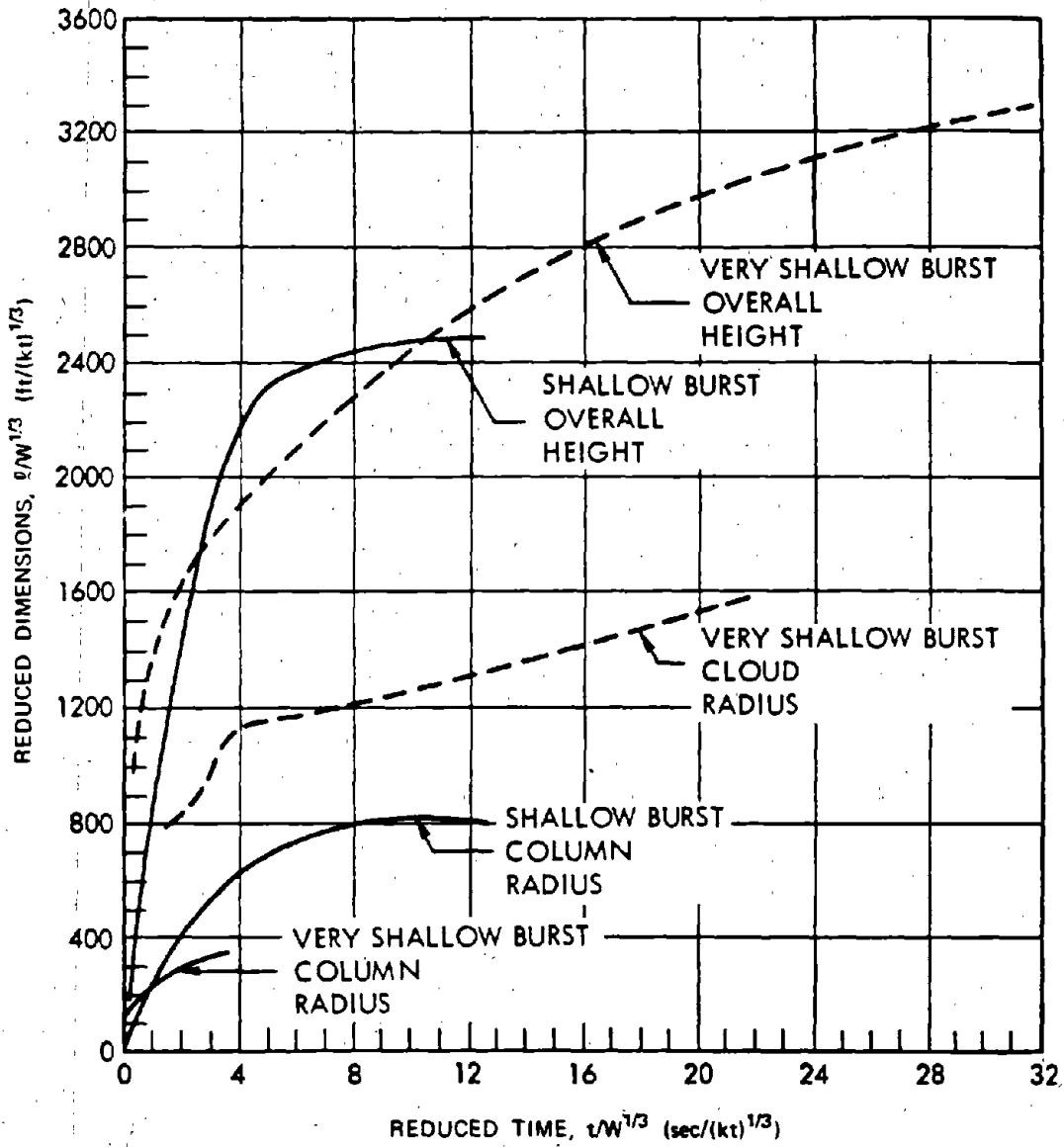


Figure 2-124. Column and Cloud Dimensions for Shallow and Very Shallow Bursts

282
2-254

[REDACTED]

**Problem 2-34. Calculation of Base Surge Growth
and Cloud Height**

[REDACTED] The reduced outside radius of various base surge clouds is shown in Figures 2-126 and 2-127 as a function of reduced time after burst. Figure 2-126 shows a curve that is applicable to shallow and very shallow bursts, while Figure 2-127 shows separate curves for deep and

very deep bursts (see Table 2-8 and Figure 2-105 for burst depth categories). Equations that relate the reduced radii and times to actual radii and times for various explosion conditions are shown below:

Burst Classification	Reduced Radius, R_s (Dimensionless)	Reduced Time, t_s (sec/ft ^{1/3})	Equation for Estimated* D_{max} (ft) or A_{max}	Applicable Figure
Very shallow	R_s/D_{max}	$t_s(D_{max})^{1/2}$	$D_{max} = 710 W^{1/3} *$	2-125
Shallow	R_s/D_{max}	$t_s(D_{max})^{1/2}$	$D_{max} = 377 W^{1/3} (d_b/W^{1/3})^{1/6}$	2-125
Deep and very deep	R_s/A_{max}	$t_s(A_{max})^{1/2}$	$A_{max} = 1,500 (W/Z)^{1/3}$	2-126

[REDACTED] The equation $D_{max} = 710 W^{1/3}$ is valid for very shallow explosions off the bottom. The equation $D_{max} = 377 W^{1/3} (d_b/W^{1/3})^{1/6}$ is valid for very shallow and shallow explosions on a bottom.

where

W = yield of the weapon (kt)

R_s = radius of the base surge (ft)

t_s = time after explosion (sec)

d_b = depth of the explosion (ft)

$Z = d_b + 33$ = total hydrostatic pressure at d_b (ft of water)

D_{max} = estimated maximum column radius (ft)

A_{max} = estimated maximum bubble radius (ft).

Figure 2-125 was developed to approximate the height of the visible base surge for use with radiation exposure calculations. The curve in Figure 2-125 was drawn under the assumption that the height is not a function of yield or depth of burst. This assumption probably is not correct, but there is not sufficient information to incorporate these parameters.

Example (U):

Given: A 40 kt explosion at a depth of 200 feet.

Find:

- The base surge radius R_s .
- The height of the visible cloud h_c 10 minutes after burst.

Solution: Refer to Table 2-8:

$$21 W^{1/3} = (21)(40)^{1/3} = 72 \text{ ft,}$$

$$75 W^{1/3} = (75)(40)^{1/3} = 256 \text{ ft,}$$

therefore, a 40 kt explosion at a depth of 200 feet is a very shallow explosion. From the relations given above (since the burst was not described as being on the bottom)

$$D_{max} = 710 W^{1/3} = (710)(40)^{1/3} = 2,430 \text{ ft,}$$

and

$$t_{cr} = \frac{t_s}{(D_{max})^{1/2}} = \frac{600}{(2,430)^{1/2}} = 12.2 \text{ sec.}$$

From Figure 2-126, the reduced base surge radius is about 7.

Answer:

$$a. R_s \approx R_{cr} \times D_{max} = (7)(2,430)$$

$$R_s \approx 17,000 \text{ ft.}$$

b. From Figure 2-125, the height of the base surge cloud is

$$h_c \approx 2,000 \text{ ft.}$$

Reliability: Base surge radii obtained from Figures 2-125 and 2-126 are estimated to be reliable to within ± 20 percent. No estimate can be made of the reliability of the height of the base surge cloud obtained from Figure 2-127.

Related Material: See paragraph 2-75. See also Table 2-8 and Figure 2-105.

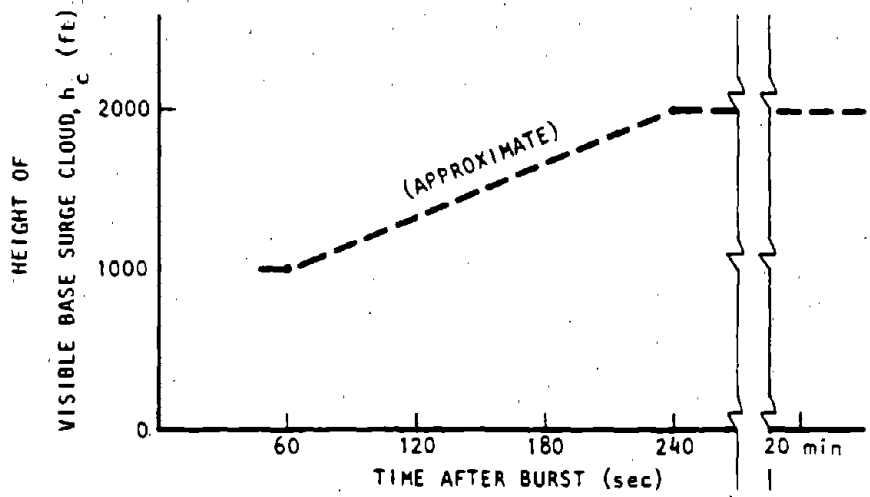


Figure 2-125. Height of Visible Base Surge Cloud as a Function of Time After Burst



2-258
ZK

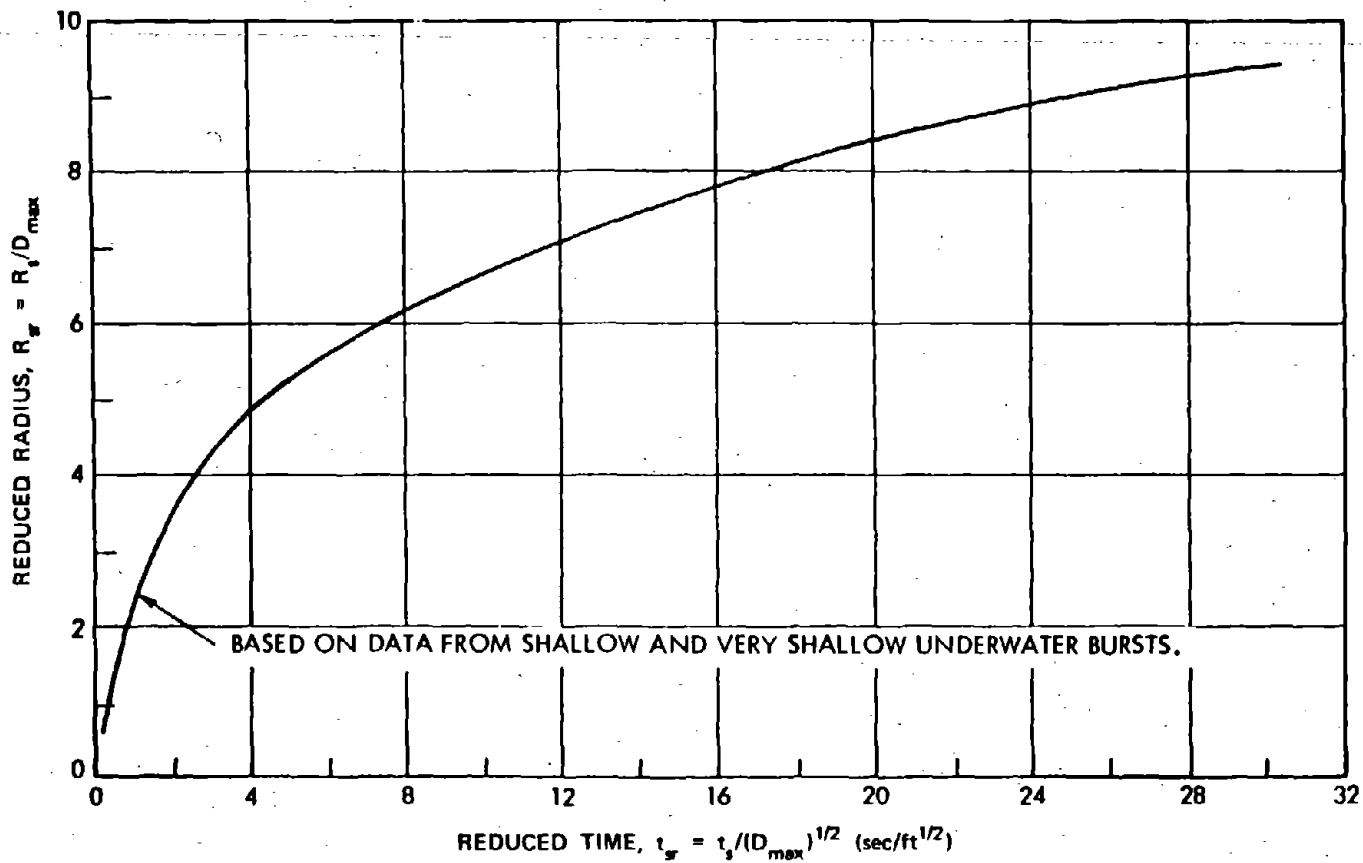


Figure 2-126. Reduced Base Surge Radius vs Reduced Time for Shallow and Very Shallow Bursts

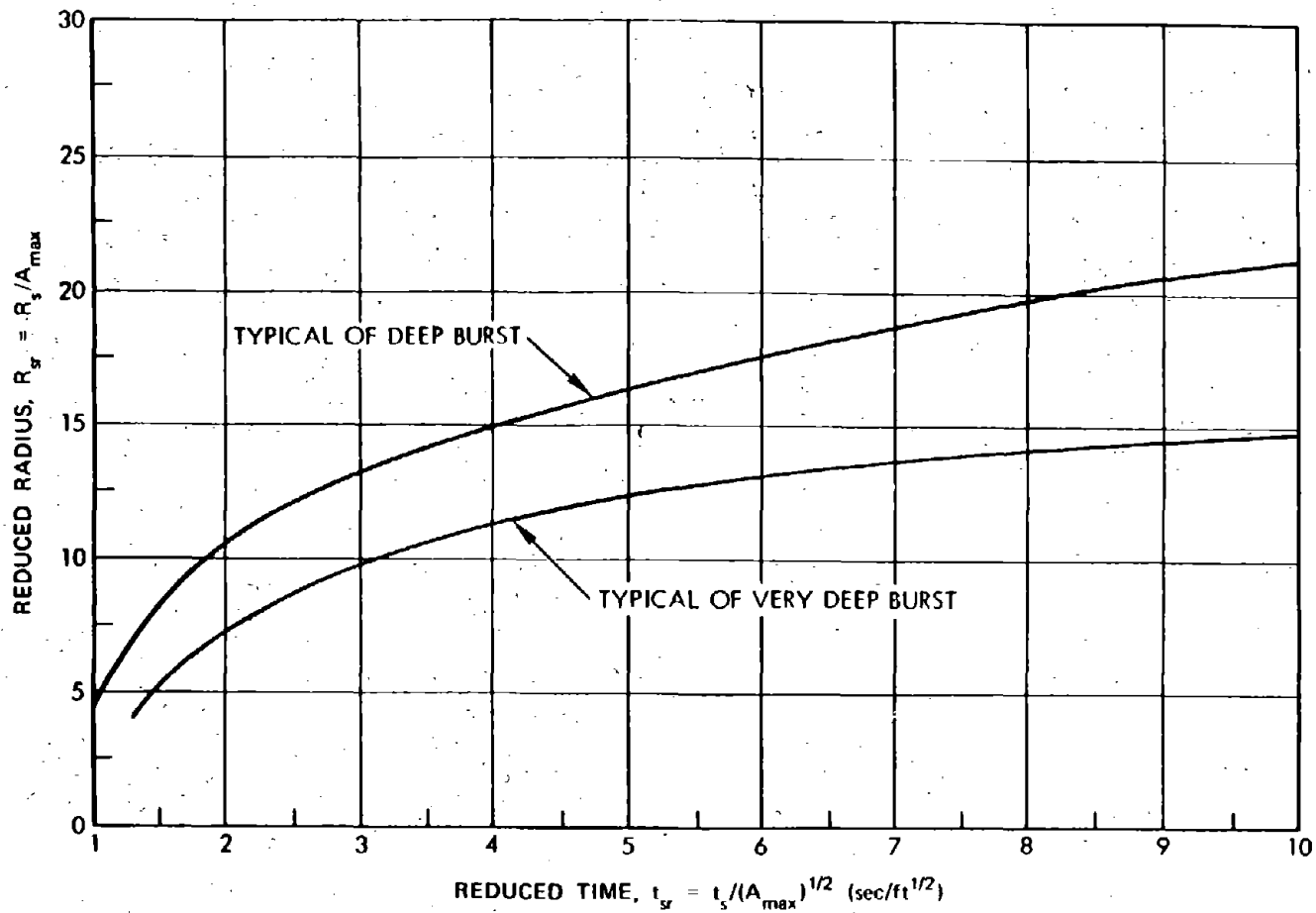


Figure 2-127. Reduced Base Surge Radius vs Reduced Time for Deep and Very Deep Bursts

287
2-560

[REDACTED]

**Problem 2-35. Calculation of the Properties of
Water Surface Waves**

[REDACTED] Figure 2-128 shows the peak wave height (crest to trough) for any depth of burst in shallow water (for waves, shallow water is $0 < d_w \leq 100 W^{1/4}$, see paragraph 2-77), and for any depth of burst not greater than five times the lower critical depth ($0 \leq d_b/5 \leq 170 W^{1/4}$, see paragraph 2-77) in deep water (for waves $d_w \geq 256 W^{1/4}$). The dashed transitional curve in Figure 2-128 can be used for intermediate depths. For any depth of burst in shallow water, and for bursts as low as the lower critical depth ($d_b = 170 W^{1/4}$) in deep water, the foregoing limits on water depth are also the estimated cavity radii as shown in Figure 2-128. For nuclear explosions in deep water at shallow depths of burst near the upper critical depth ($d_b \approx 8.6 W^{1/3}$), the peak wave height may be nearly twice as large as predicted in Figure 2-128 (see Figure 2-107).

Example

[REDACTED]

Reliability

1. Deep water.
 - a. The cavity radius given by the equation

DNA
(2)(3)

DNA
(2)(3)

[REDACTED]

in paragraph 2-77 agrees within [REDACTED] percent with the measured values shown in Table 2-10 for the H.E. tests at Mono Lake (for which the predicted value is 66.5 ft).

DNA
(6-)(3)

[REDACTED]

b. The peak wave height given in Figure 2-128 and the equation in paragraph 2-77 agrees with the measured H.E. data within a factor of two, and within [REDACTED] percent of the measured data of the two nuclear explosions.

DNA
(6-)(3)

[REDACTED]

2. Shallow water.

a. The cavity radius given by the equation in paragraph 2-77 (and Figure 2-128) provides a lower limit for explosions in shallow water. An upper limit is probably half the maximum bubble radius given by the equation in paragraph 2-67.

b. The peak wave height given by the equation in paragraph 2-77 (and in Figure 2-128) agrees with the measured values within about a factor of 2, which is roughly the uncertainty of the data.

Related Material: See paragraphs 2-67 and 2-77. See also Tables 2-9 and 2-10.

[REDACTED]

[REDACTED]

[Redacted]

DNA
(6)(3)

Deleted

Figure 2-128. Peak Wave Height H as a Function of Yield W
frange R and Water Depth d_w

ZAD
2-262

[Redacted]

[Redacted]



[REDACTED]

Problem 2-36. Calculation of Underwater Crater Dimensions

[REDACTED] Figures 2-129 through 2-131 show the apparent crater radius, the apparent crater depth, and the average height of the crater lip, respectively, as a function of weapon yield. Figures 2-129a, 2-130a, and 2-131a are for surface bursts. Figures 2-129b, 2-130b, and 2-131b are for bursts near a clayey sand bottom. Linear interpolation between the curves may be used for bursts between the surface and the bottom.

[REDACTED] The curves in Figures 2-129 through 2-131 were developed from nuclear cratering data; however, H.E. data were used to obtain scaling laws and the shape of the curves for bottom placement. Data from about 600 H.E. and [REDACTED] nuclear explosions were used in the preparation of the curves. The nuclear data are shown in Table 2-11, [REDACTED]

DNA
(2)(3)

[REDACTED] The critical water depth dividing washed and unwashed craters can be found from Figure 2-132 for a clayey-sand bottom. An unwashed crater results when the water depth is less than the minimum height of the irregular cavity lip and when the lip does not fail. For other bottom materials, the critical water depth can be found by multiplying the value of d_c by the appropriate soil factor for crater lip height in Table 2-12.

[REDACTED] **Example** [REDACTED]

Given: A 40 kt explosion on the bottom, which consists of oceanic ooze, in 60 feet of water.

Find: The radius, depth, and lip height of the apparent crater.

Solution: From Figures 2-129, 2-130, and 2-131, the crater dimensions in clayey sand are

292
2-28*

Table 2-11. Partial Compilation of Nuclear Cratering Data

[Redacted]

Deleted

DNA
(26)(3)

[Redacted]

[Redacted]

Table 2-12. Soil Factors for Cratering in Various Materials as Compared with Clayey Sand

Material	Soil Factors		
	Crater Radius	Crater Depth	Crater Lip Height
Clayey sand	1.0	1.0	1.0
Sand	1.1	0.8	0.7
Loess	0.9	1.3	1.2
Muck*	1.5	0.5	0.4
Clayey silt	1.1	1.1	1.0
Coral sand	0.9	0.8	0.7
Clay	0.9	1.4	1.3
Soft rock	0.8	0.6	0.6
Hard rock*	0.6	0.4	0.4
Oceanic ooze*	1.7	0.2	0.1

* Soil Factors estimated or interpolated from the others based on experimental data.

radius, $r_{ac} \approx 750$ ft,

depth, $d_{ac} \approx 42$ ft,

lip height, $h_l \approx 1.7$ ft.

Answer: The corresponding dimensions for oceanic ooze are (Table 2-12)

$r_{ac} \approx (1.7)(750) \approx 1,275$ ft,

$d_{ac} \approx (0.2)(42) \approx 8$ ft,

$h_l \approx (0.1)(1.7) \approx 0.2$ ft.

Reliability



Dimensions from these curves are considered to have the following reliabilities:

radius +150%-50%

depth +150%-50%

lip height +160%-60%

The accuracy of the soil factors shown in Table 2-12 is unknown.

Related Material: See "UNDERWATER CRATERING," page 2-223.

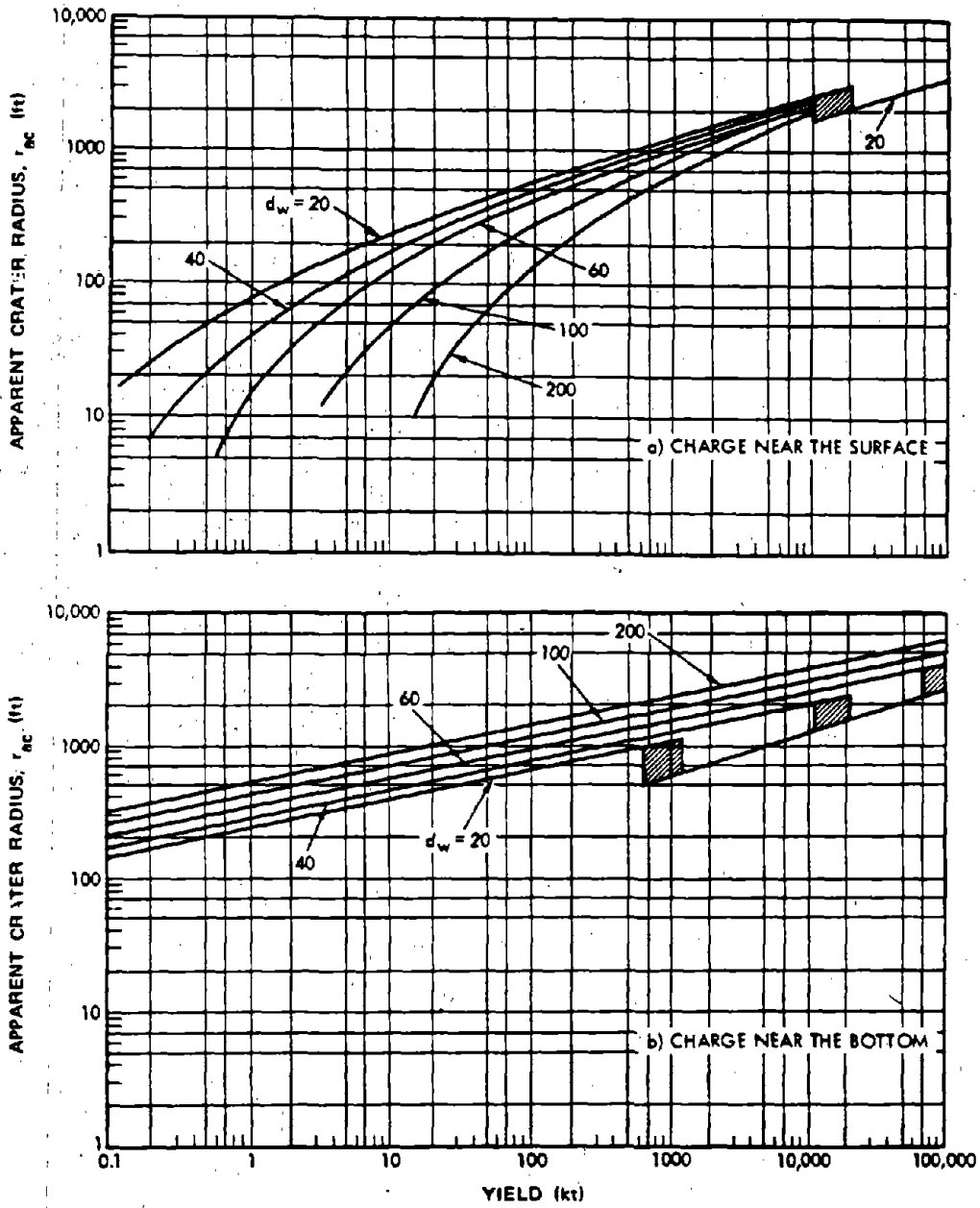


Figure 2-129. Apparent Crater Radius as a Function of Yield for Various Water Depths Over a Clayey Sand Bottom, where d_w = Water Depth in Feet. Shaded Areas Denote Possible Transition Regions from a Washed to an Unwashed Crater for $d_w = 20, 40, \text{ and } 60$.

294
2-286

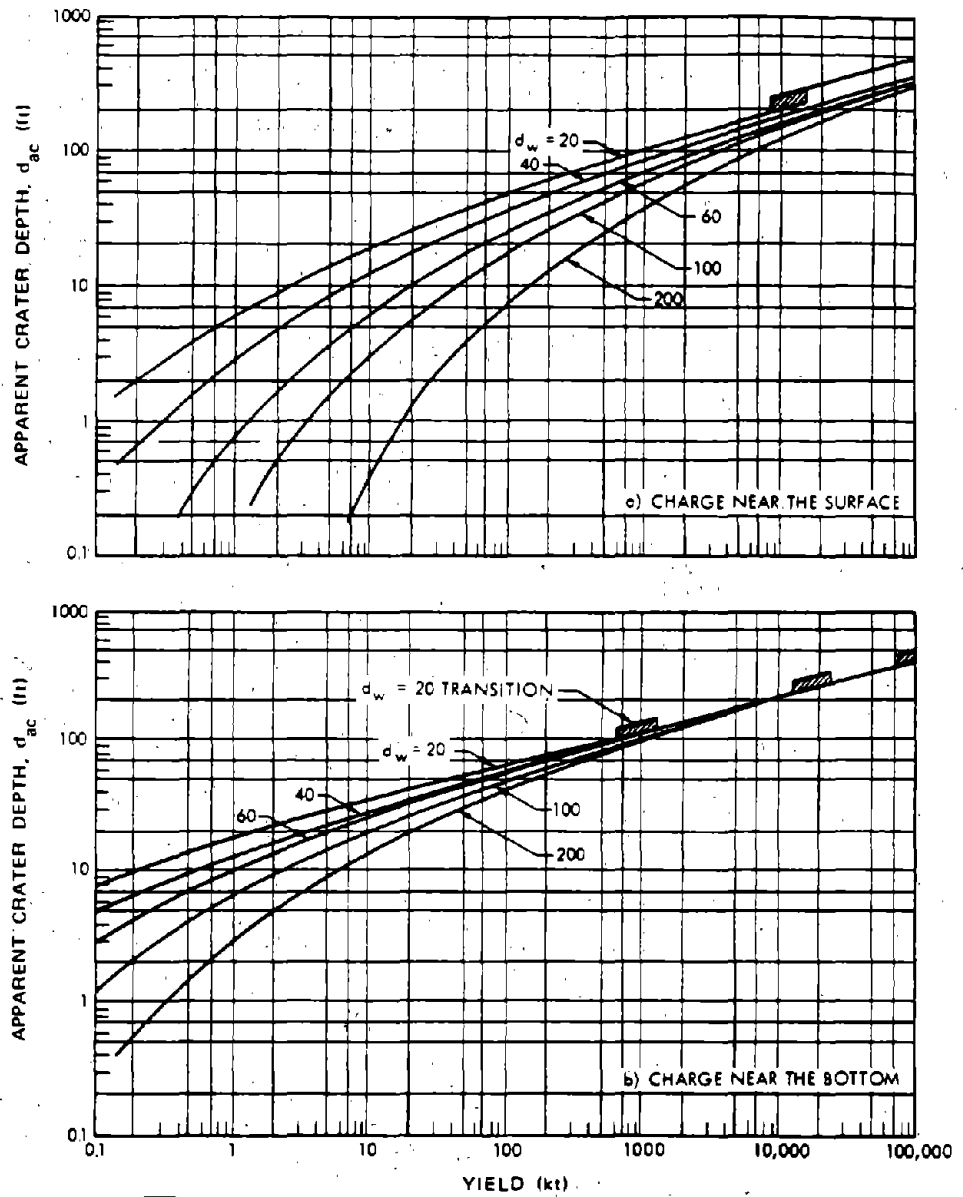


Figure 2-130. Apparent Crater Depth as a Function of Yield for Various Water Depths Over a Clayey Sand Bottom, where d_w = Water Depth in Feet. Shaded Areas Denote Possible Transition Regions from a Washed to an Unwashed Crater for $d_w = 20, 40, \text{ and } 60$.

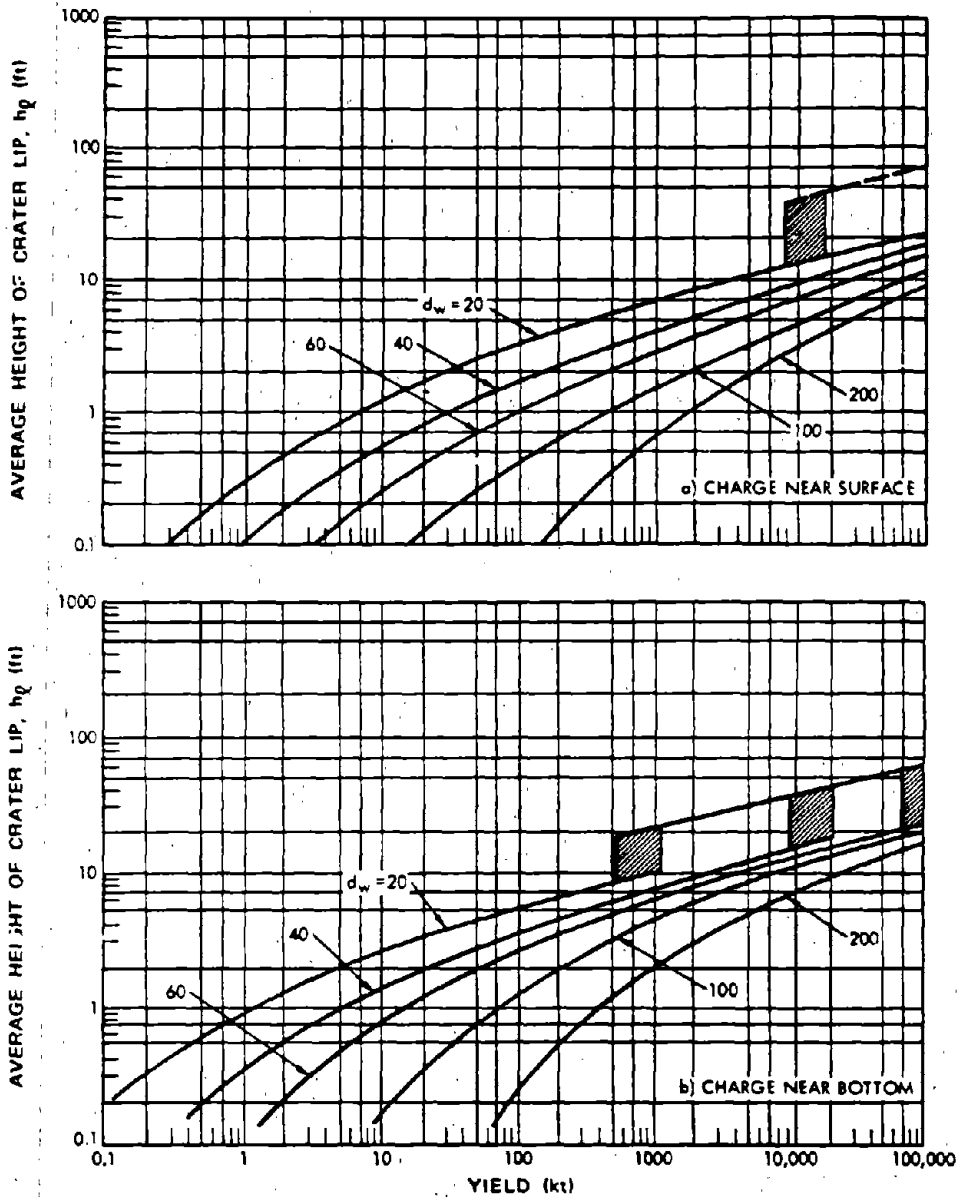


Figure 2-131. Average Height of Crater Lip as a Function of Yield for Various Water Depths with the Charge Near a Clayey Sand Bottom, where d_w = Water Depth in Feet. Shaded Areas Denote Possible Transition Regions from Crater for $d_w = 20, 40, \text{ and } 60$.

296
2-258

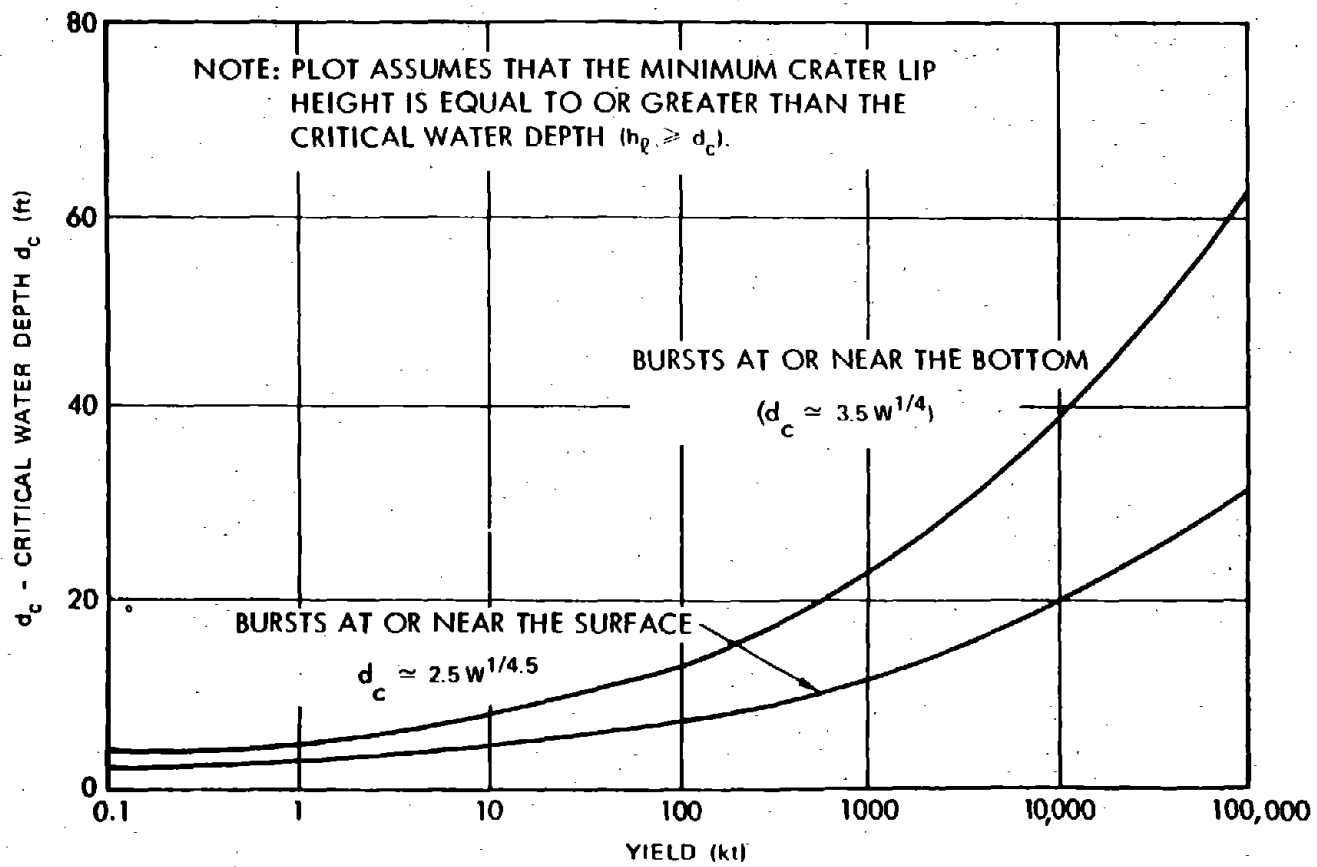


Figure 2-132. Estimated Critical Water Depth as a Function of Yield for a Clayey Sand Bottom

[REDACTED]

BIBLIOGRAPHY

Allen, R. T., *The Effect of an Open Emplacement Hole on Crater Formation near Optimum Depth of Burial* [REDACTED] DASA 2680, Systems, Science, and Software, La Jolla, California, 23 March 1971 [REDACTED]

Barash, R. M., and H. G. Snay, *Effect of Refraction on Safe Delivery Ranges for Submarine-Launched Underwater Nuclear Weapons* [REDACTED] NOLTR-62-199, U.S. Naval Ordnance Laboratory, White Oak, Silver Spring, Maryland, June 1963 [REDACTED]

Barash, R. M., and J. A. Goertner, *Refraction of Underwater Explosion Shock Waves: Pressure Histories Measured at Caustics in a Flooded Quarry*, NOLTR-67-9, U.S. Naval Ordnance Laboratory, White Oak, Silver Spring, Maryland, 19 April 1967 [REDACTED]

Blake, T. R., and D. E. Wilkins, *The Effect of an Open Emplacement Hole on the Crater Produced at Shallow Depth of Burial* [REDACTED] DNA 2813T, 3SCR-841, Systems, Science, and Software, La Jolla, California, October 1971 [REDACTED]

Carlson, R. H., and W. A. Roberts, *Project SEDAN, Mass Distribution and Throwout Studies*, PNE-217E, The Boeing Company, Seattle, Washington, August 1963 [REDACTED]

Circeo, L. J., and M. D. Nordyke, *Nuclear Cratering Experience at the Pacific Proving Grounds*, UCRL-12172, University of California Lawrence Radiation Laboratory, Livermore, California, November 1964 [REDACTED]

Cole, R. H., *Underwater Explosions*, Dover Publications, Inc., New York, N.Y., 1965 [REDACTED]

Cooper, H. F., Jr., *Free-Field Ground Motions from Surface Bursts on Rock* [REDACTED] AFWL-TR-67-94, Air Force Weapons Laboratory, Kirtland Air Force Base, Albuquerque, New Mexico, December 1967 [REDACTED]

Davis, L. K., and A. D. Rooke, Jr., *Project DANNY BOY, Mass Distribution Measurements of Crater Ejecta and Dust; Appendix B: Volumetric Equalities of the Crater* [REDACTED] Miscellaneous Paper No. 1-754, U.S. Army Waterways Experiment Station, Vicksburg, Mississippi, February 1965 [REDACTED]

Davis, L. K., and J. V. Strange, *Cratering Experiments at Mono Lake*, U.S. Army Engineer Waterways Experiment Station, Vicksburg, Mississippi, November 1966 [REDACTED]

Davis, L. K., *MINE SHAFT Series, Events MINE UNDER and MINE ORE, Subtask, N121, Crater Investigations*, Technical Report N-70-8, U.S. Army Engineer Waterways Experiment Station, Vicksburg, Mississippi, March 1970 [REDACTED]

29P
2-270

[REDACTED]

[REDACTED]

Davis, L. K., *Effects of a Near-Surface Water Table on Crater Dimensions*, Miscellaneous Paper No. 1-939, U.S. Army Engineer Waterways Experiment Station, Vicksburg, Mississippi, October 1967 [REDACTED]

Divoky, D. J., and B. LeMéhauté, *Handbook of Explosion-Generated Water Waves, Vol. II - Applications* [REDACTED] Report No. TC-130C, Tetra Tech, Inc., Pasadena, California, December 1969 [REDACTED]

Dodge, Carl, Jr., *A Photographic Investigation of the Spray Dome Produced by Shallow Underwater Explosions* [REDACTED] NOLTR-63-273, U.S. Naval Ordnance Laboratory, White Oak, Silver Spring, Maryland, 13 March 1964 [REDACTED]

Fisher, P. R., R. J. Kley, and H. A. Jack, *Geologic Investigations and Engineering Properties of Craters*, PNE-1103, U.S. Army Engineer Nuclear Cratering Group, Livermore, California, May 1969 [REDACTED]

Fitchett, D. J., *MIDDLE COURSE I Cratering Series*, Technical Report 35, U.S. Army Engineer Nuclear Cratering Group, Livermore, California, June 1971 [REDACTED]

Frandsen, A. D., *Project CABRIOLET, Engineering Properties Investigations of the CABRIOLET Crater*, PNE-957, U.S. Army Engineer Nuclear Cratering Group, Livermore, California, March 1970 [REDACTED]

Kaplan, K., and O. H. Criner, *A Study of Explosion-Generated Surface Water Waves* [REDACTED] URS 162-8, URS Corporation, Burlingame, California, December 1963 [REDACTED]

Kaplan, K., and N. R. Wallace, *Surface Waves from Nuclear Explosions* [REDACTED] URS 190-1, DASA 1240(8), URS Corporation, Burlingame, California, March 1962 [REDACTED]

Kaplan, K., C. Wiehle, *Air Blast Loading in the High Shock Strength Region* [REDACTED] Part II, Prediction Methods and Examples, URS 633-3, DASA 1460-1, URS Corporation, Burlingame, California, February 1965 [REDACTED]

Kaulum, K. W., and M. A. Olson, *Containment of Explosion Products from a Deep Underwater Explosion (Chase V) - Final Report* [REDACTED] USNRDL-TR-67-60, U.S. Naval Radiological Defense Laboratory, San Francisco, California, 5 May 1967 [REDACTED]

Kot, C. A., *Hydra Program: Theoretical Study of Bubble Behavior in Underwater Explosions*, USNRDL-TR-747, U.S. Naval Radiological Defense Laboratory, San Francisco, California, 15 April 1964 [REDACTED]

Kranzer, H. C., and J. B. Keller, "Water Waves Produced by Explosions," *J. Appl. Phys.*, Vol. 30, No. 3, March 1959, pp. 398-407 [REDACTED]

[REDACTED]

Kriebel, A. R., *Analysis of Water Waves Generated Explosively at the Upper Critical Depth* [REDACTED]

URS 679-1, 2, 3, URS Corporation, Burlingame, California, January 1968 [REDACTED]

Lewis, J. G., *Ground Shock and Survival or Kill of Military Systems* [REDACTED] DASA 1836,
Defense Atomic Support Agency, Washington, D.C., October 1966 [REDACTED]

Maine, C. I., J. R. Carbonell, and I. Dyer, *Mechanisms in the Generation of Airblast by Underwater Explosions*, Bolt, Beranek and Newman Report No. 1434, NOLTR-66-88, U.S. Naval Ordnance Laboratory, White Oak, Silver Spring, Maryland, 23 September 1966 [REDACTED]

Moulton, J. F., Jr., *Height-of-Burst Curves Above 100 psi, Shock, Vibration, and Associated Environments, Protective Construction* [REDACTED] Part I, DDR&E Bulletin-32, U.S. Naval Ordnance Laboratory, White Oak, Silver Spring, Maryland, November 1963 [REDACTED]

Military Engineering with Nuclear Explosives, DASA 1669, U.S. Army Engineer Nuclear Cratering Group, Livermore, California, June 1966 [REDACTED]

Newmark, N. M., and W. J. Hall, *Preliminary Design Methods for Underground Protective Structures*, AFSWC-TDR-62-6, University of Illinois, Urbana, Illinois, June 1962 [REDACTED]

Newmark, N. M., *Notes on Shock Isolation Concepts*, Vibration and Civil Engineering Proceedings of Symposium of British National Section International Association for Earthquake Engineering, pp. 71-82, Butterworths, London, 1966 [REDACTED]

Nuclear Weapons Blast Phenomena [REDACTED] DASA 1200-I, -II, -III, -IV, Defense Atomic Support Agency, Washington, D.C., Vol. I, March 1971, Vol. II, December 1970, Vol. III, 1 March 1970, Vol. IV, to be issued during calendar year 1972 [REDACTED]

Peckham, P. and J. F. Pittman, *Airblast from Lithanol Charges Fired Underwater* [REDACTED] NOLTR-68-174, U.S. Naval Ordnance Laboratory, White Oak, Silver Spring, Maryland, 2 December 1968 [REDACTED]

Phillips, D. E., and T. B. Heathcote, *Underwater Explosion Tests of Two Steam Producing Explosives, I. Small Charge Tests*, NOLTR-66-79, U.S. Naval Ordnance Laboratory, White Oak, Silver Spring, Maryland, 23 May 1966 [REDACTED]

Phillips, D. E., and H. G. Snay, *The Parameters of Underwater Nuclear Explosion Bubbles* [REDACTED] NOLTR-68-63, U.S. Naval Ordnance Laboratory, White Oak, Silver Spring, Maryland, 26 June 1968 [REDACTED]

[REDACTED]

Phillips, D. E., and R. L. Willey, *Underwater Explosion Tests of Two Steam Producing Explosives, II. 50- and 300-lb Charge Tests* [REDACTED] NOLTR-67-7, U.S. Naval Ordnance Laboratory, White Oak, Silver Spring, Maryland, 22 March 1967 [REDACTED]

Pinkston, J. M., Jr., *Surface Waves Resulting from Explosions in Deep Water* [REDACTED] Report 2, *Summary of Experimental Procedures and Results of Tests at Lake Ouachita, Arkansas* [REDACTED] DASA 1482-2, WES-TR-1-647, U.S. Army Engineer Waterways Experiment Station, Vicksburg, Mississippi, April 1966 [REDACTED]

Pittman, J. F., *Airblast from Shallow Underwater HBX-1 Explosions* [REDACTED] NOLTR-68-45, U.S. Naval Ordnance Laboratory, White Oak, Silver Spring, Maryland, 3 April 1968 [REDACTED]

Pyatt, D. E., *A Short Summary of Radiative Ground Coupling* [REDACTED] General Atomics, Inc., San Diego, California, April 1967 [REDACTED]

Rooke, A. D., Jr., G. B. Clark, and J. N. Strange, *Shot JOHNNY BOY, Mass Distribution Measurements*, POR-2282, U.S. Army Engineer Waterways Experiment Station, Vicksburg, Mississippi [REDACTED]

Rooke, A. D., Jr., and L. K. Davis, *FERRIS WHEEL Series, FLAT TOP Event, Crater Measurements*, POR-3008, U.S. Army Engineer Waterways Experiment Station, Vicksburg, Mississippi, 9 August 1966 [REDACTED]

Rudlin, L., and J. C. Silva, *Airblast from Underwater Nuclear Explosions* [REDACTED] NAVORD Report 6714, U.S. Naval Ordnance Laboratory, White Oak, Silver Spring, Maryland, 1 February 1960 [REDACTED]

Sauer, F. M., et al., *Nuclear Geoplosics, A Sourcebook of Underground Phenomena and Effects of Nuclear Explosions - Part Four, Empirical Analysis of Ground Motion and Cratering*, DASA 1285 (IV), 1964 [REDACTED]

Shelton, A. V., M. D. Nordyke, and R. H. Goerchermann, *The NEPTUNE Event, A Nuclear Explosive Cratering Experiment*, UCRL-5766, Lawrence Radiation Laboratory, Livermore, California, 19 April 1960 [REDACTED]

Shelton, F. H., B. S. Evans, and D. C. Sachs, *A Study of Air Blast Phenomenology in the Very High Pressure Region* [REDACTED] DASA-1331, Kaman Nuclear, Colorado Springs, Colorado, 31 December 1962 [REDACTED]

Snay, H. G., *The Hydrodynamic Background of the Radiological Effects of Underwater Nuclear Explosions* [REDACTED] NAVWEPS Report 7323, U.S. Naval Ordnance Laboratory, White Oak, Silver Spring, Maryland, 29 September 1960 [REDACTED]

Snay, H. G., *Underwater Explosion Phenomena: The Parameters of Migrating Bubbles*, NAVORD Report 4185, U.S. Naval Ordnance Laboratory, White Oak, Silver Spring, Maryland, 12 October 1962 [REDACTED]

[REDACTED]

Snay, H. G., *Hydrodynamic Concepts Selected Topics for Underwater Nuclear Explosions*, NOLTR-65-52, DASA-1240-1(2), U.S. Naval Ordnance Laboratory, White Oak, Silver Spring, Maryland, 15 September 1966 [REDACTED]

Snay, H. G., and J. F. Butler, *Shock Wave Parameters for Nuclear Explosions Under Water*, NAVORD Report 4500, U.S. Naval Ordnance Laboratory, White Oak, Silver Spring, Maryland, 1 May 1957 [REDACTED]

Snay, H. G., J. F. Butler, and A. N. Gleyzal, *Predictions of Underwater Explosion Phenomena*, WT-1004 (NOLR-1213), U.S. Naval Ordnance Laboratory, White Oak, Silver Spring, Maryland, May 1956 [REDACTED]

Strange, J. N., *Underwater Cratering*, Miscellaneous Paper No. 1-598, DASA-1240, Chapter VII, Part I, U.S. Army Engineer Waterways Experiment Station, Vicksburg, Mississippi, September 1963 [REDACTED]

Strange, J. N., *Water Shock-Wave Reflection Properties of Various Bottom Materials*, Miscellaneous Paper No. 1-826, U.S. Army Engineer Waterways Experiment Station, Vicksburg, Mississippi, June 1966 [REDACTED]

Strange, J. N., and S. H. Halper, *A Quantitative Evaluation of the Underwater Shock Wave Resulting from Surface and Underwater Explosions*, TR No. 2-615, U.S. Army Engineer Waterways Experiment Station, Vicksburg, Mississippi, February 1963 [REDACTED]

Strange, J. N., and L. Miller, *Blast Phenomena from Explosions at an Air-Water Interface*, Rept. 1, Miscellaneous Paper No. 1-814, U.S. Army Engineer Waterways Experiment Station, Vicksburg, Mississippi, June 1966 [REDACTED]

Taylor, G. I., "The Instability of Liquid Surfaces When Accelerated in a Direction Perpendicular to their Planes, Part I," *Proceedings of the Royal Society*, London, Volume A 201, pp. 192-196 [REDACTED]

U.S. Army Special Text 5-26, ADM Employment, U.S. Army Engineer School, Fort Belvoir, Virginia, November 1969 [REDACTED]

U.S. Standard Atmosphere, 1962, U.S. Committee on Extension to the Standard Atmosphere, available through the U.S. Government Printing Office, December 1962 [REDACTED]

U.S. Standard Atmosphere Supplements, 1966, U.S. Committee on Extension to the Standard Atmosphere, available through the U.S. Government Printing Office [REDACTED]

Van Dorn, W. G., B. LeMéhaute, and L. Hwang, *Handbook of Explosion-Generated Water Waves, Vol. I - State of the Art*, Report No. TC-130, Tetra Tech, Inc., Pasadena, California, October 1968 [REDACTED]

[REDACTED]

Van Dorn, W. G., and W. S. Montgomery, *Water Waves from 10,000-lb High-Explosive Charges*, Final Report Operation HYDRA II-A, S10 63-20, Scripps Institution of Oceanography, La Jolla, California, 1 June 1963 [REDACTED]

Veletsos, A. S., and N. M. Newmark, *Effect of Inelastic Behavior on the Response of Simple Systems to Earthquake Motions*, Ill. U. SRS 219; University of Illinois, Urbana, Illinois, 1960 [REDACTED]

Veletsos, A. S., and N. M. Newmark, *Response Spectra Approach to Behavior of Shock Isolation Systems*, Volume 2, Newmark, Hansen and Associates, Urbana, Illinois, June 1963 [REDACTED]

Vulnerability Handbook for Hardened Installations, Volume I Revised, Response to Large-Yield Nuclear Weapons [REDACTED] Newmark, Hansen and Associates, Urbana, Illinois, 1965 [REDACTED]

Walter, D., *Explosion-Generated Wave Tests, Mono Lake, California, Ground and Aerial Photography*, URS 654-2, URS Corporation, Burlingame, California, January 1966 [REDACTED]

Whalin, R. W., and R. Kent, *Water Waves Produced by Impulsive Energy Sources (U), Part VI: Data Analysis* [REDACTED] NMC-ONR-62, National Marine Consultants, Anaheim, California, December 1963 [REDACTED]

Whalin, R. W., and D. J. Divoky, *Water Waves Generated by Shallow Water Explosions*, Report No. S-359, National Engineering Science Co., Pasadena, California, September 1966 [REDACTED]

Wiegel, R. L., *Oceanographical Engineering*, Prentice Hall, 1964 [REDACTED]

Wilton, C., K. Kaplan, and N. R. Wallace, *Study of Channeling of Air Blast Waves*, URS 170-19, DASA 1605, URS Corporation, Burlingame, California, December 1964 [REDACTED]

Young, G. A., *The Physics of the Base Surge*, NOLTR-64-103, U.S. Naval Ordnance Laboratory, White Oak, Silver Spring, Maryland, 17 June 1965 [REDACTED]

Young, G. A., *Surface Phenomena of Underwater Nuclear Explosions* [REDACTED] NOLTR-63-111, DASA 1240-1(9), U.S. Naval Ordnance Laboratory, White Oak, Silver Spring, Maryland, 22 September 1965 [REDACTED]

Young, G. A., and B. W. Scott, *Explosion Debris Distributions Following Large Lithanol Underwater Explosions* [REDACTED] NOLTR-68-162, U.S. Naval Ordnance Laboratory, White Oak, Silver Spring, Maryland, 6 November 1968 [REDACTED]

